Understanding the Plasma Universe through Laboratory Experiments and Related Models

Thesis by
Yang Zhang

In Partial Fulfillment of the Requirements for the
Degree of
Doctor of Philosophy

CALIFORNIA INSTITUTE OF TECHNOLOGY
Pasadena, California

2024
Defended May 14, 2024

Yang Zhang
ORCID: 0000-0002-4168-9225

ACKNOWLEDGEMENTS

I would like to first thank my committee members, Professor Kerry J. Vahala, Professor Sterl Phinney, Professor Konstantin Batygin, and, of course, Professor Paul M. Bellan, for their invaluable presence and guidance throughout this endeavor.

My time pursuing my graduate studies at Caltech has been incredibly rewarding. I am sincerely thankful for the opportunity I have been given. These years have been the most enjoyable, productive, and intellectually stimulating period of my life, largely thanks to my advisor, Professor Paul M. Bellan. I cannot emphasize my gratitude enough towards him. Paul is an exceptional advisor from whom I have learned not only research but also humility and effective mentorship. His kindness, patience, and enthusiasm for plasma physics are unmatched. His insights across various aspects of the field are invaluable. He has always made himself available for students, whether in person or through phone and email. He is always willing to set aside whatever he is doing and patiently discuss any problem I bring up. Whenever I have a new idea, I eagerly anticipate hearing his thoughts on it. Paul consistently encourages me to do what I want to do and explore various research. He also enthusiastically promotes our work. Paul is incredibly generous in supporting me to attend conferences. I have been fortunate to present my research and learn from experts at numerous conferences. Paul is also a captivating storyteller. Having traveled to many corners of the world, he always has fascinating tales to share. I feel fortunate to have learned about his diverse experiences and perspectives. Paul, thank you for being such an inspiring advisor!

I would like to express my heartfelt gratitude to everyone in the Bellan plasma group. Their outstanding personalities and willingness to support each other have made my experience truly rewarding. I am incredibly fortunate to have collaborated with such an outstanding team. I extend my thanks to Pakorn Wongwaitayakornkul for his guidance in operating the solar loop experiment, to Young Dae Yoon for our insightful discussions on plasma physics, paper publication, and career prospects, to Ryan Marshall for our collaborative work on initial X-ray measurement, and Byonghoon Seo for answering my questions about plasma physics. I am also grateful to have had Yi Zhou join the group one year before me and André Nicolov one year after me. I want to thank them for attending most conferences together and engaging in enriching discussions on various aspects of our work. I really enjoyed working with Seth Pree together on the solar nanoflare experiment and the

double loop experiment. I am grateful for every piece of advice and assistance he provided me with. I am also thankful to have Joshua Morgan in the group. His enthusiasm for working on experiments and abundance of interesting ideas are truly inspiring. I eagerly anticipate seeing his 3D-printed vacuum chamber. Additionally, I have learned a lot of fascinating slang from him. I also thank Adele Payman for working in the same office and testing my idea on the double helix current wires equilibrium. I am grateful for the recent additions to our group, Efstratios Kritikos and Yegon Lim, whose diverse life experiences have enriched our discussions. I am also thankful to Dave Felt and Kevin Cooper for their technical support. I cannot express enough gratitude to Connie Rodriguez for her diligent management of the group's finances and for ensuring that no leftover food goes to waste. I thoroughly enjoyed our conversations and learning about her perspectives on American life, both past and present.

I would also like to express my gratitude for the generous funding provided by the Department of Energy, the Air Force Office of Scientific Research, and the National Science Foundation. Without the support of these funding sources, the research presented in this thesis would not have been possible.

I would like to extend my sincere thanks to Christy Jenstad and Jennifer Blankenship for their invaluable contributions to Applied Physics. Their dedication in organizing engaging activities and their unwavering support for students have made a significant difference in our academic journey.

Also, thank you to all of my friends inside and outside of Caltech. Especially those who play board games nearly every week and have dinner on every important holiday. Tian Xie, Yuchun Sun, Ruizhi Cao, Xiaoqiao Chen, Tianzhe Zheng, Zhiquan Yuan, Yongzhao Guo, Ding Zhong, Cheng Shen, Yifan Chen, Lue Wu, Xuejian Shen, Duxing Hao, Mingchen Liu. I am thankful to all the kind people who have touched my life.

Lastly, I want to express my deepest gratitude to my parents for their unconditional support. I would not have reached this milestone without your boundless love, encouragement, and belief in me. I am thankful to my girlfriend for being with me. I also want to thank my relatives, particularly my uncle and grandfather, for their steadfast love and support throughout this journey.

ABSTRACT

Laboratory experiments and the models they inspire are powerful tools for studying the plasma universe. This dissertation details possible solutions to two important problems in the plasma universe, namely how solar flares are generated and how accretion disks transport angular momentum and generate astrophysical jets.

Addressing the first problem, solar coronal loop physics is simulated in a laboratory experiment. The loop structure composed of braided strands is replicated. The MHD kink instability and the magnetic Rayleigh Taylor instability (MRTI) are observed to disrupt the loop structure. The dependence of the MRTI wavelength on the axial magnetic field is studied. Transient, localized 7.6-keV X-ray bursts and a several-kilovolt voltage spike are observed to be associated with the breaking of braided magnetic flux ropes containing 2 eV plasma. These spikes occur when the braid strand radius is choked down to be at the kinetic scale by either MHD kink or magnetic Rayleigh–Taylor instabilities. The observed sequence reveals an MHD to non-MHD cross-scale coupling that is likely responsible for generating solar energetic particles and X-ray bursts. All the essential components of this mechanism have been separately observed in the solar corona.

Magnetic flux ropes, the fundamental building block of magnetohydrodynamic plasma configurations, have often been observed to wrap around each other to form a helical braided structure with net axial current as observed from the laboratory experiment and solar coronal loops. Braiding phenomena extend to astrophysical jets, double helix nebula, and fusion plasma experiments. The equilibrium of braided flux ropes is more complicated than familiar axisymmetric systems because it requires balancing forces between the individual braids. A novel method for constructing these equilibria is developed. This method generates a double helix equilibrium with net axial current which is characteristic of observed solar loops and of laboratory-produced braided magnetic flux ropes. To the best of our knowledge, no previous model has been able to describe braided structures with net axial current. The net-axial-current equilibrium presented here reproduces the observed braided structure of the double helix nebula and is expected to be a powerful tool in other contexts.

Addressing the second problem, the dissertation introduces a first-principles angular momentum transport mechanism based only on collisions between neutrals and

charged particles in the presence of gravitational and magnetic fields. The mechanism is demonstrated by a 2D N-body simulation of a weakly-ionized system. It is found that ions and electrons drift in opposite radial directions as a result of colliding with Kepler-motion neutrals. This reduces the ordinary angular momentum of neutrals and increases the canonical angular momentum of charged particles in a manner such that the net global canonical angular momentum is conserved. The accumulation of ions at small radius and electrons at large radius produces a radially outward electric field, while current from the separation of ions and electrons is radially inward. Consequently, this process provides a gravitational dynamo converting gravitational energy into the electric energy that powers an astrophysical jet. Because this neutral angular momentum loss depends only on neutrals colliding with charged particles, it should be ubiquitous. The model predicts an accretion rate of 3×10^{-8} solar mass per year in good agreement with observed accretion rates.

Based on the conservation of canonical angular momentum and dynamics of charged particles under collisions with infalling neutrals, the dissertation also investigates the origin of angular momentum in astrophysical systems. A weakly-ionized, initially non-rotating cloud of neutral particles is shown to spontaneously start rotating when infalling. Quantitative scaling predicts an angular momentum generation rate sufficient to convert neutral infall motion into neutral Keplerian rotation in the outer region of a protoplanetary accretion disk.

PUBLISHED CONTENT AND CONTRIBUTIONS

1. Zhang, Y. & Bellan, P. M. Magnetic double helix. (under review) (2024).
   Y.Z. developed the model from suggestions and guidance of P.M.B.

2. Zhang, Y. & Bellan, P. M. Mechanism for generation of angular momentum in an astrophysical system. (to be submitted) (2024).
   Y.Z. performed the particle simulation from suggestions and guidance of P.M.B. The interpretation and analytical model was done jointly by Y.Z. and P.M.B.

3. Zhang, Y., Pree, S. & Bellan, P. M. Generation of laboratory nanoflares from multiple braided plasma loops. *Nature Astronomy* **7,** 655–661 (2023).
   Y.Z. designed the braided loop experiment from suggestions and guidance of P.M.B. S.P. built the X-ray camera from suggestions and guidance of P.M.B. Y.Z. and S.P. performed the experiment. The interpretation of the results was done jointly by all authors. Y.Z. drafted the manuscript. All authors revised the manuscript together.

4. Zhang, Y. & Bellan, P. M. Neutral-charged-particle collisions as the mechanism for accretion disk angular momentum transport. *The Astrophysical Journal* **930,** 167 (2022).
   Y.Z. performed the particle simulation from suggestions and guidance of P.M.B. The interpretation and analytical model was done jointly by Y.Z. and P.M.B.

5. Zhang, Y., Wongwaitayakornkul, P. & Bellan, P. M. Magnetic Rayleigh–Taylor instability in an experiment simulating a solar loop. *The Astrophysical Journal Letters* **889,** L32 (2020).
   Y.Z. designed the braided loop experiment from suggestions and guidance of P.M.B. S.P. built the X-ray camera from suggestions and guidance of P.M.B. Y.Z. and S.P. performed the experiment. The interpretation of the results was done jointly by all authors. Y.Z. drafted the manuscript. All authors revised the manuscript together.

TABLE OF CONTENTS

LIST OF ILLUSTRATIONS

Chapter 1

INTRODUCTION

1.1 Plasma Universe

Plasma is often referred to as the fourth state of matter, alongside solids, liquids, and gases. It is a state of matter in which atoms or molecules are ionized, meaning they have lost or gained electrons, resulting in a mixture of positively charged ions and free electrons. This ionized state gives plasma unique properties, such as the ability to conduct electricity, respond to electric and magnetic fields, and exhibit complex collective behavior. Figure 1.1 shows typical plasmas and their parameters of number density and temperature.

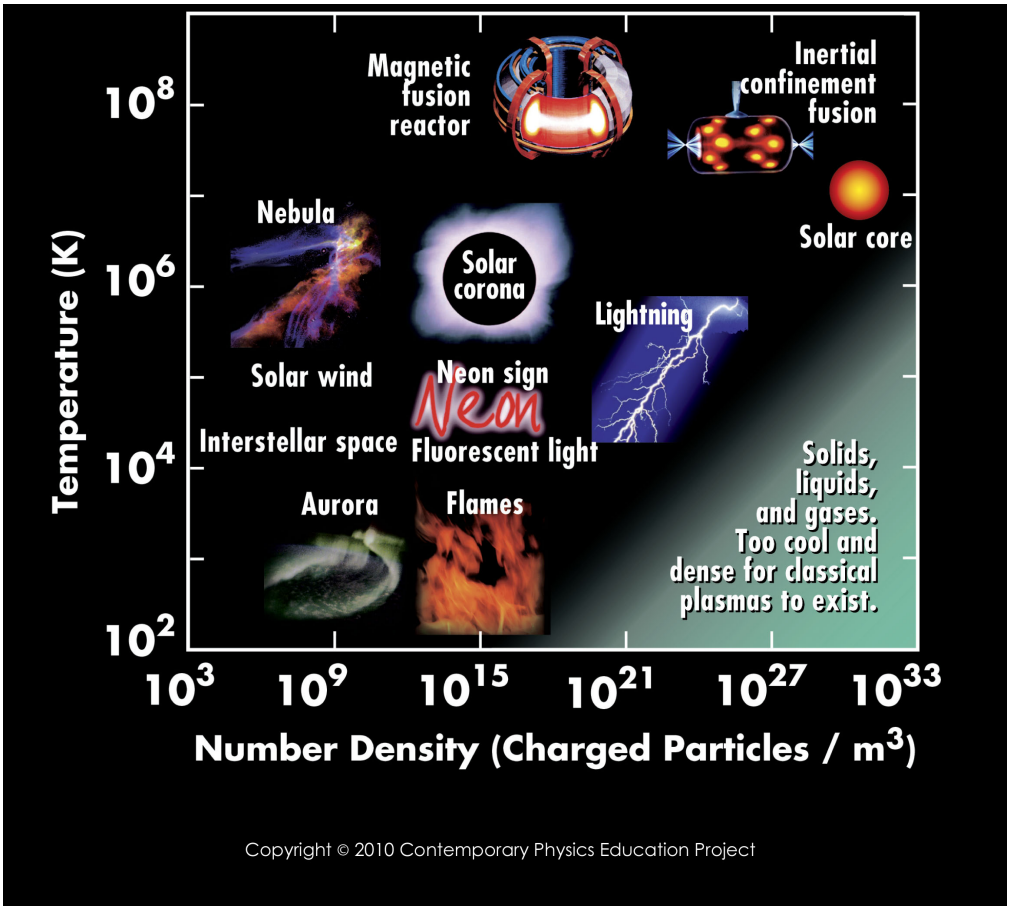

Figure 1.1: **Characteristics of typical plasmas.** This visual tool illustrates the relative positions of various scientific and natural plasmas based on their number density n and temperature T. Credit: Contemporary Physics Education Project.

Understanding and controlling plasmas is essential in various fields, including fusion energy research, space science, astrophysics, and materials science. Plasma physics is the branch of physics that studies the behavior, properties, and applications of plasmas.

1.2 Plasma Dynamics Models

In plasma dynamics, three main models are commonly used: Vlasov theory, two-fluid theory, and magnetohydrodynamics (MHD). Each model offers a different level of detail and complexity in describing plasma behavior. A comprehensive discussion of plasma physics can be found in the book, *Fundamentals of Plasma Physics* by Paul M. Bellan [1].

Kinetic Description

The Vlasov theory is a kinetic modeling approach. It is the most detailed and characterizes plasma dynamics. Rather than studying the evolution of every individual particle, the Vlasov model follows the temporal evolution of particle distribution functions $f(\mathbf{x}, \mathbf{v}, t)$. Given the acceleration of the particles $\mathbf{a}$, we can describe the evolution of $f(\mathbf{x}, \mathbf{v}, t)$ using the Vlasov equation

$$\frac{\partial f}{\partial t} + \mathbf{v} \cdot \frac{\partial f}{\partial \mathbf{x}} + \mathbf{a} \cdot \frac{\partial f}{\partial \mathbf{v}} = 0. \tag{1.1}$$

Typically, the acceleration is from the Lorentz force with $\mathbf{a} = \frac{q}{m}(\mathbf{E} + \mathbf{v} \times \mathbf{B})$.

Two-Fluid Description

By taking the integral of the distribution function and various degrees of the velocity, the averaged fluid description is derived. Fluid description considers the evolution of fluid quantities of every species σ, density $n_\sigma(\mathbf{x}, t) = \int f_\sigma(\mathbf{x}, \mathbf{v}, t)\, d\mathbf{v}$, mean velocity $\mathbf{u}_\sigma(\mathbf{x}, t) = \int \mathbf{v} f_\sigma(\mathbf{x}, \mathbf{v}, t)\, d\mathbf{v}$ on space. A set of partial differential equations governing these mean quantities is obtained by integrating various degrees of velocity with the Vlasov equation and a collision operator.

Continuity Equation

$$\frac{\partial n_\sigma}{\partial t} + \nabla \cdot (n_\sigma \mathbf{u}_\sigma) = 0 \tag{1.2}$$

Equation of Motion

$$n_\sigma m_\sigma \frac{d\mathbf{u}_\sigma}{dt} = n_\sigma q_\sigma (\mathbf{E} + \mathbf{u}_\sigma \times \mathbf{B}) - \nabla P_\sigma - \mathbf{R}_{\sigma\alpha} \tag{1.3}$$

where P_σ is the pressure, and $\mathbf{R}_{\sigma\alpha}$ is the collision force between fluid species σ and α.

The fluid model is obtained through the integration over velocity space, resulting in the loss of detailed information regarding the velocity distribution function.

MHD Description

Particle motion in the two-fluid system is described by the mean quantities of individual species. The MHD model couples together the mean quantities of different species and approximates the plasma as a single, finite-pressure, electrically conducting fluid. Defining $\rho = \sum_\sigma m_\sigma n_\sigma$, $\mathbf{U} = \frac{1}{\rho}\sum_\sigma m_\sigma n_\sigma \mathbf{u}_\sigma$, $\mathbf{J} = \sum_\sigma n_\sigma q_\sigma \mathbf{u}_\sigma$, and $P = \sum_\sigma P_\sigma$, the following are the derived MHD equations:

Continuity Equation

$$\frac{\partial \rho}{\partial t} + \nabla \cdot (\rho \mathbf{U}) = 0 \tag{1.4}$$

Equation of Motion

$$\rho \frac{d\mathbf{U}}{dt} = -\nabla P + \frac{1}{\mu_0}(\nabla \times \mathbf{B}) \times \mathbf{B} \tag{1.5}$$

Induction Equation

$$\frac{\partial \mathbf{B}}{\partial t} = \nabla \times (\mathbf{u} \times \mathbf{B}) \tag{1.6}$$

Equation of State

$$\frac{\partial P}{\partial t} + U \cdot \nabla P + \gamma P \nabla \cdot U = 0, \tag{1.7}$$

MHD works for large scale plasma phenomena. It is valid for phenomena with a length scale larger than the ion skin depth and the ion cyclotron radius and a time scale longer than the ion cyclotron periods.

An important dimensionless parameter is

$$\beta = \frac{P}{B^2/2\mu_0}, \tag{1.8}$$

which is the ratio between the plasma pressure and magnetic pressure. In general, when β is much less than 1 ($\beta \ll 1$), the magnetic field dominates over the plasma pressure, and the plasma is said to be magnetically dominated. Conversely, when β is much greater than 1 ($\beta \gg 1$), the plasma pressure dominates over the magnetic pressure, and the plasma is said to be pressure dominated.

There is no intrinsic physical scale inside of the MHD equations. The scaling allows for three free transformation parameters a_1, a_2, a_3 following invariant transformations: $L/a_1 \to L'$, $\rho_0/a_2 \to \rho'$, $B_0/\sqrt{a_3} \to B'$, $P_0/a_3 \to P'$, $\sqrt{a_2/a_3}v_0 \to v'$.

This scaling allows one-to-one correspondence between laboratory and astrophysical scales [2].

1.3 Solar Physics

Solar physics is the branch of astrophysics that focuses on the study of the Sun, our nearest star. It encompasses a wide range of phenomena occurring in and around the Sun, including its structure, dynamics, and influence on the solar system and beyond. Solar physics plays a crucial role in understanding fundamental processes such as solar particle acceleration, magnetic field dynamics, solar activity cycles, and space weather.

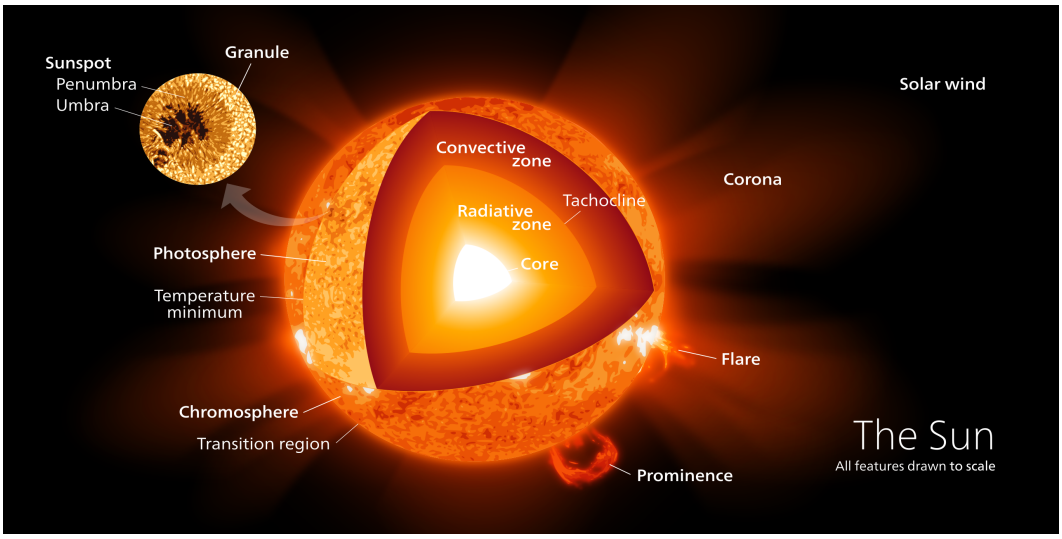

Figure 1.2: **Representation of the different layers and features of the Sun.** Credits: Kelvinsong.

The following is a brief introduction to solar structure and terminology.

Sun's structure

The Sun has a radius of 696 Mm and is composed of various layers and an extensive atmosphere. From the center outward, it consists of the core, radiative zone, convective zone, photosphere, chromosphere, and corona. Each of these layers has distinct characteristics and plays a crucial role in the Sun's structure and behavior.

Core: At the very center lies the core, where temperatures and pressures are incredibly high. The core of the Sun extends from the center to about 0.25 solar radii. Nuclear fusion occurs here, primarily converting hydrogen into helium through nuclear fusion. This process releases immense amounts of energy, which radiates

outward.

Radiative Zone: Surrounding the core is the radiative zone from the core out to about 0.7 solar radii. In this zone, energy generated in the core travels outward primarily through radiation. Photons generated in the core bounce around, gradually losing energy as they move toward the surface.

Convection Zone: The Sun's convection zone extends from 0.7 solar radii to near the surface. Here, energy is transported by the movement of hot plasma, similar to the way water boils and circulates in a pot on a stove. This convective motion brings heat to the surface.

Photosphere: The photosphere is the visible surface of the Sun, where most of the visible light that we see is emitted. It is a relatively thin layer, approximately 0.5 Mm thick, and is optically thick, meaning that light is absorbed and re-emitted multiple times before escaping into space. The temperature here is around 5,500 K. Sunspots are occasionally observed on the photosphere as visibly dark patches.

Chromosphere: Chromosphere is 2.5 Mm thick and optically thin layer above the photosphere. The temperature of the chromosphere increases gradually with altitude, ranging up to around 20,000 K near the top.

Corona: The outermost layer of the Sun's atmosphere is the corona. It extends millions of kilometers into space and is much hotter than the surface of the Sun, reaching temperatures of millions of Kelvin. The corona is visible during total solar eclipses as a faint, white halo around the Sun.

Solar coronal loop

Solar coronal loops are prominent structures in the Sun's corona, the outermost layer of its atmosphere, characterized by elongated loops or arcs of hot, glowing plasma. These loops are formed by the Sun's complex and dynamic magnetic field lines, which extend from the solar surface into the corona. The intense magnetic fields present in the Sun's atmosphere guide and confine the plasma along these magnetic field lines, giving rise to the loop-like shapes observed. Coronal loops are often visible in images of the sun taken in extreme ultraviolet or X-ray wavelengths. These structures can vary in size, from relatively small loops to giant arcs that span hundreds of thousands of kilometers. Coronal loops are important features for understanding the sun's magnetic activity and are closely studied by solar physicists to gain insights into processes such as solar flares, coronal mass ejections, and solar wind acceleration.

Solar flare

A solar flare is a relatively intense, localized emission of electromagnetic radiation in the Sun's atmosphere generated from magnetic field energy release. The electromagnetic radiation is of a broad spectrum from thermal emissions of extreme ultraviolet lights to non-thermal emissions of hard X-rays. Energetic particles are also observed during a solar flare.

1.4 Protoplanetary Accretion Disk

A protoplanetary disk is a structure formed around a young star during the process of planetary system formation. It consists of gas and dust particles orbiting the central star in a flattened, disk-like shape. These disks are often observed around young stars that are still in the process of accumulating material from their surrounding molecular clouds. Twenty nearby protoplanetary disk observations are shown in Figure 1.3. The formation of a protoplanetary disk begins with the collapse of a dense region within a molecular cloud, which eventually gives rise to a young star surrounded by a disk of leftover material. As the particles within the disk collide and stick together, they gradually grow in size through a process called accretion. Over time, these small particles coalesce to form larger objects, such as planetesimals, which serve as the building blocks for planets.

Protoplanetary disks are typically cold and weakly ionized. They have inner radii of a few a.u., outer radii of 100 a.u., and poloidal magnetic fields $\sim$ 1 milligauss [5]. Particles in the accretion disk undergo Keplerian motion and gradually accrete onto the central star. The accretion rates ranges from 10^{-9} to 10^{-7} $M_\odot$ yr^{-1} [6]. Bidirectional astrophysical jets are generated from protoplanetary disks as shown in Figure 1.4. The lifetime of a protoplanetary disk is around a few million years.

Understanding protoplanetary disks is essential for unraveling the mysteries of planet formation and the diversity of planetary systems observed in the universe.

Two important questions

Two important questions related to the protoplanetary disk have not been solved. The first problem is the angular momentum transport. Particles in the accretion disk are in Kepler motion. The angular momentum is $\sqrt{GM_* r}$. Accretion means the decrease of the radial distance r. To maintain the Kepler motion, particles need to reduce their angular momentum. Consequently, a mechanism is needed to remove the angular momentum to allow the particles to accrete.

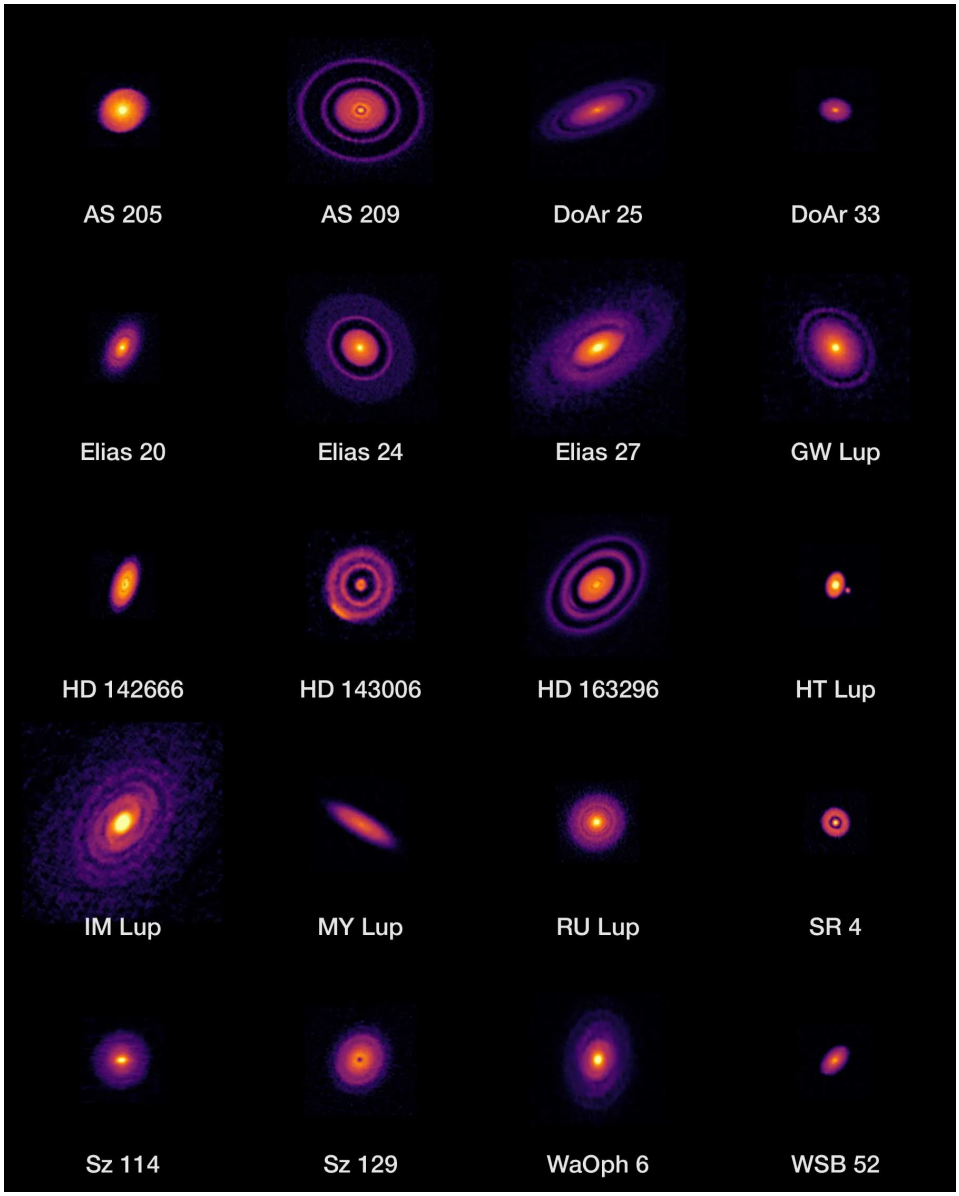

Figure 1.3: **Protoplanetary disks observations.** 20 nearby protoplanetary disks observed by Chile's Atacama Large Millimeter/submillimeter Array (ALMA) in 2018 for its Disk Substructures at High Angular Resolution Project (DSHARP). Credits: ALMA (ESO/NAOJ/NRAO) [3], S. Andrews *et al* [4]

.

The second problem is on the jet generation. Jets are driven by $\mathbf{J} \times \mathbf{B}$ magnetic force, where $\mathbf{J}$ is the electric current density and $\mathbf{B}$ is the magnetic field. To sustain the electric currents required to generate these jets, an energy source is needed to provide the necessary electrical energy. As the accretion disk is an isolated system, the electric energy must ultimately come from the gravitational energy released

during the accretion process. A mechanism is needed to convert gravitational energy into electrical energy.

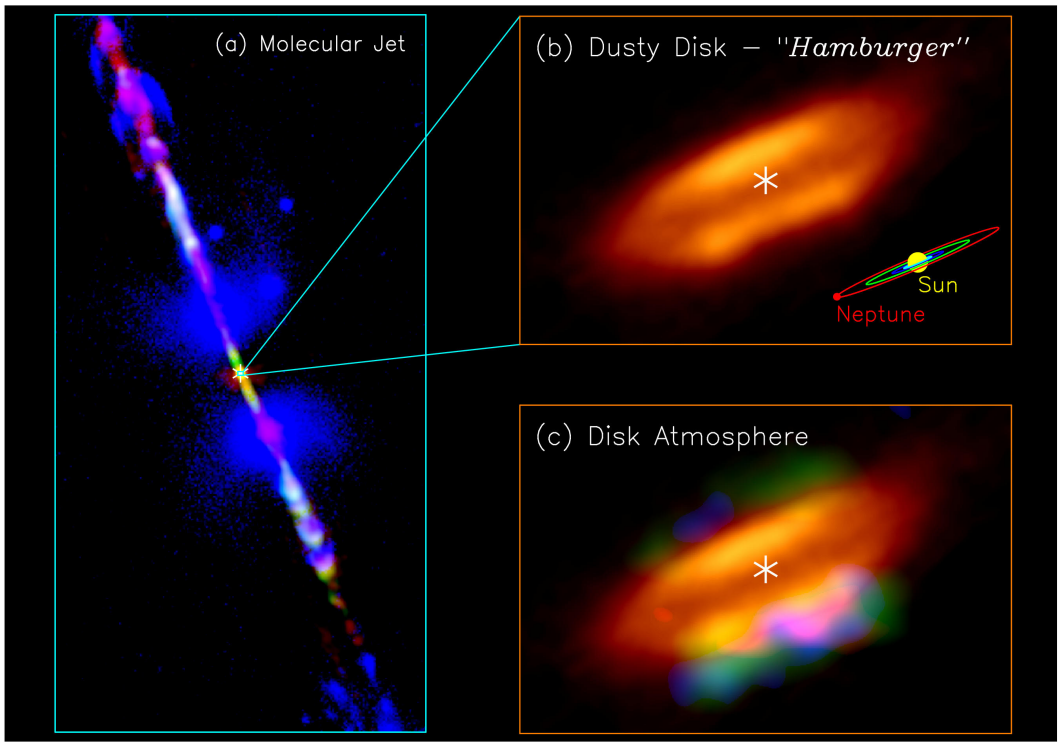

Figure 1.4: **Jet, disk, and disk atmosphere in the HH 212 protostellar system**. (a) A composite image for the HH 212 jet in different molecules, combining the images from the Very Large Telescope [7] and ALMA [8–10]. Orange image shows the dusty envelope+disk mapped with ALMA. (b) A zoom-in to the central dusty disk. The asterisk marks the position of the protostar. A size scale of our solar system is shown in the lower right corner for comparison. (c) Atmosphere of the accretion disk detected with ALMA. In the disk atmosphere, green is for deuterated methanol, blue for methanethiol, and red for formamide. Credit: ALMA (ESO/NAOJ/NRAO), Lee *et al* [8–10]

.

1.5 Laboratory Astrophysics

Laboratory astrophysics is a field that aims to simulate and study astrophysical phenomena and processes in controlled laboratory settings. By recreating extreme conditions found in space, researchers can gain insights into fundamental physical processes, test theoretical models, and interpret astronomical observations.

The constraints on observational access, as well as limitations in desired spatial and temporal resolutions, pose challenges in astrophysical research. Theoretical models

and simulations are bound by computational constraints, simplifying assumptions, and achievable parameters. Laboratory experiments offer a valuable avenue for exploring configurations similar to astrophysical systems on Earth. Notably, both laboratory experiments and astrophysical systems adhere to the same fundamental laws of physics and can be described by dimensionless equations. The scalability of laboratory experiments to real astrophysical systems is a key advantage, providing insights into phenomena that are challenging to observe directly. Conducting experiments under controlled conditions allows researchers to isolate specific variables, explore parameter space, and gain a deeper understanding of the underlying physics. Laboratory astrophysics advances our understanding of the universe by bridging the gap between theoretical models, observational data, and empirical knowledge of fundamental physical processes.

1.6 Thesis Overview

This dissertation explores experimental and theoretical investigations into two significant questions: the generation of solar flares (discussed in Chapters 3, 4, and 5) and the mechanisms by which accretion disks transport angular momentum and give rise to astrophysical jets (explored in Chapters 6 and 7). The research conducted in this dissertation encompasses a diverse array of approaches, including laboratory experiments, theoretical modeling, and numerical simulations, each addressing distinct aspects related to these overarching questions.

How solar flares are generated

Chapter 3 presents an experimental study of one MHD instability, magnetic Rayleigh Taylor instability. We observed MRTI developed on a laboratory plasma loop and showed that MRTI wavelength increases with the increase of background magnetic field strength. This provides a possible explanation of the different observed plume dynamics in the solar prominences and also points out a possible magnetic field measurement method from the MRTI wavelength.

Chapter 4 covers laboratory-created nanoflares. We replicated the braided feature of solar coronal loops. Transient, localized 7.6-keV X-ray bursts are observed in braided magnetic flux ropes of a 2-eV plasma when the braid strand radius is choked down to be at the kinetic scale by either MHD kink or magnetic Rayleigh–Taylor instabilities. This X-ray burst is of nanoflare feature with multiple separated observed X-ray bursts observed from multiple strands breaking at different times. This sequence of observations reveals a cross-scale coupling from MHD to non-MHD

physics that is likely responsible for generating solar energetic particles and X-ray bursts.

Chapter 5 presents a helical current wire model to construct the observed braiding behavior in nature and laboratory. A double helix equilibrium with the net axial current is derived, which is characteristic of observed solar loops and laboratory-produced braided magnetic flux ropes.

How accretion disks transport angular momentum and generate astrophysical jets

Chapters 6 and 7 shift focus to a new topic: the transport of angular momentum within accretion disks.

Chapter 6 covers a model of angular momentum transport and jet generation based only on the collisions between neutrals and charged particles and the basic conserved quantity canonical angular momentum. Collisions between neutrals and charged particles cause: (i) ions to move radially inwards, (ii) electrons to move radially outwards, (iii) neutrals to lose ordinary angular momentum, and (iv) charged particles to gain canonical angular momentum. Neutrals thus spiral inward due to their decrease of ordinary angular momentum. Quantitative scaling of the model using plausible disk density, temperature, and magnetic field strength gives an accretion rate in good agreement with observed accretion rates. This mechanism also naturally provides a gravitational dynamo process converting gravitational energy into electric field energy that powers astrophysical jets.

Chapter 7 builds upon the model developed in Chapter 6, extending it to a system characterized by radially free-falling particles. It provides a possible solution for spinning up an astrophysical system.

Chapter 2

CALTECH SOLAR LOOP EXPERIMENT

2.1 Experimental Setup

The experimental plasma is generated in a 1.5 m long, 1 m diameter stainless steel chamber having $\sim 10^{-7}$ torr base pressure. The chamber is considerably larger than the plasma and simulates a half-infinite space.

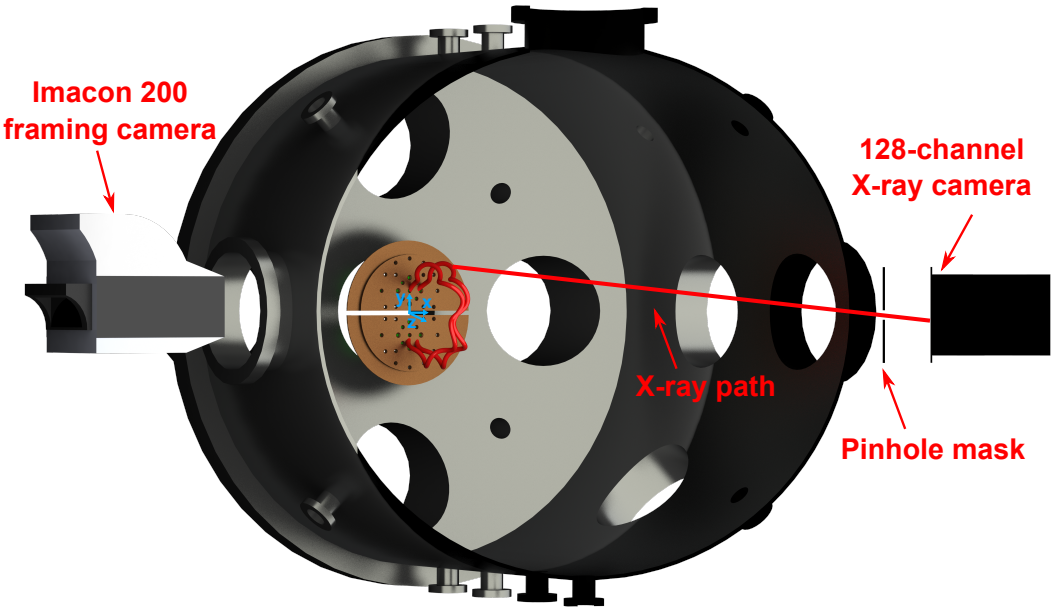

Figure 2.1: **Experimental set-up.** Plasma loop is created between two copper electrodes. The electrodes are mounted on the end dome of a 1.0-m-diameter, 1.5-m-long stainless steel vacuum chamber. Two solenoids are behind the electrodes to generate an arched magnetic field. The capacitor powering the solenoids is charged to a voltage V_b, so the bias magnetic field provided by the solenoids can be expressed as $B = \alpha V_b$, where α is a constant. Define a Cartesian coordinate system, as shown, with origin at the midpoint between electrodes, z along the vertical direction relative to electrode plane, and y along the line between the two electrode centers. Diagnostic devices include a visible-light fast framing camera, a gated linear spectroscopic array with a 1-ms time resolution, a 128-channel X-ray scintillators detector array, a high voltage probe Tektronix P6015 measuring the voltage across the two electrodes, a Rogowski coil measuring the current flowing through the plasma loop, and magnetic field probes measuring the magnetic field.

The plasma is generated using a plasma gun structure depicted in Figure 2.2. There are two copper plates. On each plate, there is a large number of gas nozzles to allow the gas to be puffed into the electrode region. We can control those nozzles to be open or closed so as to create different configurations of plasma loops. Behind the two electrodes, there are two solenoids for generating an arched magnetic field in front of the electrodes. A capacitor bank is connected to the electrodes to apply a high-voltage that ionizes neutral gas to form plasma.

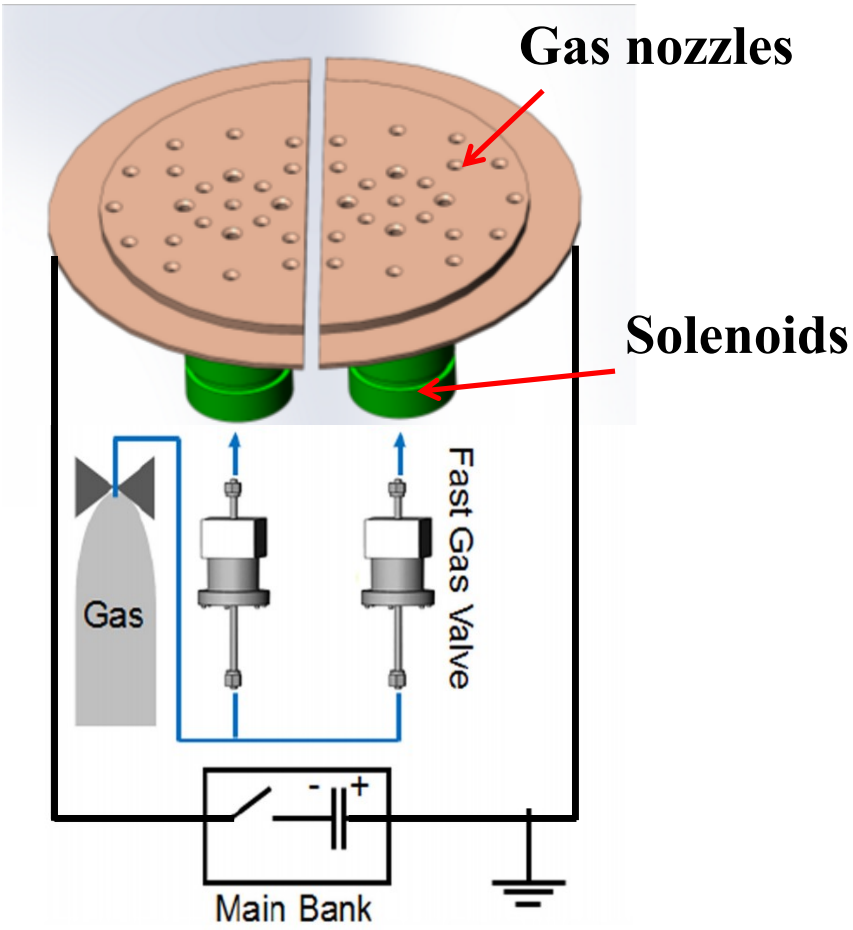

Figure 2.2: **Plasma gun structure**. Plasma loops are generated between the two copper plates. There are a large number of nozzles connected to a fast gas valve and a gas cylinder to allow the gas to be puffed into the electrode region. Positioned behind the electrodes are two solenoids, responsible for generating an arched magnetic field. A capacitor bank is linked to the two electrodes, supplying a discharge voltage to ionize the gas into plasma.

The firing sequence is shown in Figure 2.3. An arched 0.01 T – 0.3 T vacuum magnetic field called the bias field is produced by solenoids located behind the electrodes on a slow (ms) timescale so as to penetrate the electrodes. Gas is then

injected into the electrode region by fast gas valves. High voltage (3 – 6 kV) is applied across the electrodes on a fast (μs) timescale, breaking down the gas and creating plasma.

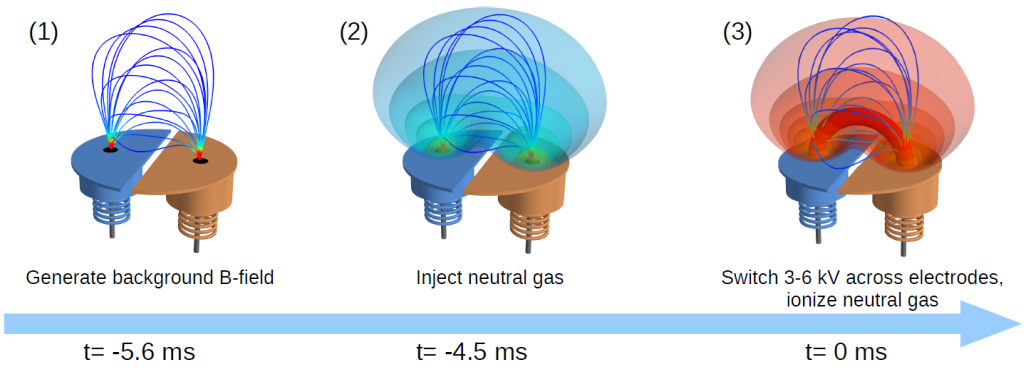

Figure 2.3: **Diagram of the single loop apparatus showing the primary steps to generate a flux rope**: (1) generate arched bias background magnetic field, (2) puff in neutral gas, and (3) switch capacitor bank across electrodes (adapted from [11] with permission).

The plasma is almost fully ionized, and has density $n \sim 10^{20} - 10^{21}\mathrm{m}^{-3}$ and temperature $\sim 2 - 10$ eV. The plasma duration is ~ 10 μs. The distance between the centers of the two electrodes is 8 cm. Figure 2.1 defines a Cartesian coordinate system with origin at the midpoint between electrodes, z along the vertical direction, and y along the line between the two electrode centers. The capacitor powering the solenoids is charged to a voltage V_b, so the bias magnetic field provided by the solenoids can be expressed as $B = \alpha V_b$, where α is a constant. Vacuum measurement of the bias field were made for $V_b = 50$ V at $x = 0$ cm, $z = 3.81$ cm for two different values of y. These give $\mathbf{B} = (0.00, 0.02, 0.08)$ T at $y = 5.08$ cm and $\mathbf{B} = (0.00, 0.04, 0.03)$ T at $y = 7.62$ cm.

2.2 Diagostics

Diagnostic devices include a visible-light fast framing camera, a 128-channel X-ray scintillators detector array, a gated linear spectroscopic array with a 1-ms time resolution, a high voltage probe Tektronix P6015 measuring the voltage across the two electrodes, a Rogowski coil measuring the current across the two electrodes, and magnetic probes.

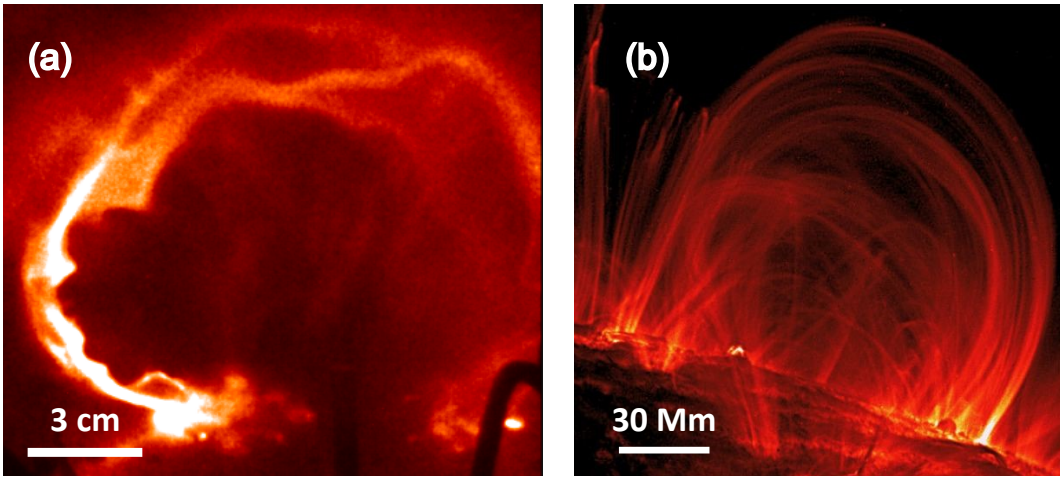

Figure 2.4: **Comparison between the Caltech experimental plasma loop and the solar coronal loop.** (a) Experimental plasma loop (b) Solar coronal loop (Credit: TRACE/NASA).

Visible light framing camera

The visible light emission of the plasma is captured using a DRS Hadland Imacon 200 high-speed camera. This camera comprises seven intensified charge-coupled device (ICCD) cameras, each capturing two frames from each shot. A beam splitter is employed to direct the incoming light into one of the seven ICCDs. The minimum interframe time is 5 ns. In our typical experimental setup, the plasma can be photographed using an exposure time of 20 ns and an inter-frame time of a few hundred nanoseconds. Each ICCD produces a 10-bit image with a resolution of 1200 × 980 pixels.

X-ray camera

The 128-channel X-ray detector shown in Figure 2.1 was comprised of a linear array of 128 LYSO(CE) scintillators (OST Photonics) which were fiber-coupled to a photomultiplier tube (PMT) array (4×Hamamatsu H7260-100). The PMT signals were digitized by a 128 channel, 125 MHz digitizer (CAEN R5560). The X-rays were viewed through a custom 254 μm thick polyimide window. Visible light was prevented from entering the detector by an 18 μm thick aluminum foil. Further details about this diagnostic and the X-ray transparent window are described elsewhere [12]. For pinhole imaging, the 0.7 mm by 51 mm rectangular pinhole was laser cut into a 0.76 mm thick stainless steel sheet and mounted 16 cm from the detector surface. The pinhole mask was 69 cm from the center of the electrodes.

Spectroscopy

We observe line emissions from the elements comprising the plasma. To analyze this light emission, we pass it through a spectrometer. The light with different wavelengths is diffracted to different angles and then captured by an intensified charge-coupled device (ICCD) camera. By comparing the spectrum of the emitted light with a thermodynamic model, we gain insight into the local state of the plasma. Doppler shift and Stark broadening can be used to infer the plasma flow velocity and density, respectively.

Voltage probe

A ×1000 high-voltage oscilloscope probe (Tektronix P6015A) is utilized to measure the voltage across the plasma, with the probe connected to the two electrodes. The output of this voltage probe is configured to drive a 1 MΩ oscilloscope input channel. To enable the output to drive a 50 Ω digitizer input channel, a buffer circuit is connected to the output of this probe.

Rogowski coil

A Rogowski coil [13] is employed to measure the current flowing through the plasma loop.

Magnetic probe array

The primary magnetic diagnostic is a 12-channel B-dot probe array. These 12 channels are arranged into four 3-axis clusters to measure the vector magnetic field at four locations located 17.5, 19.5, 21.5, and 25.5 cm from the electrode plane.

2.3 Scaling to Solar Corona

Figure 2.4 shows the Caltech experimental plasma loop and the solar coronal loop. They are of similar structure and dominated by MHD physics. The MHD behavior of the plasma loop can be scaled to the many other situations governed by MHD because MHD has no intrinsic length scale. As discussed in Chapter 1, MHD scaling [2] allows for three free parameters: a_1, a_2, a_3, following invariant relations: $\frac{L_0}{a_1} \rightarrow L'$, $\frac{\rho_0}{a_2} \rightarrow \rho'$, $\frac{B_0}{\sqrt{a_3}} \rightarrow B'$, $\frac{P_0}{a_3} \rightarrow P'$, $\frac{1}{a_1}\sqrt{\frac{a_3}{a_2}}t \rightarrow t'$, $\sqrt{\frac{a_2}{a_3}}v_0 \rightarrow v'$ to transform a scale to another scale having the same plasma beta. This transformation gives a one-to-one correspondence between systems, allowing laboratory experimental plasmas to be scaled to equivalent systems in space plasmas. One scaling to solar corona is shown in the Table of Figure 2.5. It shows characteristic parameters of the experiment,

the solar corona and the experiment scaled to the solar corona using $a_1 = 10^{-8}$, $a_2 = 1 \times 10^5$, $a_3 = 9 \times 10^2$. The scaled characteristic parameters have magnitudes similar to that of the solar corona.

	Experiment	Scaled Experiment	Solar Corona
Characteristic length L (m)	0.05	5×10^{6}	5×10^{6}
Characteristic time t (s)	10^{-6}	10	10
Magnetic field B (G)	3000	100	100
Mass density ρ ($\mathrm{kg \cdot m^{-3}}$)	1.7×10^{-6}	1.7×10^{-11}	1.7×10^{-11}
Pressure P (Pa)	800	0.89	0.32
Alfven velocity v_A($\mathrm{m \cdot s^{-1}}$)	2.1×10^{5}	2.2×10^{6}	2.2×10^{6}
Plasma beta β	0.02	0.02	0.01

Figure 2.5: **Plasma parameters of Caltech experiment and scaling to solar corona.** Typical values of the experiment (left column) are scaled according to the MHD scaling described in the text. The scaled values (center column) are in good agreement with approximate values for the solar corona (right column). This close correspondence indicates magnetohydrodynamic similarity between the two systems and the relevance of the experimental parameter regime to that of the solar corona. The experiment plasma is hydrogen plasma with a density 10^{21} $\mathrm{m^{-3}}$ and a temperature 5 eV. The solar corona has a density 10^{16} $\mathrm{m^{-3}}$ and a temperature 200 eV [14].

2.4 Previous Work

Many graduate students and postdocs have contributed to the solar loop experiments. Freddy Hansen explored the interaction between two plasma loops with the same helicity and reverse helicity [15] and the magnetic flux rope expansion mechanism. Shreekrishna Tripathi investigates the kinetic jets from the plasma loop [16]. Eve Stenson explored magnetically driven flows [17]. Bao Ha studied the mechanisms for flux rope expansion [18]. Magnus Haw examined MHD collimation mechanism in arched flux ropes [19] and the formation of coronal mass ejection cavity [20]. Pakorn Wongwaitayakornkul investigated apex dips [21] and magnetically induced current piston [22].

Chapter 3

MAGNETIC RAYLEIGH TAYLOR INSTABILITY

1. Zhang, Y., Wongwaitayakornkul, P. & Bellan, P. M. Magnetic Rayleigh–Taylor instability in an experiment simulating a solar loop. *The Astrophysical Journal Letters* **889,** L32 (2020).

My initial investigation into the solar loop experiment begins with examining the phenomenon of magnetic Rayleigh Taylor instability (MRTI). Prior to this work, MRTI had already been observed in a separate laboratory experiment, namely the Caltech astrophysical jets experiment. In that context, a kink instability constricts the jet channel, contributing to a secondary acceleration that propels MRTI forward [23]. In the solar loop experiment, the loop structure is inherently curved, allowing for expansion and thus creating an effective gravitational force that facilitates MRTI. We observed MRTI developed on the laboratory plasma loop and showed that MRTI wavelength increases with the increase of the background magnetic field strength. This provides a possible explanation of the different observed plume dynamics in the solar prominences and also points out a possible magnetic field measurement method from the MRTI wavelength.

3.1 Introduction

The Rayleigh-Taylor Instability (RTI) is an important instability in many astrophysical and laboratory systems, such as supernova explosions [24–26], solar prominences [27–30], and inertial confinement fusion [31, 32]. RTI occurs when a heavy fluid is initially on top of a light fluid . If the low-density fluid is vacuum, the interface is planar, and there is no magnetic field, the growth rate of this one-dimensional instability is

$$\gamma = \sqrt{gk} \tag{3.1}$$

where g is the gravitational acceleration and k is the spatial wavenumber. The instability grows as $\exp(\gamma t)$ with a ripple structure initially followed by later development of plumes and finger-like structures. For a plasma supported above vacuum by a magnetic field parallel to the planar interface, assuming that there is no magnetic field shear near the interface and the conducting wall is far away from the MRTI

location [33–35], the growth rate reduces to

$$\gamma^2 = gk - \frac{2\left(\mathbf{k}\cdot\mathbf{B_0}\right)^2}{\mu_0\rho} \tag{3.2}$$

where $\mathbf{B_0}$ is the unperturbed magnetic field. For a perturbation with $\mathbf{k}\perp\mathbf{B_0}$, also known as an interchange mode, the growth rate is the same as the RTI without a magnetic field. However, for a perturbation with $\mathbf{k} \parallel \mathbf{B_0}$, known as an undular mode, the growth rate is

$$\gamma^2 = gk - \frac{2\left(kB_0\right)^2}{\mu_0\rho}\ . \tag{3.3}$$

The undular mode has a critical wavelength

$$\lambda_\mathrm{c} = \frac{4\pi B_0^2}{\mu_0\rho g} \tag{3.4}$$

at which $\gamma = 0$. If $\lambda < \lambda_\mathrm{c}$, $\gamma^2 < 0$, which implies that only perturbations with wavelength $\lambda > \lambda_\mathrm{c}$ can grow. Equation 3.3 also shows that there is a fastest growing wavelength which is given by

$$\lambda_\mathrm{m} = 2\lambda_\mathrm{c} = \frac{8\pi B_0^2}{\mu_0\rho g} \tag{3.5}$$

and which corresponds to a maximum growth rate

$$\gamma_\mathrm{m} = \sqrt{\frac{gk}{2}}\ . \tag{3.6}$$

Zhai & Bellan [36] derived the MHD theory of the magnetic Rayleigh Taylor instability on the surface of a magnetically confined cylindrical plasma flux rope. The Rayleigh-Taylor instability is found to couple to the classic current-driven instability, resulting in a new type of hybrid instability.

The MRTI is thought to be the mechanism for the formation and dynamics of plumes in solar prominences. Berger *et al.* [27] observed the upflows from plumes caused by the MRTI. Ryutova *et al.* [28] described how the theoretically predicted growth rates and behaviors for the MRTI matched observations of quiescent prominence plumes. Hillier *et al.* [37] verified the MRTI mechanism for upflows from simulations. Keppens *et al.* [38] found the indications of secondary Kelvin-Helmholtz (KH) instabilities due to shear flows at the bubbles. However, the dependence on magnetic field strengths and how this dependence affects observed differences is still not

determined. An example of such differences is that some prominences produce many small plumes while others produce only large plumes [27].

Previous experiments [39–41] investigated the MRTI using Z-pinch implosions, but these experiments focused mainly on the growth rate and X-ray production and did not vary the magnetic field to test for a relation between magnetic field and the MRTI wavelength.

In the Caltech solar loop experiment, a magnetized plasma loop is generated to simulate solar flux ropes. We show here the existence of a hoop force driven magnetic Rayleigh-Taylor instability in this experiment. Detailed measurements indicate a scaling where the observed axial wavelength λ increases with axial magnetic field, and this scaling is shown to be consistent with the MRTI.

3.2 Experimental Results

The image in Figure 3.1 shows a typical observed MRTI. The MRTI occurs in a positive y region (upper region) with $y = 5 - 8$ cm, $z = 1 - 4$ cm as determined from the images. The growth rate γ_{observed} is determined by measuring the MRTI amplitude at a sequence of times. The effective gravitational acceleration $g_{\text{effective}}$ is determined from the y direction motion of the loop at the location where the MRTI takes place. The wavelength λ is obtained from the image when the MRTI first appears and ranges from 0.5 cm to 2.5 cm. We assume the observed MRTI is the fastest growing mode and compare the calculated growth rate $\gamma_{\text{calculated}} = \gamma_{\text{max}} = \sqrt{\pi g_{\text{observed}}/\lambda}$ to the observed growth rate. The table in Figure 3.1 presents this comparison and shows that the observed growth rate is in good agreement with the calculated growth rate; this confirms that the observed structure is the MRTI.

Another question concerns the mechanism providing the effective gravity. We now show that this mechanism is provided by the hoop force acceleration. A circular, current-carrying hoop [42] with major radius R, minor radius a, internal inductance per unit length l_{i}, and current I experiences an outward radial force per unit length

$$f_{\text{hoop}} = \frac{\mu_0 I^2}{4\pi R}\left[\ln\left(\frac{R}{a}\right) + 1.08 + \frac{l_{\text{i}}}{2}\right] . \tag{3.7}$$

Assuming the current is uniformly distributed, $l_{\text{i}} = 0.5$, so

$$f_{\text{hoop}} = \frac{\mu_0 I^2}{4\pi R}\left[\ln\left(\frac{R}{a}\right) + 1.33\right] \tag{3.8}$$

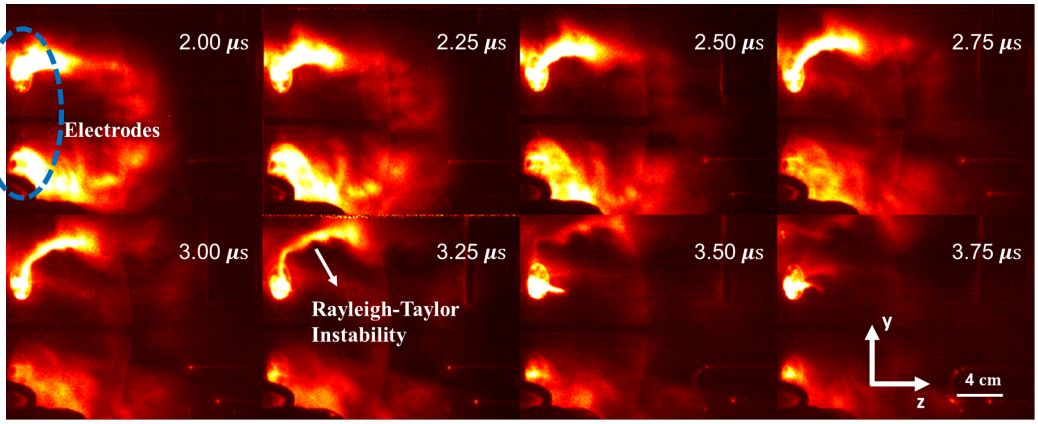

Shot #	V_b (V)	I (kA)	a (cm)	R (cm)	λ (cm)	g_{observed} $(10^{10}\text{m}\cdot\text{s}^{-2})$	$g_{\text{calculated}}$ $(10^{10}\text{m}\cdot\text{s}^{-2})$	γ_{observed} $(10^{6}\cdot\text{s}^{-1})$	$\gamma_{\text{calculated}}$ $(10^{6}\cdot\text{s}^{-1})$
7385	30	8.5	0.75	5.3	0.8	4.4	5.5	4.2	4.1
7313	40	8.7	0.78	5.1	1.2	2.9	5.4	3.1	2.8
7359	50	8.7	0.81	5.0	1.7	3.5	5.0	2.5	2.6
7274	60	9.2	0.82	5.1	2.3	3.4	5.3	1.8	2.2

Figure 3.1: **MRTI observation.** The image shows the MRTI in a time series images of N_2 plasma loop evolution. The table shows comparison between the observed growth rate and the calculated growth rate from the MRTI theory and comparison between the observed acceleration and the calculated acceleration from hoop force theory.

which gives an acceleration

$$g_{\text{hoop}} = \frac{f_{\text{hoop}}}{\rho\pi a^2} = \frac{\mu_0 I^2}{4\pi^2\rho a^2 R}\left[\ln\left(\frac{R}{a}\right) + 1.33\right] . \tag{3.9}$$

R and a are obtained from the images and I is obtained from a Rogowski coil measurement. This provides sufficient information to compare the observed acceleration g_{observed} with the calculated acceleration $g_{\text{calculated}}$ from the hoop force. The MRTI occurs at $t = 2 - 3$ μs and parameters measured at $t = 2$ μs are used with density assumed to be $n = 2 \times 10^{21}$ m^{-3} [11, 18]. The gas used is N_2. The table in Figure 3.1 shows that the observed acceleration and the calculated acceleration have order of magnitude agreement. Discrepancies exist presumably because the current loop in the experiment is not a complete circle. Also, the measured current does

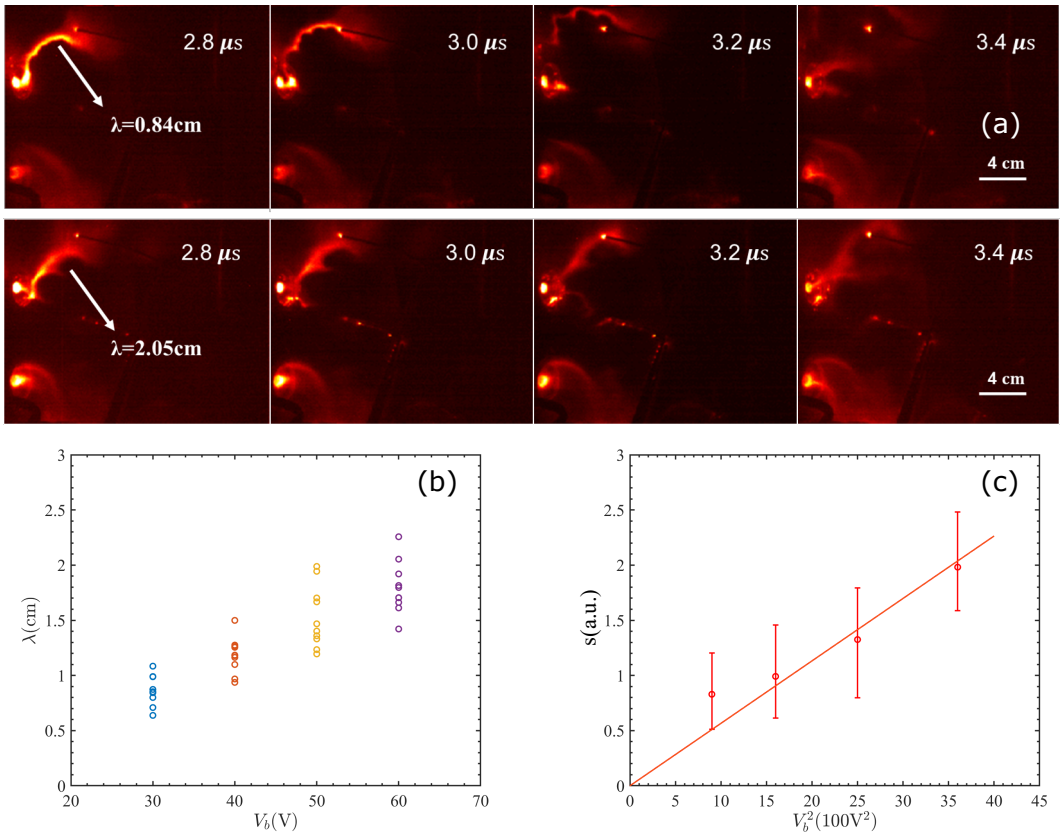

Figure 3.2: **MRTI dependence on axial magnetic field.** (a) Time series images of N_2 plasma loop evolution (upper shot# 7385 and V_b = 30 V, lower shot# 7281 and V_b = 60 V). (b) Plot of the wavelength of the MRTI versus different bias voltage. (c) Plot of s versus V_b^2 (each data point is from 10 shots and the error bar represents the spread over these shots).

not fully flow through the visible loop [18, 43]; this is consistent with the observed acceleration being smaller than the calculated one.

The bias voltage V_b (applied on the solenoids) controls the background axial magnetic field of the loop. When we increase the bias voltage so as to increase the axial magnetic field, we find the wavelength of the MRTI increases, as shown in Figure 3.2a. For a sufficiently large bias magnetic field, the MRTI is not observed.

Figure 3.2b shows measurements for a sequence of bias fields V_b = 30, 40, 50, 60 V, each repeated for 10 shots. This plot indicates that for increasing bias voltage (which is proportional to the axial magnetic field), the wavelength increases.

This phenomenon is consistent with the MRTI theory, since Equation 3.5 shows that the increase of magnetic field causes the corresponding fastest growth wavelength to increase. For a sufficiently large magnetic field, the wavelength is larger than the

loop dimensions and the MRTI cannot occur. This is most likely the reason for the absence of the MRTI in previous solar loop simulation experiments where a much larger axial magnetic field was used (e.g., [17, 21]). In Equation 3.5, besides B_0, the other two parameters ρ, g also influence the fastest growth wavelength. In order to remove the influence of these parameters and verify that the increasing wavelength corresponds with the MRTI theory, we introduce the parameter $s = \lambda\rho g$. Using Equation 3.5, the fastest growing mode corresponds to

$$s = \frac{8\pi}{\mu_0} B_0^2 = \frac{8\pi\alpha^2}{\mu_0} V_b^2 \,. \tag{3.10}$$

To determine s, the quantities λ and g are obtained from the image measurement, while n is determined as a relative density from the light intensity which scales as n^2. Keeping other experimental parameters the same, we set V_b = 30, 40, 50, 60 V for 10 shots at each voltage to obtain s. Figure 3.2c shows s plotted versus V_b^2. The error bars are determined by the shot-to-shot variation of measured data and the line shows the best fit. From this figure, it is clear that s scales as V_b^2 as predicted by Equation 3.10.

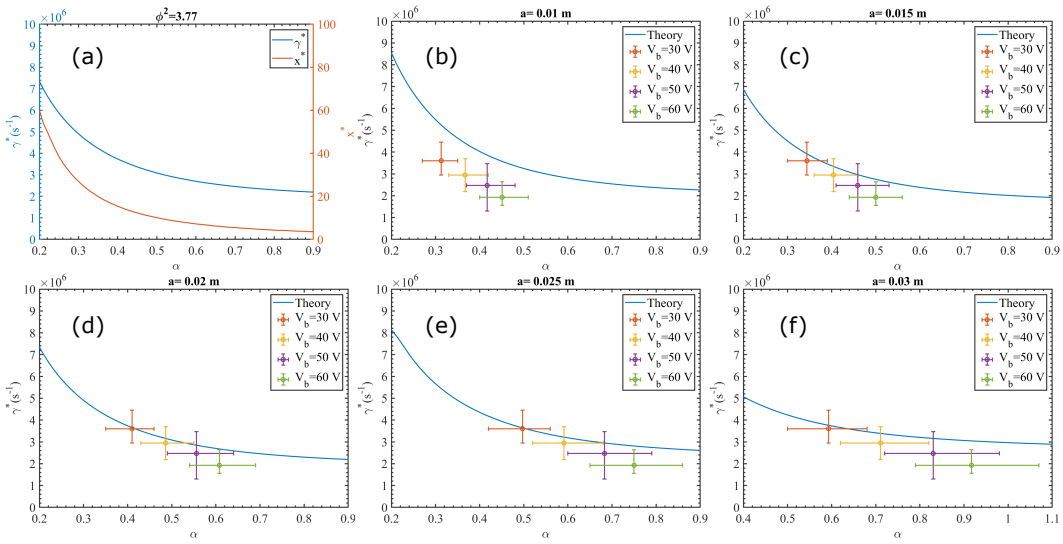

Figure 3.3: **Comparison with the MRTI theory under cylinder geometry.** (a) x^* and γ^* versus α with Φ^2 = 3.77. (b - f) Comparison between the observed growth rate and the calculated growth rate from the MRTI theory under cylindrical geometry (each data point is from 10 shots and the error bar represents the spread over these shots).

As the geometry of the experiment is more like a cylinder. The experiment results can also been used to compare with the magnetic Rayleigh Taylor instability under

cylindrical geometry derived by Zhai & Bellan [36]. Using the notation in Zhai & Bellan [36], the growth rate is

$$\gamma = \gamma\left(x, \alpha, \Phi^2\right) \tag{3.11}$$

where $x = ka = 2\pi a/\lambda$, $\alpha = B_z/B_\theta$, $\Phi^2 = \mu_0 \rho g a \big/ B_\theta^2$ and a is the radius of the cylinder. Consider a system with certain values Φ^2 and α subject to a random perturbation that contains all possible $x = ka$. The component x that gives the largest $\gamma = \gamma\left(x, \alpha, \Phi^2\right)$ is defined as x^*, and the fastest growth rate is defined as γ^*. $x^*\left(\alpha, \Phi^2\right) = x$ that maximizes $\gamma = \gamma\left(x, \alpha, \Phi^2\right)$. Figure 3.3 (a) shows the dependence of the fastest growing mode on α for fixed $\Phi^2 = 3.77$. Note that α is proportional to the axial magnetic field and x corresponds to $1/\lambda$. Figure 3.3 (a) shows that with the increase of axial magnetic field, the wavelength increases and the growth rate decreases, the same trend as predicted for the MRTI in planar geometry.

We assumed all of the experiments have the same parameters except for axial field with $\rho = 5 \times 10^{-5}$ m^{-3}, $g = 3 \times 10^{10}$ m $\cdot$ s^{-2}, $I = 10^4$ A, $B_\theta = \mu_0 I/2\pi a$, and that the observed mode is the fastest growing mode. The only free parameter in the determination of Φ^2 is a. From the experimental results, x^* can be obtained and the corresponding α and γ^* can be calculated. The observed growth rate and the calculated growth rate are compared in Figure 3.3 (b - f) for different a. For $a = 0.015 - 0.025$ m, the observed growth rate agrees well with the MRTI theory in cylindrical geometry. The value for the radius is somewhat larger than the observed 0.008 m value. This discrepancy may result from simplifying theoretical assumptions such as uniform density and axial magnetic field and current flowing through the surface. In [36], the radius used for comparison was also larger than the observed one from the image.

3.3 Conclusions and Discussions

In conclusion, we have determined a hoop force driven MRTI in a laboratory experiment. Changing the axial magnetic field shows that the wavelength of the MRTI increases with increase of axial magnetic field. This scaling is verified to be consistent with both the planar MRTI theory and the more detailed cylindrical MRTI theory.

For the experiment, the characteristic length is $L = 0.01$ m and the characteristic time is $\tau = 10^{-6}$ s. Plasma density is about 2×10^{21} m^{-3}. Plasma temperature is assumed to be 5 eV. The corresponding Debye length $\lambda_D = \sqrt{\frac{\varepsilon_0 k_B T}{ne^2}} = 3.7 \times 10^{-7}$ m $\ll$ L

and $4\pi n\lambda_D^2/3 = 430 \gg 1$. The resistive diffusion time is $\mu_0 L^2/\eta = 2\times10^{-6}$ s $>\tau$, where the Spitizer resistivity $\eta = 6.8\times10^{-5}\ \Omega\cdot$ m. There may be some magnetic field diffusion effects. Near the MRTI region, the axial magnetic field is measured to be 0.04 T - 0.1 T when there is no plasma. The toroidal magnetic field generated by the current is calculated to be 0.2 T - 0.4 T, so we assume a nominal total magnetic field $\sim$ 0.3 T. For B = 0.3 T, the cyclotron frequency for nitrogen is then $\omega_{ci} = 2\times10^6$ s^{-1} while the characteristic time is $\tau = 10^{-6}$ s. The system is thus marginally in the MHD regime. Hall term corrections may thus alter the MRTI dispersion relation derived from ideal MHD. We do not insert magnetic probes to measure the magnetic field at the MRTI location because the MRTI scale is so small that a probe will disturb the MRTI. As the MRTI dispersion relation derived from ideal MHD can describe this phenomenon properly, we assume the ideal MHD provides a reasonable description to lowest order.

The MRTI behavior reported here is likely to apply to many other situations governed by MHD because MHD has no intrinsic length scale. MHD scaling [2] allows for three free parameters: a_1, a_2, a_3, following invariant relations: $\frac{L_0}{a_1} \rightarrow L'$, $\frac{\rho_0}{a_2} \rightarrow \rho'$, $\frac{B_0}{\sqrt{a_3}} \rightarrow B'$, $\frac{P_0}{a_3} \rightarrow P'$, $\frac{1}{a_1}\sqrt{\frac{a_3}{a_2}}t \rightarrow t'$, $\sqrt{\frac{a_2}{a_3}}v_0 \rightarrow v'$, $\frac{a_1 a_2}{a_3}g_0 \rightarrow g'$ to transform a scale to another scale having the same plasma beta. This transformation gives a one-to-one correspondence between systems, allowing laboratory experimental plasmas to be scaled to equivalent systems in space plasmas.

Figure 3.4 shows the MRTI in a quiescent prominence observed on 2007 August 8th UT in the Hα line from HINODE Solar Optical Telescope [44]. The mean value of initial wavelength is about 1 Mm and the characteristic time of the MRTI is about 1 min [27]. For a typical solar prominence, a representative value for mass density is 5×10^{-10} kg$\cdot$m^{-3} [45]. The pressure is in the range $0.01-0.1$ Pa and a representative value is 0.05 Pa [46]. The magnetic field is about $3-26$ G and a representative value is 12 G [47].

The table in Figure 3.4 shows characteristic parameters of the experiment, the solar quiescent prominence and the experiment scaled to the solar prominence using $a_1 = 10^{-8}$, $a_2 = 1\times10^5$, $a_3 = 6\times10^4$. The scaled characteristic parameters have magnitudes similar to that of a solar quiescent prominence. From these results, the variation of magnetic field strength may be a reason for observed differences in plume dynamics in solar prominences, so that prominences having weak magnetic field produce many small plumes while those with strong magnetic fields produce large plumes.

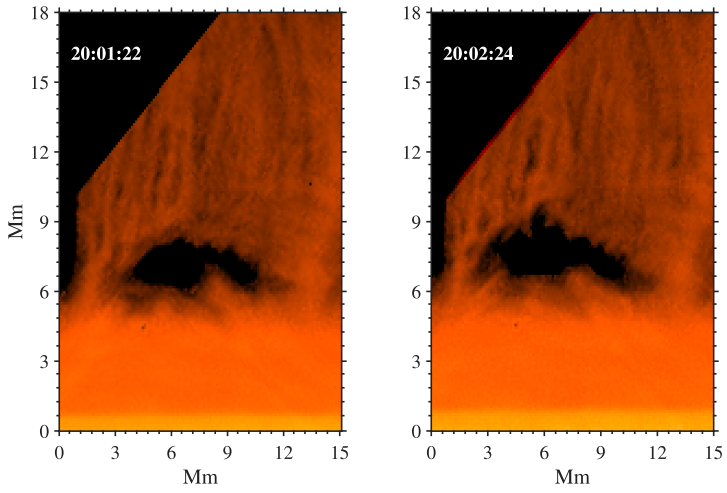

	Experiment	Solar quiescent prominence	Scaled experiment
$L\,(\mathrm{m})$	10^{-2}	10^{6}	10^{6}
$t\,(\mathrm{s})$	10^{-6}	60	78
$B\,(\mathrm{T})$	0.3	1.2×10^{-3}	1.2×10^{-3}
$\rho\,(\mathrm{kg \cdot m^{-3}})$	5×10^{-5}	5×10^{-10}	5×10^{-10}
$P\,(\mathrm{Pa})$	3×10^{3}	5×10^{-2}	5×10^{-2}
$v_A\,(\mathrm{m \cdot s^{-1}})$	3.8×10^{4}	4.8×10^{4}	4.9×10^{4}
β	0.08	0.09	0.08
$g\,(\mathrm{m \cdot s^{-2}})$	3×10^{10}	274	500

Figure 3.4: **Comparison with solar observation.** The image shows the MRTI in a quiescent prominence observed on 2007 August 8$^{\text{th}}$ 20:01:22 and 20:02:24 UT in the Hα line from HINODE Solar Optical Telescope [44]. The table shows dimensionless scaling of the experiment to solar prominences.

Chapter 4

LABORATORY NANOFLARES

1. Zhang, Y., Pree, S. & Bellan, P. M. Generation of laboratory nanoflares from multiple braided plasma loops. *Nature Astronomy* **7,** 655–661 (2023).

In Chapter 3, alongside MRTI, we also observed MHD kink instability within the single loop structure. When these MHD instabilities choke the loop structure to the kinetic scale of ion skin depth, we detected hard X-rays associated with this process, utilizing a single-channel X-ray detector devised by Ryan Marshall [48]. We attempted to link this process with the generation of X-rays from solar coronal loops. Solar coronal loops typically have a radius on the order of 10^6 meters, whereas the ion skin depth for typical solar corona densities is around 10 meters. Consequently, it would pose a challenge for MHD instabilities to choke a 1 Mm solar coronal flux rope down to the ion skin depth.

Addressing this challenge prompted us to consider a probable mechanism through which the solar scenario could still engender kinetic instability. The crucial insight lies in recognizing that the solar coronal flux rope is not a singular entity but rather comprises numerous fine strands braiding around each other, each only a few ion skin depths thick. Consequently, MHD instabilities need only constrict individual strands by a modest factor to reach the ion skin depth scale.

To validate this braided loop structure concept, we redesigned the electrode structure with more gas nozzles to generate braided magnetic flux ropes. In this novel experimental setup, we replicated the braided configuration characteristic of solar coronal loops. MHD instabilities developed on each strand independently and choked each strand down at different times. The bursting of individual strands gives rise to X-ray emissions. Our thorough measurements of these intricately braided strands and the resulting X-rays reveal a multi-scale process that could possibly be responsible for the generation of energetic particles and X-rays during solar flares.

4.1 Introduction

Energetic particles and X-ray bursts are generated by solar flares. This generation cannot be explained by MHD physics and, instead, is presumed to depend on non-

MHD physics having a characteristic length scale that is smaller than can be modeled by MHD. Because MHD is valid only for scale lengths greatly exceeding the ion skin depth which in the solar corona is about 1 to 10 m, it is likely that the scale length of the non-MHD physics that occurs when MHD breaks down is of this order. Existing solar observation technology provides significant information about energetic particles and the X-ray burst generation processes [49–53]. However, because the best resolution of solar observations is about $10^5 - 10^6$ m [54, 55] and so is much coarser than the ion skin depth, many fine details cannot yet be resolved.

Thus, understanding how energetic particles and X-rays are produced is a critical problem. Parker [56, 57] proposed that energetic particles and X ray bursts are created by the dissipation of tiny tangential magnetic discontinuities formed from convection-caused continuous and random motion of magnetic field photospheric footpoints. He labeled the basic unit of impulsive energy release a "nanoflare" and proposed that large, X-ray producing solar flares are swarms of nanoflares each of which is too small to be resolved by existing observational methods. On the other hand, Alfvén and Carlqvist [58, 59] proposed a related but somewhat different model wherein a double layer forms in a solar magnetic flux tube when the electric current density becomes very large and exceeds some threshold. The electric field associated with the double layer would accelerate particles to high energy.

We report here laboratory observations from a new configuration of the Caltech lab experiment [17, 18, 20–22, 60] replicating solar coronal loops and interpret these observations in terms of a combination of the Parker nanoflare and the Alfvén/Carlqvist double-layer concepts. Specifically, transient localized 7.6 keV X-ray bursts, which we refer to as nanoflares, are observed to result from the instability of braided magnetic flux tubes containing 2 eV plasma. The phenomenological sequence leading to these bursts is determined by detailed observations using multiple interrelated diagnostics. These experimental results reveal a clear path where certain types of MHD dynamics precipitate fine-scale mechanisms, beyond the scope of MHD, that generate solar X-ray bursts and energetic particles.

4.2 Experimental Results

Figure 2.1 shows the experimental set-up. Plasma-filled, current-carrying magnetic flux tubes (plasma loops) are created by a magnetized electrode structure having multiple gas nozzles that can be open or closed to produce different plasma loop configurations. The plasma loops originate from the gas nozzle positions. This

arrangement enables creation of multiple braided strands. In this experiment, four holes are open on each electrode.

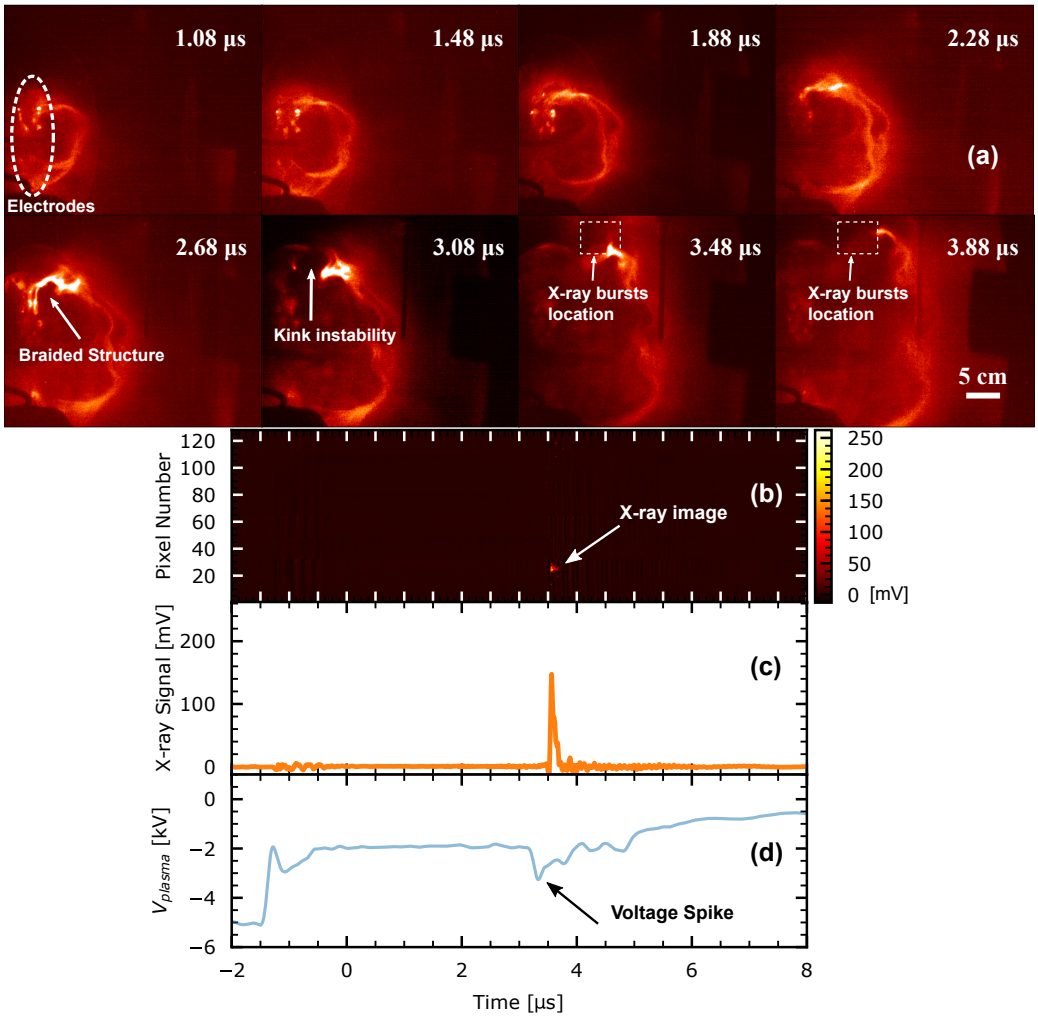

Figure 4.1: **Time series images of experimental plasma loop evolution and X-ray and voltage measurements** (a) A two-strand braided structure is observed in a time series images of hydrogen plasma loop evolution. With the expansion of the plasma loop, a kink instability occurs near the top of the loop. It chokes the strand radius down and breaks the strand at later time. A local hard X-ray burst is observed from the boxed regions in frames 7 and 8. The uncertainty in the origin of the X-rays is due to the size of the pinhole and the spread of the signal on the camera. Image is false colored. (b) A 1-D X-ray 'movie' of the solar loop plasma. A localized X-ray source is observed from pixels 20-30 at around 3.6 μs. (c) A line out of the PMT traces is shown. (d) The voltage across the electrode. Just prior to the X-ray burst, a transient voltage spike appears across the electrodes.

Figure 4.1 (a) shows a sequence of high-speed photographs made by an Imacon 200 camera showing the evolution of a braided structure of multiple current-carrying plasma loops. The main capacitor bank was charged to 5 kV for this sequence and the bias field coil was charged to 80 V. The braided structure consists of at least 2 strands on its upper part near the electrode (see 2.68 μs image). The hoop force resulting from the electric current flowing along the plasma loop drives a localized expanding bulge of the braided loop structure; this bulge becomes the kink instability seen in the 2.68 μs and 3.08 μs images. A kinking loop segment must lengthen as a result of the deformation of its axis but because ideal MHD instabilities such as a kink are incompressible [61], the volume of the segment must remain constant. To maintain constant volume, the radius of the segment must decrease and so the rapid lengthening of the loop segment by the kink chokes the loop radius so it becomes a thin filament and then finally breaks at 3.08-3.48 μs.

When the thin filament breaks, an X-ray burst is detected by the 128-channel X-ray detector array shown in Figure 2.1. A pinhole is put in front of the X-ray detector. The location of the X-ray source is determined by tracing a ray passing through the pinhole from where the ray intercepts the detector to where the ray intercepts the plasma loop. Using this procedure, the location of the source of the X-ray burst was determined to be near where the plasma loop breaks as indicated by the white box in the 3.48 and 3.88 μs frames. The uncertainty in where the X-rays originate, shown by the box size, results from the pinhole size and the signal spread on the detector array. As shown in Figure 4.1 (c) and (d), the X-ray burst occurs at the same time as a voltage spike measured across the plasma loop.

The detector array can alternatively be configured to measure X-ray energy; this is achieved by replacing the pinhole by multi-layer aluminum foils placed flush against the scintillators as shown in Figure 4.2 (a). Calibration for this energy-measuring mode is based on the X-ray intensity I through metal foil of thickness d having the dependence $I = I_0 e^{-\frac{d}{\lambda}}$ where I_0 is the incident signal and λ is a material- and energy-dependent attenuation length. The energy-dependence of the X-ray attenuation length for Aluminum (Al) is shown in Figure 4.2 (b) [62]. When an X-ray burst is incident on the detector configured as in Figure 4.2 (a), the signal is larger for detectors having fewer layers of aluminum foil. The X-ray attenuation length is determined by normalizing each group of signals to the control amplitude (channels with no foil) and then performing a linear regression on the log of the normalized signal. This measured attenuation length is then used to obtain the X-ray energy

by comparing to the attenuation length plot for Al in Figure 4.2 (b). Each group of 32 channels was considered separately in order to reduce the impact of signal variation across the 12.8 cm width of the detector and variation in the individual PMT modules. Figure 4.2 (c) shows the time-dependence of the 128 channel typical X-ray raw signal using the foil layers, and Figure 4.2 (d) shows the X-ray signal strength of the 128 channels with the Al filter location/strength overlayed as gray bars. Measurements from over 100 shots show that the X-ray energy ranges from 6 to 10 keV with an average of 7.6 keV. Seth built the camera. We measure the X-ray energy together.

The voltage spike indicates a sudden increase in the electrical resistance in series with the inductive circuit. This can be explained by two associated effects: (i) the development of a kinetic instability when the electron drift velocity $v_d = J_{axial}/ne$ associated with electric current exceeds a characteristic wave velocity such as Alfvén velocity and (ii) a geometric stretching effect. When the electron drift velocity exceeds a threshold, waves are destabilized and increase the local effective electrical resistivity [58, 63]. The fastest-growing ideal MHD instabilities are incompressible [61] which means that the volume of the kinking loop segment must remain constant during the kinking. However, when a loop segment kinks, the length l of the segment axis must increase as seen in Figure 4.1. The constraint that the segment is incompressible and so has constant volume requires $l\pi r^2 = const$, where r is the loop radius. The cross section πr^2 of the stretched loop segment thus decreases as the kinking stretches l; decrease of the loop cross-section means that the loop axial current density $J_{axial} = I/\pi r^2$ increases. The electron drift velocity J_{axial}/nq_e consequently increases and causes a kinetic instability that increases resistivity η. Furthermore and even without an increase in resistivity, the segment electrical resistance $R_{segment} = \eta l/\pi r^2$ will increase from the geometric stretching (increase in l/r^2). Thus, stretching not only can instigate a kinetic instability that would increase local η, but stretching also increases the resistance $R_{segment}$ simply from the change in aspect ratio. The sudden appearance of substantial resistance at the kink location has an effect equivalent to splicing a large resistor into the circuit at the location of the instability. The inductive energy of the entire circuit $LI^2/2$ could in principle be dumped into this region of increased resistivity. The large voltage jump along the length of the kinking loop strand segment resulting from LdI/dt would accelerate electrons and ions to extreme energies and the bremsstrahlung radiation of the electrons would produce X-rays.

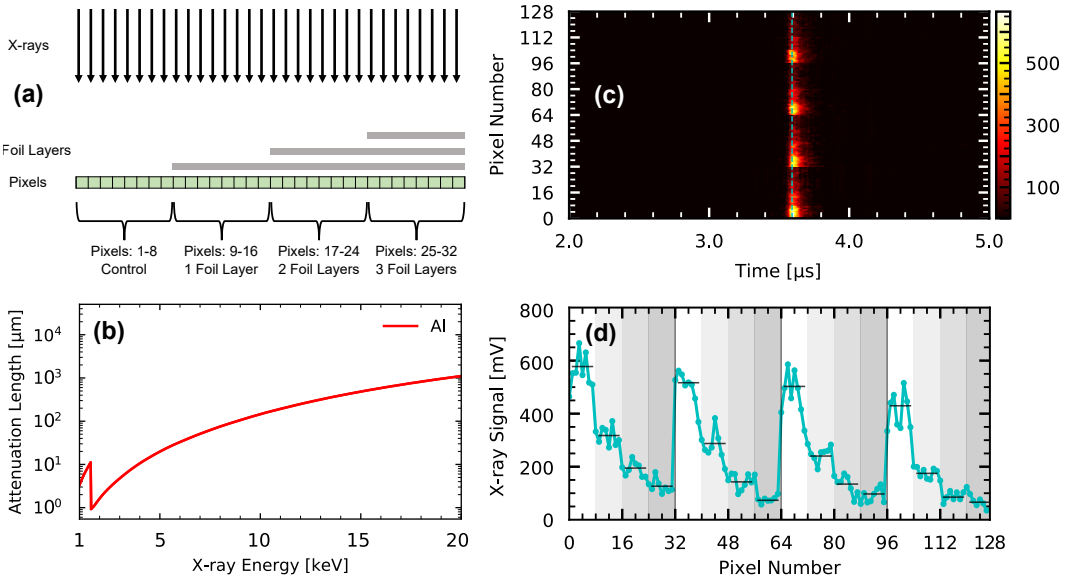

Figure 4.2: **X-ray energy measurements.** (a) A schematic diagram of the foil array placed in front of the scintillators of the X-ray detector. The foils arranged along the detector have either no additional foils (i.e., a control measurement), 36, 72, or 108 micron thick aluminum foils. (b) The NIST values of the attenuation length of X-rays of different energy through aluminum. The K-shell peak transmission window around 1.5 keV can be ignored because the polyimide window has a transmission fraction of $< 1 \times 10^{-6}$ for photon energies less than 2 keV, and the transmission fraction of the air between the window and the detector surface has a transmission fraction less than 0.01. (c) An example of the energy measurement. (d) An example line out of the measured signal. Gray bands indicate the filter placement, with darker bands indicating a thicker layer.

An electric circuit simulation verifies the idea that the voltage spike associated with the X-ray burst is induced from a sudden increase of resistivity. The LTspice circuit simulation software [64] is used to simulate the experimental circuit diagram presented in Figure 4.3 (a). As there are spikes both from voltage and current measurements shown in Figure 4.3 (c) and 4.3 (d), the resistance change should also be a spike-like peak function. To represent the cause of these spikes, as shown in Figure 4.3 (b), a Gaussian time-dependent function is used to describe the sudden transient increase of resistivity. This assumed time-dependent resistance causes the circuit model to produce voltage and current spikes that nearly duplicate the experimentally measured voltage and current spikes; this is seen by comparing Figure 4.3 (c) and (d) which are from the experiment with Figure 4.3 (e) and (f) which are from the circuit simulation. Seth suggested doing the circuit simulation, which we then both carried out together.

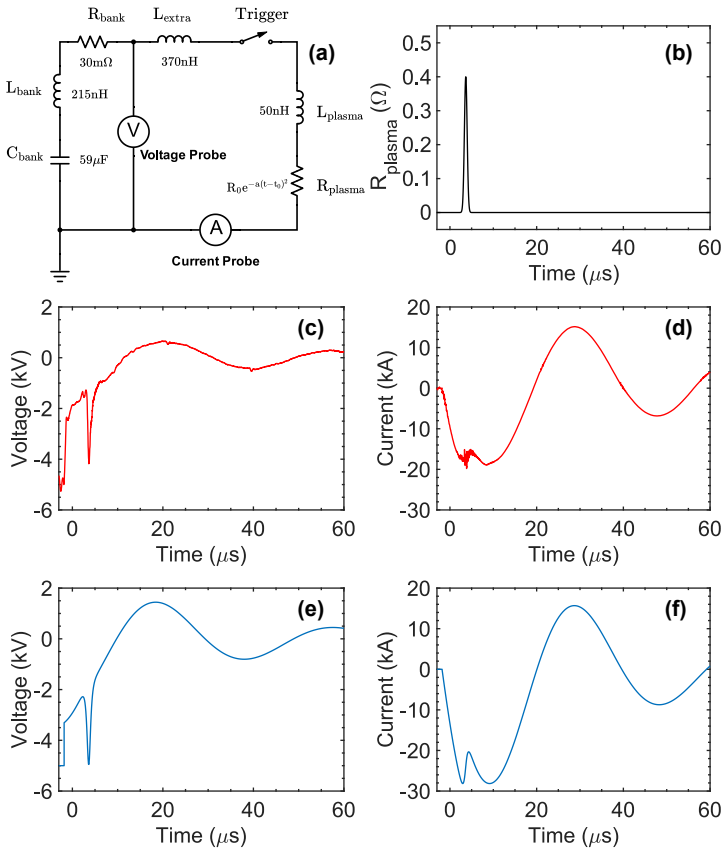

Figure 4.3: **Solar loop experiment circuit simulation.** (a) Experiment circuit diagram. The plasma part of the circuit is represented as an inductor and a time-dependent resistor. The plasma inductance is assumed to be 50 nH, which is obtained by simplifying the plasma loop as a half circle loop of wire with 5 cm loop major radius and 1 cm minor (wire) radius. The voltage and current spikes are both peak functions, so the corresponding resistance change is presumed to be also a peak function. We use Gaussian function $R_{plasma} = R_0 \exp(-a(t-t_0)^2)$ to represent the transient change of the plasma resistance where R_0 is the peak resistance value, and t_0 is the resistance peak time, and a is related to the full width at half maximum (FWHM). They are chosen according to the relative voltage spike amplitude, voltage peak time and the voltage spike FWHM. In the simulation, $R_0 = 0.4\ \Omega$, $t_0 = 3.65\ \mu$s and $a = 5\ \mu\text{s}^{-2}$ are used. The corresponding plasma resistance is plotted in (b). (c, d) Voltage and current measurement from experiment Shot # 9258. As shown in (a), the voltage measured in (c) is the voltage across the plasma part and an extra inductor. We also measured the voltage across the plasma part by connecting two voltage probes directly to the top electrode and bottom electrode and then subtracting the two voltages. The voltage trace across the plasma is similar but has a several kV larger voltage spike compared with (c). (e, f) Voltage and current curves from the simulation. Voltage and current spikes similar to the experimentally observed spikes are reproduced by the transient resistance increase.

To see why a kinetic instability should develop when a loop strand is choked, consider the situation when the electron drift velocity is near the Alfvén velocity. The loop strand has both an axial magnetic field B_z and a local azimuthal magnetic field B_φ where the latter is associated with the current density in the strand by Ampere's law via $\mu_0 J_z = r^{-1}\partial/\partial r\left(rB_\varphi\right)$. The ratio of electron drift velocity to the Alfvén velocity is [23]

$$\frac{v_\mathrm{d}}{v_A} = \frac{J_z}{ne}\frac{\sqrt{\mu_0 n m_i}}{B_z} = \sqrt{\frac{m_i}{\mu_0 n e^2}}\frac{1}{B_z r}\frac{\partial}{\partial r}\left(rB_\varphi\right) = \frac{d_i}{B_z r}\frac{\partial}{\partial r}\left(rB_\varphi\right).$$

If B_φ is of order B_z, v_d will become of order v_A if the length scale of r becomes of the order of d_i. The density of the hydrogen plasma loop is $n = 1\times10^{21}$ m^{-3} as measured from Stark broadening of the H_β line; the ion skin depth is thus $d_i = 0.72$ cm. Before the kink instability, the diameter of a single strand is thus very close to d_i. The choking of the strand by the kink instability will consequently reduce the strand radius to be smaller than d_i. This enables a kinetic instability in the choked strand which will increase the resistivity in the strand. This resistivity increase together with the increase in strand segment l/r^2 increases the local electrical resistance.

A magnetic Rayleigh Taylor instability (MRTI, or Kruskal–Schwarzschild instability [35]) can also occur in the plasma loop as shown in Figure 4.4 and the MRTI works similarly to the kink instability to choke the plasma strand radius down to the kinetic scale.

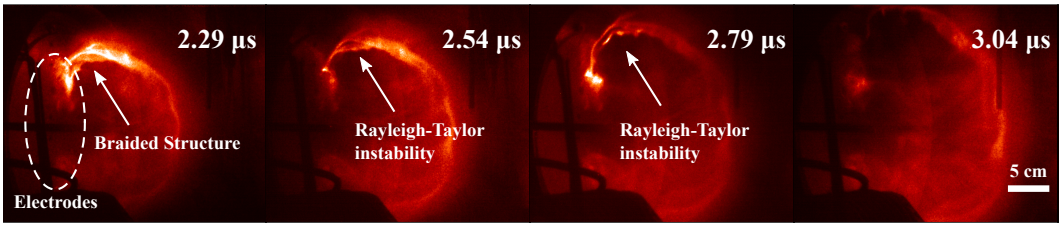

Figure 4.4: **Magnetic Rayleigh Taylor instability observation.** A four-strand braided structure is shown in time series images of hydrogen plasma loop evolution. With the expansion of the plasma loop, a magnetic Rayleigh Taylor instability occurs on the loop and plays the same role as a kink instability to choke the strand radius down and break the strand at later time.

We define a single X-ray burst as a laboratory nanoflare and sometimes observe multiple nanoflares. Figure 4.5 (a) shows an experiment shot where the plasma loop is composed of two separate strands. Two separate X-ray bursts are detected in Figure 4.5 (b) and two $\sim$ 3 kV spikes were measured as shown in Figure 4.5 (c).

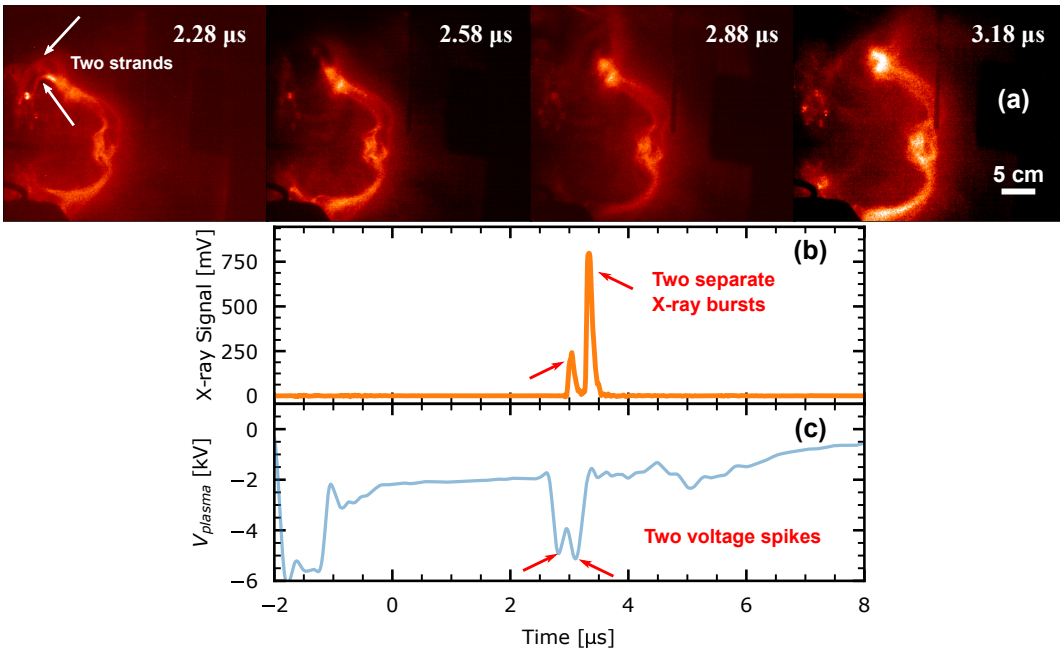

Figure 4.5: **Two experimental nanoflare events.** (a) The image shows a braided structure of 2 strands in a time series images of hydrogen plasma loop evolution. (b) X-ray traces are shown. They show two separate X-ray bursts. (c) The voltage across the electrodes. Just prior two separate X-ray bursts, two separate voltage spikes are measured.

These bursts and associated voltage spikes are presumed to be generated as each of the two strands went unstable and broke via the mechanism described above. Three laboratory nanoflares in one shot have also been observed.

4.3 Discussion

These experimental results suggest a multi-scale instability sequence wherein solar loops initially governed by ideal MHD dynamics kink which then chokes the current channel and trigger kinetic instability which then instigates opening-switch-like processes that cause solar X-ray bursts.

The MHD behavior reported here can be scaled to the many other situations governed by MHD because MHD has no intrinsic length scale. MHD scaling [2] allows for three free parameters: a_1, a_2, a_3, following invariant relations: $\frac{L_0}{a_1} \rightarrow L'$, $\frac{\rho_0}{a_2} \rightarrow \rho'$, $\frac{B_0}{\sqrt{a_3}} \rightarrow B'$, $\frac{P_0}{a_3} \rightarrow P'$, $\frac{1}{a_1}\sqrt{\frac{a_3}{a_2}}t \rightarrow t'$, $\sqrt{\frac{a_2}{a_3}}v_0 \rightarrow v'$ to transform a scale to another scale having the same plasma beta. This transformation gives a one-to-one correspondence between systems, allowing laboratory experimental plasmas to be scaled to equivalent systems in space plasmas. Table 4.1 shows characteristic

parameters of the experiment, the solar corona and the experiment scaled to the solar corona using $a_1 = 10^{-8}$, $a_2 = 1 \times 10^5$, $a_3 = 9 \times 10^2$. The scaled characteristic parameters have magnitudes similar to that of the solar corona.

Table 1 Experimental plasma parameters and scaling to the solar corona

	Experiment	Scaled Experiment	Solar Corona
Characteristic length L (m)	0.05	5×10^{6}	5×10^{6}
Characteristic time t (s)	10^{-6}	10	10
Magnetic field B (G)	3000	100	100
Mass density ρ(kg $\cdot$ m^{-3})	1.7×10^{-6}	1.7×10^{-11}	1.7×10^{-11}
Pressure P(Pa)	800	0.89	0.32
Alfven velocity v_A(m $\cdot$ s^{-1})	2.1×10^{5}	2.2×10^{6}	2.2×10^{6}
Plasma beta β	0.02	0.02	0.01
Lundquist number S	200		2×10^{13}
Ion skin depth d_i(m)	0.007		2

Table 4.1: **Plasma parameters of Caltech experiment and scaling to solar corona.** Typical values of the experiment (left column) are scaled according to the MHD scaling described in the text. The scaled values (center column) are in good agreement with approximate values for the solar corona (right column). This close correspondence indicates magnetohydrodynamic similarity between the two systems and the relevance of the experimental parameter regime to that of the solar corona. The experiment plasma has a density 10^{21} m^{-3} and a temperature 5 eV. The solar corona has a density 10^{16} m^{-3} and a temperature 200 eV [14].

A critical distinction between the lab and solar situations is that the initial state of the lab experiment is much closer to kinetic instability than at first consideration would apparently be the case for the solar situation. The initial current channel radius in the experiment is around d_i so that the kink instability does not have to choke the current channel cross-section very much. In contrast, the nominal radius of a solar coronal loop is of order of 10^6 m whereas the ion skin depth for nominal solar corona densities is of order of 1 to 10 m. The length of the solar loop would have to increase by an unrealistically large amount to choke the 10^6 m radius to be of the order of 10 m. The solar situation could nevertheless develop a kinetic instability on realizing that a solar coronal flux rope is not monolithic but instead is a fractal braid of successively smaller braided filamentary flux ropes, i.e., strands. The finest strand would be close to ion skin depth, i.e., ~10 m to ~100 m. Because of this fractal braiding, an MHD instability only has to choke an individual finest MHD-governed strand by a small factor to instigate kinetic instability.

A finest scale structure of 10 m is consistent with the required magnetic field diffusion time. Solar loops are stable for time scales of hours and have an internal axial current providing the $\mathbf{J} \times \mathbf{B}$ inward force that balances outward forces from

the pressure gradient in the direction of the loop radius. The time for this current to become distributed over the loop cross section is the magnetic field diffusion time $\tau_r = \mu_0 r^2/\eta$, where r is the radius and η is the resistivity. The temperature of a solar corona loop is $T = 200$ eV so Spitzer resistivity gives $\eta = 7 \times 10^{-7}\ \Omega \cdot \mathrm{m}$. Thus, a 3600 s diffusion time corresponds to a 45 m radius. If the solar corona loop were a monolithic structure (like a solid copper wire) having a 10^6 m radius rather than being constituted by fractal strands, the magnetic field diffusion time would be 6×10^4 yr which is orders of magnitude greater than observed characteristic solar magnetic field evolution time scales. This implies that a fractal structure is necessary for a solar corona loop to have a distributed current. Filamentary decomposition of a flux rope is analogous to Litz wire [65], which is composed of braided tiny, insulated wire strands. This structure can enhance current penetration compared with a single monolithic conductor and so links more interior flux and increases the inductance [66].

The essential components of this mechanism have been separately observed in nature. Solar observations imply that coronal loops are composed of braided flux ropes because, as imaging resolution has increased over the years, each improvement in resolution has revealed finer-scale structure [14]. Braided loop structures have commonly been observed on the Sun, for example by the High-resolution Corona Imager [49]. Fast-growing ideal MHD instabilities such as the kink instability and the magnetic Rayleigh Taylor instability are common in solar loop structures [30, 67]. Previous study has shown that a large current flows through the solar loop and the current disruption from LdI/dt can generate voltage spikes up to 10^6 kV [58]. Fleishman et al. measured the rapid magnetic field decay in a solar flare region, which implies a strong inductive electric field [51, 53] with associated voltage spike $V = -d\phi/dt = -LdI/dt$ where the magnetic flux is $\phi = \int \mathbf{B} \cdot d\mathbf{S} = LI$ and I is the electric current. Nanoflares have also been observed [50, 52].

A specific highly-relevant example is the kink-driven solar flare observed in active region NOAA 11163 on February 24, 2011 [68] which had an evolution very similar to what was observed in the Caltech lab experiment. Compared with the Caltech experiment, it has a bigger length scale (20 Mm) but a slower time scale (10 s). The MHD behavior of both situations can be scaled and compared using Table 4.1. Figure 4.5 (a-c) presents high-resolution observations of this kink-driven solar flare as observed by the Solar Dynamics Observatory (SDO)/Atmospheric Imaging Assembly (AIA) [54] while Figure 4.5 (d-f) show the comparable situation in the

Caltech lab experiment. In both the active region and the lab experiment, a kink instability developed on a loop segment and in both cases the axial stretching produced by the kink chokes the radius of the segment and then the choked segment breaks. Figure 4.5 (g) shows the hard X-ray signal from RHESSI [69] for the solar kink-driven instability and Figure 4.5 (h) shows the X-ray signal from the lab experiment.

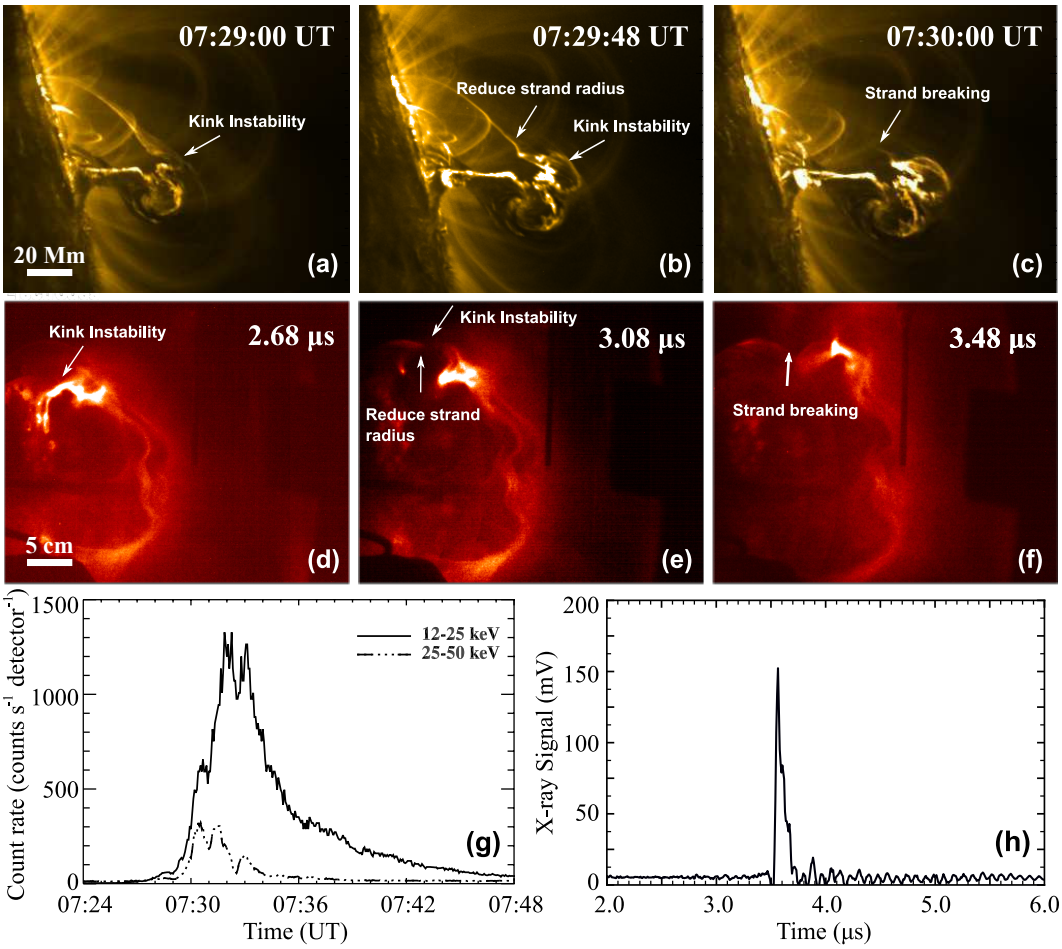

Figure 4.5: **Comparison between solar observation and experimental observation.** (a-c) SDO/AIA 171 (T~0.6 MK) Å EUV images showing the development of kink instability, associated CME, and flare which occurred in active region NOAA 11163 on 2011 February 24. (d-f) Experimental images showing the similar process as (a-c). (g) RHESSI hard X-ray flux profiles (12–25 and 25–50 keV). Hard X-ray bursts are observed during the process. (h) hard X-ray signals observed in the experiment associated with this process. (a, b, c, g) are reproduced by permission of the AAS [68].

It is thus reasonable to propose the following path for how solar eruptions create energetic particles and X-rays: (i) A solar flux rope is conjectured to be a braid of

a very large number of fine-scale flux ropes with the finest scale being somewhat larger than d_i; (ii) Electric current flows along the flux rope and the corresponding hoop force causes a segment or segments of the flux rope to bow out; (iii) Each strand then develops a fast-growing MHD instability, such as the kink instability or magnetic Rayleigh Taylor instability which then chokes the strand down to a critical scale at which time kinetic instabilities develop and, together with the stretching of the length of the unstable strand, increase the resistance of the choked segment; (iv) This increase in resistance corresponds to an opening switch so the inductive energy of the entire circuit would be dumped into this region of increased resistance; (v) A high voltage drop resulting from LdI/dt would accelerate electrons and ions to extreme energies and the bremsstrahlung radiation of the electrons would produce X-rays.

The particle acceleration mechanism proposed here is also likely relevant to space and astrophysics regimes. A similar voltage spike double layer structure has been observed in Earth's plasma sheet and identified as a cause for particle accelerations [70].

Chapter 5

BRAIDED MAGNETIC FLUX ROPES EQUILIBRIUM

1. Zhang, Y. & Bellan, P. M. Magnetic double helix. (under review) (2024).

Braided magnetic flux ropes are observed from the experiment and the solar coronal loops. However, there is no model describing the braided structure. In this chapter, we developed a method for constructing the equilibrium of braided magnetic flux ropes.

Magnetic flux ropes, the fundamental building block of magnetohydrodynamic plasma configurations, have often been observed to wrap around each other to form a helical braided structure with net axial current. Braiding has been observed in astrophysical jets, solar coronal loops, and laboratory experiments. The equilibrium of braided flux ropes is more complicated than familiar axisymmetric systems because it requires balancing forces between the individual braids. We present here a method for constructing these equilibria. This method generates a double helix equilibrium with net axial current which is characteristic of observed solar loops and of laboratory-produced braided magnetic flux ropes. To the best of our knowledge, no previous model has been able to describe braided structures with net axial current and instead have only described braided structures with no net axial current; these no-net current structures had equal-magnitude positive and negative axial currents. The net-axial-current equilibrium presented here reproduces the observed braided structure of the double helix nebula and is expected to be a powerful tool in other contexts.

5.1 Introduction

Braided magnetic flux ropes have often been observed in solar and astrophysical contexts. Examples are the interwoven braided magnetic strands of solar loops [49], solar prominence [71], the magnetic clouds in the solar wind [72], the double helix nebula [73], and the double helix structure in Massive Galaxy's Jet M87 [74]. These examples demonstrate the complexity of magnetic fields in different settings. Similar structures have also been produced in laboratory experiments, for example two interacting braided magnetic flux ropes with the same-direction axial currents have been reported [75]. Contrary to expectations, these flux ropes which were

wrapped around each other, did not merge like parallel current wires but instead moved closer and then bounced back. This behavior indicates a more complex interaction than previously assumed. Additionally, in the UCLA large plasma device experiment [76], a similar dual braided flux rope structure was created, with spiky voltage signals detected, presumably linked to magnetic reconnection between the two strands. This suggests a dynamic interplay between magnetic fields in such configurations. In the Caltech solar loop experiments, braided loop structures were produced [77], with different strands behaving independently during an instability cascade. The bursting of individual strands was observed to produce hard X-rays, indicating the production of high-energy particles during these events. Similar helical structures were also observed in toksmak experiments [78], reversed field pinch experiments [79], Z-pinch experiments [80], spheromak experiments [81], and plasma jet experiments [82, 83]. Braiding and strand-strand interaction are likely to be fundamental to magnetic flux rope dynamics [84]. It has been noted by Marshall and Bellan [85] that a braided structure is a lower-energy configuration than an unbraided structure containing the same magnetic flux; this implies it is energetically favorable for systems to be braided in flux-conserving configurations.

A helically symmetric system is the most basic braided system. Using cylindrical coordinates (r, θ, z), a system with helical symmetry depends only on radial distance r and the helical parameter $u = \theta - kz$. Setting $u =$ const for fixed r generates a helical line in space and all physical scalars remain invariant along this helical line. An MHD equilibrium differential equation having helical symmetry has been previously derived and is known as the generalized Grad-Shafranov equation or the JOKF equation [86]. Due to the complexity of this differential equation, only a solution with alternating J_z polarity and no net current has been reported [87] and this is only obtained under restrictive linear assumptions. The derivation of an equilibrium solution where all strands have the same J_z polarity so there is a net axial current has remained elusive. This is important because, unlike a no-net-current configuration such a solution would be susceptible to kinking and associated expansion from hoop forces as observed in actual braided solar structures and in laboratory experiments.

We now show via a thought experiment that it is possible to construct a braided magnetic flux rope equilibrium where all strands have the same J_z polarity. Specifically, Figure 5.1 shows braided current wires having a range of axial angular wavenumbers $k = 2\pi/\lambda$ where λ is the axial wavelength of the helical wire. When λ goes to

infinity, corresponding to k going to zero, the two wires are parallel. As they have same-direction axial current, the two wires attract each other. In contrast, when k goes to infinity, the two wires form two interspersed tightly coiled same-direction solenoids, and the interaction force is now radially outward. As the physics is continuous from $k = 0$ to $k = \infty$, there must be an intermediate state k_{eq} where the interaction force vanishes. This state represents the equilibrium state of the system.

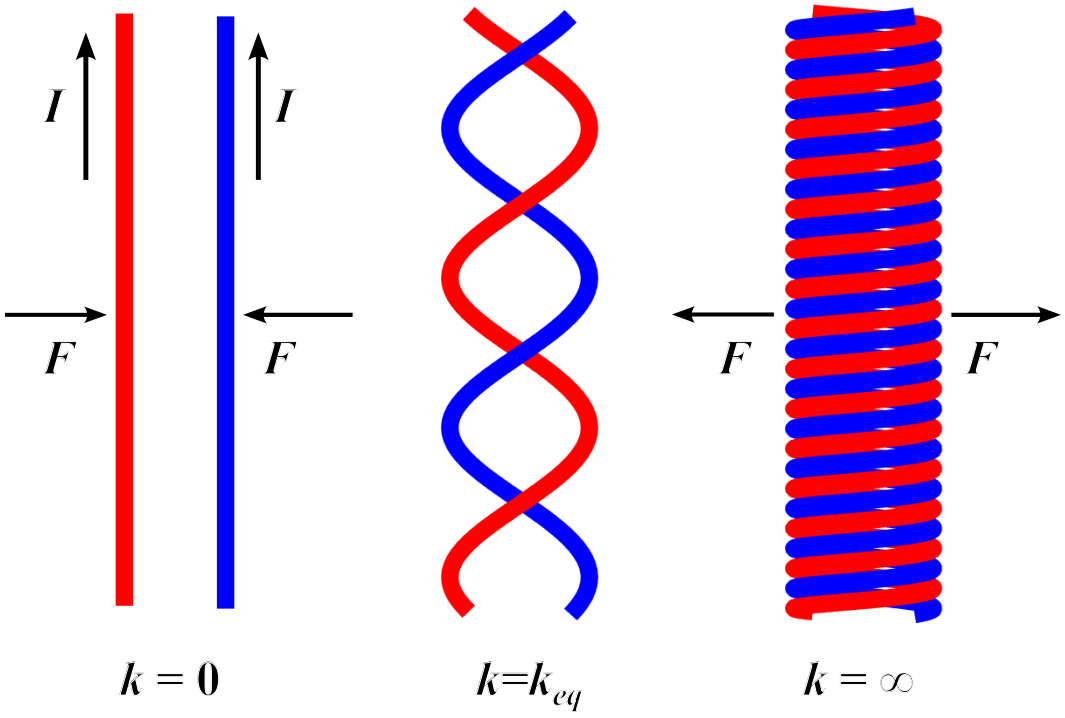

Figure 5.1: **A thought experiment on the interaction between two helically braided current wires under different angular wavenumbers.** The $k = 0$ corresponds to two parallel current wires. They attract each other. The $k = \infty$ corresponds to tightly coiled solenoids. The two helical wires repel each other. As the physics should be continuous, there must be a $k = k_{eq}$ as presented in the middle with a zero interaction force. This corresponds to the equilibrium state.

We present here a model that successfully produces an equilibrium of two braided magnetic flux ropes with $J_z \geq 0$ everywhere. This could, for example, represent a braided solar corona loop carrying a net axial current. The magnetic field of a "point source" helical current wire is first established and then, via the Green's function method, is used to obtain the magnetic field of a distributed current. The net magnetic force summed over the cross-section of one of the two finite-cross-section helical wires is calculated from the current distribution in the wire and the

magnetic field constructed using the Green's function method. Equilibrium is found by determining the parameters for which this net force vanishes. This successfully reproduces the observed braided structure of the double helix nebula [73].

5.2 Helical Current Wire Model

To derive the Green's function, we begin by considering an infinitely long wire that follows a helical path having radius r' and axial wavenumber k. The wire has zero radius and carries a current I with $\mathbf{J}\left(r,\theta,z\right)=Ir^{-1}\delta\left(r-r'\right)\delta\left(\theta-kz-\varphi'\right)\left(\hat{z}+kr'\hat{\theta}\right)$. At $z=0$ the wire is located at azimuthal position φ'; this dependence on r' and φ' will enable a later construction with multiple wires where each has a different r' and φ'. The wire thus is at $r(z)=r'$, $\theta(z)=kz+\varphi'$.

The magnetic field produced by the helical wire is potential for $r<r'$ and for $r>r'$ with a jump at $r=r'$ determined by the current in the wire. Using these properties the magnetic field is derived via the discontinuous vacuum magnetic field method [88] to be

$$
r<r'\begin{cases}
B_r\left(r,\theta,z\right)=\dfrac{\mu_0 I}{\pi}k^2r'\displaystyle\sum_{n=1}^{\infty}nK'_n\left(nkr'\right)I'_n\left(nkr\right)\sin\left[n\left(\theta-kz-\varphi'\right)\right]\\
B_\theta\left(r,\theta,z\right)=\dfrac{\mu_0 I}{\pi}kr'\dfrac{1}{r}\displaystyle\sum_{n=1}^{\infty}nK'_n\left(nkr'\right)I_n\left(nkr\right)\cos\left[n\left(\theta-kz-\varphi'\right)\right]\\
B_z\left(r,\theta,z\right)=\dfrac{\mu_0 I}{2\pi}k-\dfrac{\mu_0 I}{\pi}k^2r'\displaystyle\sum_{n=1}^{\infty}nK'_n\left(nkr'\right)I_n\left(nkr\right)\cos\left[n\left(\theta-kz-\varphi'\right)\right]
\end{cases}
$$

$$
r>r'\begin{cases}
B_r\left(r,\theta,z\right)=\dfrac{\mu_0 I}{\pi}k^2r'\displaystyle\sum_{n=1}^{\infty}nI'_n\left(nkr'\right)K'_n\left(nkr\right)\sin\left[n\left(\theta-kz-\varphi'\right)\right]\\
B_\theta\left(r,\theta,z\right)=\dfrac{\mu_0 I}{2\pi r}+\dfrac{\mu_0 I}{\pi}kr'\dfrac{1}{r}\displaystyle\sum_{n=1}^{\infty}nI'_n\left(nkr'\right)K_n\left(nkr\right)\cos\left[n\left(\theta-kz-\varphi'\right)\right]\\
B_z\left(r,\theta,z\right)=-\dfrac{\mu_0 I}{\pi}k^2r'\displaystyle\sum_{n=1}^{\infty}nI'_n\left(nkr'\right)K_n\left(nkr\right)\cos\left[n\left(\theta-kz-\varphi'\right)\right].
\end{cases}
\tag{5.1}
$$

This magnetic field has the properties that (i) B_r is continuous at $r=r'$, (ii) there is an axial field $B_z=\frac{\mu_0 I}{2\pi}k$ for $r\ll r'$ as befits a radius r' solenoid wound of a wire with pitch $2\pi/k$, (iii) for $r\gg r'$ there is an azimuthal field $B_\theta=\frac{\mu_0 I}{2\pi r}$ as befits an axial wire with current I, (iv) there are jumps in B_θ and B_z at $r=r'$ corresponding to the current in the wire, and (v) the field is potential for $r<r'$ and for $r>r'$.

The magnetic field prescribed by Equation (5.1) is from a point-source helical current. Using the Green's function method, we obtain the magnetic field of a distributed current by replacing the current I with an area integration over the current density of the distributed current. Because the current flowing in the helical wire can be completely specified by prescribing J_z in the $z = 0$ plane, we define $J_{z0}(r', \varphi') = J_z(r', \varphi' - kz, z = 0)$.

We consider a thin helical wire with current $dI = J_{z0}(r', \varphi')\, r' dr' d\varphi'$; this current flows through an annular sector in the $z' = 0$ plane located between r' and $r' + dr'$ and between φ' and $\varphi' + d\varphi'$. Using Equation (5.1), the radial magnetic field provided by this current dI is

$$dB_r(r, \theta, z) = \begin{cases} \text{for } r < r' \\ \dfrac{\mu_0 J_{z0}(r', \varphi')\, r' dr' d\varphi'}{\pi} k^2 r' \\ \times \displaystyle\sum_{n=1}^{\infty} n K'_n(nkr')\, I'_n(nkr) \sin[n(\theta - kz - \varphi')] \\ \text{for } r > r' \\ \dfrac{\mu_0 J_{z0}(r', \varphi')\, r' dr' d\varphi'}{\pi} k^2 r' \\ \times \displaystyle\sum_{n=1}^{\infty} n I'_n(nkr')\, K'_n(nkr) \sin[n(\theta - kz - \varphi')] \end{cases} . \tag{5.2}$$

The radial magnetic field generated from a helical current distribution is then the integral of Equation (5.2) over all (r', φ') to give

$$\begin{aligned} B_r(r, \theta, z) = &\int_r^{\infty} dr' \int_0^{2\pi} d\varphi' \left\{ \begin{array}{l} \frac{\mu_0 J_z(r', \varphi')}{\pi} k^2 r'^2 \\ \times \sum_{n=1}^{\infty} n K'_n(nkr')\, I'_n(nkr) \sin[n(\theta - kz - \varphi')] \end{array} \right\} \\ &+ \int_0^{r} dr' \int_0^{2\pi} d\varphi' \left\{ \begin{array}{l} \frac{\mu_0 J_z(r', \varphi')}{\pi} k^2 r'^2 \\ \times \sum_{n=1}^{\infty} n I'_n(nkr')\, K'_n(nkr) \sin[n(\theta - kz - \varphi')] \end{array} \right\} . \end{aligned} \tag{5.3}$$

Similarly, the azimuthal magnetic field and the axial magnetic field can be derived as

$$B_\theta(r,\theta,z) = \int_r^\infty dr' \int_0^{2\pi} d\varphi' \left\{ \begin{array}{l} \frac{\mu_0 J_z(r',\varphi')}{\pi} kr'^2 \frac{1}{r} \\ \times \sum_{n=1}^{\infty} nK'_n(nkr') I_n(nkr) \cos\left[n(\theta - kz - \varphi')\right] \end{array} \right\} + \int_0^r dr' \int_0^{2\pi} d\varphi' \left\{ \begin{array}{l} \frac{\mu_0 J_z(r',\varphi') r'}{2\pi r} + \frac{\mu_0 J_z(r',\varphi')}{\pi} kr'^2 \frac{1}{r} \\ \times \sum_{n=1}^{\infty} nI'_n(nkr') K_n(nkr) \cos\left[n(\theta - kz - \varphi')\right] \end{array} \right\} \tag{5.4}$$

$$B_z(r,\theta,z) = \int_r^\infty dr' \int_0^{2\pi} d\varphi' \left\{ \begin{array}{l} \frac{\mu_0 J_z(r',\varphi') r'}{2\pi} k - \frac{\mu_0 J_z(r',\varphi')}{\pi} k^2 r'^2 \\ \times \sum_{n=1}^{\infty} nK'_n(nkr') I_n(nkr) \cos\left[n(\theta - kz - \varphi')\right] \end{array} \right\} - \int_0^r dr' \int_0^{2\pi} d\varphi' \left\{ \begin{array}{l} \frac{\mu_0 J_z(r',\varphi')}{\pi} k^2 r'^2 \\ \times \sum_{n=1}^{\infty} nI'_n(nkr') K_n(nkr) \cos\left[n(\theta - kz - \varphi')\right] \end{array} \right\}. \tag{5.5}$$

Different localized current density distribution $J_{z0}(r', \varphi')$ can be constructed to model various braided flux ropes situations. Let us consider the simplest multi-strand helical situation, namely two helically braided current wires each with uniform current density on a circular cross-section having a radius b in the $z = 0$ plane. The respective centers of these two circular cross sections are at $r = a$, $\theta = 0$ and at $r = a$, $\theta = \pi$ and through each circular cross-section there is a uniform axial current density J_{z0}. The interiors of the two circular cross-sections are defined by $(x \pm a)^2 + y^2 \leq b^2$. Since the wires are helical, the vector current density is $\mathbf{J} = J_{z0}\left[\hat{z} + kr'\hat{\theta}\right]$ inside the two circular cross-sections while outside, $\mathbf{J} = 0$. The magnetic field resulting from this current distribution is derived in the Appendix A as Equations (A.5–A.6) using Equations (5.3–5.5). The area of each circular cross section in the $z = 0$ plane is $S = \pi b^2$.

The internal pressure distribution in a closed box cannot exert a net body force on the box because if this happened, the box would be "pulling itself up by its own bootstraps". This implies that $\int_S dS \nabla P = 0$ showing that the internal pressure distribution in a wire cannot exert a body force on the wire. Thus, the only possible net body force on each of the two wires in the double helix is the magnetic force but in a static equilibrium there must be no net force so $\mathbf{f} = \int_S dS \mathbf{J} \times \mathbf{B} = 0$. Consequently,

the equilibrium condition is that on each wire the net magnetic force per length is

$$\mathbf{f} = \int_S dS \mathbf{J} \times \mathbf{B} = 0. \tag{5.6}$$

Consider the magnetic force on the wire having a circular cross-section in the $z = 0$ plane centered at $r = a$ and $\theta = 0$. The integration region S is $(x-a)^2 + y^2 \leq b^2$. The three components of $\mathbf{f}$ are:

$$f_x = \int_S dS J_{z0} \left[((krB_z - B_\theta)\cos\theta - B_r \sin\theta) \right] \tag{5.7}$$

$$f_y = \int_s dS J_{z0} \left[((krB_z - B_\theta)\sin\theta + B_r \cos\theta) \right] \tag{5.8}$$

$$f_z = \int_S dS J_{z0} \left[-krB_r \right]. \tag{5.9}$$

Since each component of $\mathbf{B}$ is proportional to J_{z0}, each component of $\mathbf{f}$ is proportional to J_{z0}^2 and so is insensitive to the sign of J_{z0}. If it were assumed that $f_y > 0$, then, from symmetry, there would be a body force in the $+\hat{\theta}$ direction on both circular cross-sections. This body force would cause the entire system to spin up in the $+\hat{\theta}$ direction and so gain angular momentum. Since the system is self-contained, it cannot change its own angular momentum and so f_y must vanish. A similar argument indicates that f_z must vanish. However, since f_x corresponds to the radial direction, a finite f_x would not change the center of mass velocity of the system. Thus, f_x could be finite, and, if so, would cause a radial expansion or contraction of the helix; i.e., a change in the radial separation between the two circular cross-sections. Thus, there is only a radial force between the two helical wires. A more detailed mathematical proof for $f_y = f_z = 0$ is presented in the Appendix A.

To simplify the notation we define dimensionless lengths normalized to a, so $\bar{x} = x/a$, $\bar{b} = b/a$, $\bar{k} = ka$. We additionally define the dimensionless force $\bar{f_x} = f_x \Big/ \left(\frac{\mu_0 J_{z0}^2 \pi^2 b^4}{4\pi a} \right)$, and dimensionless magnetic field $\bar{\mathbf{B}} = \mathbf{B} \Big/ \left(\frac{\mu_0 J_{z0} b^2}{4a} \right)$. When $\bar{k} = 0$, $\bar{f_x} = -1$. This agrees with the attractive force between two parallel current wires each having a radius b and having centers separated a distance $2a$ as this force is $\mu_0 J_z^2 \pi^2 b^4 / 4\pi a$.

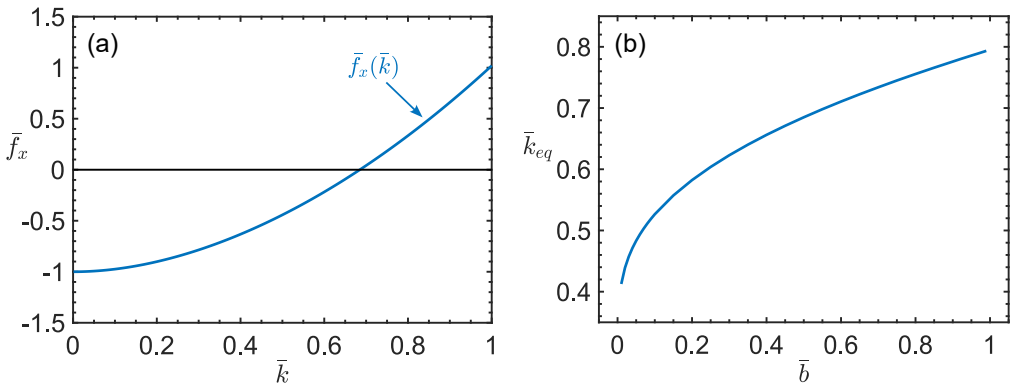

Figure 5.2: **Equlibrium of two helically braided current wires.** (a) $\bar{f}_x$ versus $\bar{k}$ under $\bar{b} = 0.5$. $\bar{f}_x = 0$ corresponds to the equilibrium state, and k_{eq}=0.685. (b) The equilibrium axial wavenumber $\bar{k}_{eq}$ versus minor radius $\bar{b}$.

5.3 Main Results

Figure 5.2(a) shows $\bar{f}_x$ plotted as a function of $\bar{k}$ for $\bar{b} = 0.5$. This plot shows that as $\bar{k}$ increases, $\bar{f}_x$ changes from being negative (attractive force) to being positive (repulsive force) as was shown qualitatively in Figure 5.1. In particular, Figure 5.2(a) shows that, for $\bar{b} = 0.5$, $\bar{f}_x = 0$ occurs at $\bar{k}_{eq} = 0.685$; this is the equilibrium. The value of $\bar{k}_{eq}$ at which equilibrium occurs depends on $\bar{b}$; this dependence is shown in Figure 5.2(b). It is seen that $\bar{k}_{eq}$ is an increasing function of $\bar{b}$, indicating that the double helix equilibrium of thicker braided current wires (bigger $\bar{b}$) has a shorter axial wavelength.

Figure 5.3 provides a detailed visualization of the physical characteristics of the equilibrium state for a helically braided magnetic flux rope system with $\bar{b} = 0.5$ and $\bar{k}_{eq} = 0.685$. Figure 5.3(a) shows a projection of the helically braided current wire structure in the $\bar{y} = 0$ plane. This projection shows two entwined current wires; for clarity, the two wires are illustrated using different colors, but it should be realized that the two wires have identical physical properties. Figures 5.3(b)-(e) show various physical quantities in the $\bar{z} = 0$ plane; physical quantities at different $\bar{z}$ can be determined from $\bar{z} = 0$ solutions utilizing the helical symmetry. Figure 5.3(b) shows the axial current density $\bar{J}_z = J_z/J_{z0}$ while Figure 5.3(c) shows the azimuthal current density $\bar{J}_\theta = J_\theta/J_{z0}$. Figure 5.3(d) shows $\bar{\mathbf{B}}_\perp$, the magnetic field component perpendicular to $\hat{z}$, as lines following $\bar{\mathbf{B}}_\perp = \bar{B}_x\hat{x} + \bar{B}_y\hat{y}$; it is seen that the $\bar{\mathbf{B}}_\perp$ lines encircle the two current centers. If the perpendicular magnetic field component is written as $\bar{\mathbf{B}}_\perp = \bar{B}_r\hat{r} + \bar{B}_\theta\hat{\theta}$, it is seen that $\bar{B}_r$ is an odd function of θ and $\bar{B}_\theta$ is an even function of θ; The colors in Figure 5.3(d) show the amplitude

$\bar{B}_\perp = \sqrt{\bar{B}_x^2 + \bar{B}_y^2}$. Figure 5.3(e) shows $\bar{B}_z$ which is largest at radii internal to the braided helical wires and reverses direction on moving from inside to outside the helix. It is seen that $\bar{B}_z$ is an even function of θ. These symmetries of $\bar{B}_r$, $\bar{B}_\theta$, and $\bar{B}_z$ justify the conclusion that $f_y = f_z = 0$.

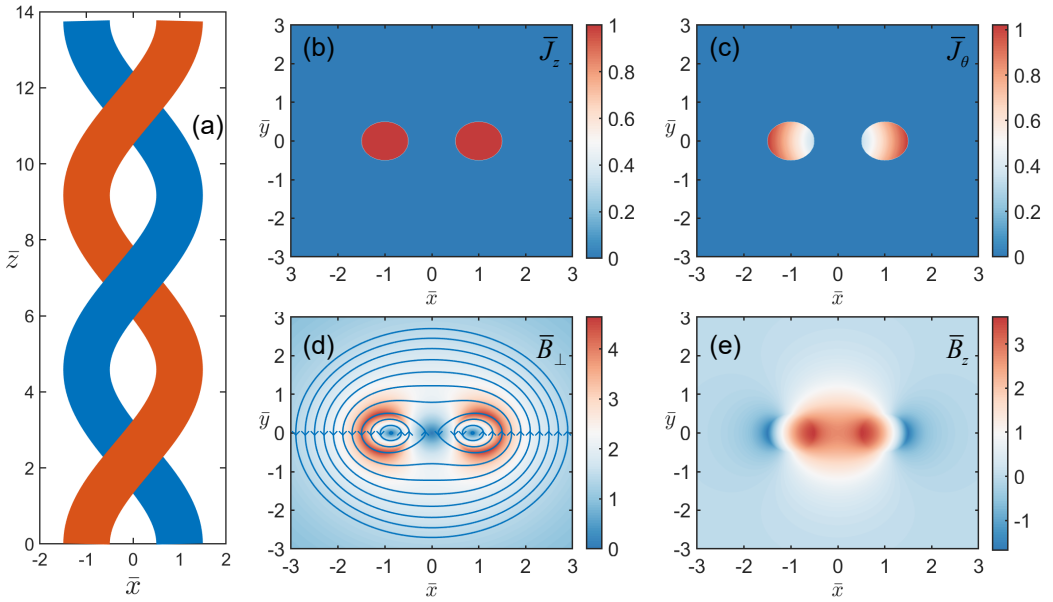

Figure 5.3: **Braided double helix equilibrium with $\bar{b} = 0.5$ and $\bar{k}_{eq} = 0.685$.** (a) The equilibrium diagram with two braiding current wires. Two colors are used to distinguish the two wires but they are the same. The physical quantities on the $\bar{z} = 0$ plane are plotted in (b-e). (b) The axial current density $\bar{J}_z = J_z/J_{z0}$ distribution. Uniform axial current distributes inside of the cross-section (c) The azimuthal current density $\bar{J}_\theta = J_\theta/J_{z0}$ distribution. (d) The $x-y$ direction magnetic field lines $\bar{\mathbf{B}}_\perp = \bar{B}_x\hat{x} + \bar{B}_y\hat{y}$ and, as colored shading, corresponding amplitude $\bar{B}_\perp = \sqrt{\bar{B}_x^2 + \bar{B}_y^2}$. (e) The axial magnetic field $\bar{B}_z$ distribution.

The equilibrium is determined from the surface integral of the magnetic field force equaling zero, i.e., $f_x = 0$. Inside the circular current-carrying cross section, the local magnetic force $\mathbf{J} \times \mathbf{B}$ force can be finite, as shown in Figure 5.4(a) and this force acts to pinch the current wire. This non-zero magnetic force can be balanced by an internal pressure gradient ∇P. Integration of $\nabla P = \mathbf{J} \times \mathbf{B}$ gives an internal pressure profile in the wire $\bar{P} = P \Big/ \left(\frac{\mu_0 J_{z0}^2 b^2}{4} \right)$. This internal pressure profile is shown in Figure 5.4(b). $\nabla P = \mathbf{J} \times \mathbf{B}$ requires $\nabla \times (\mathbf{J} \times \mathbf{B}) = 0$. The magnetic field generated from constant current density wires as the double helix current wires automatically satisfies this curl-free condition $\nabla \times (\mathbf{J} \times \mathbf{B}) = 0$. Details are discussed in the Appendix A.

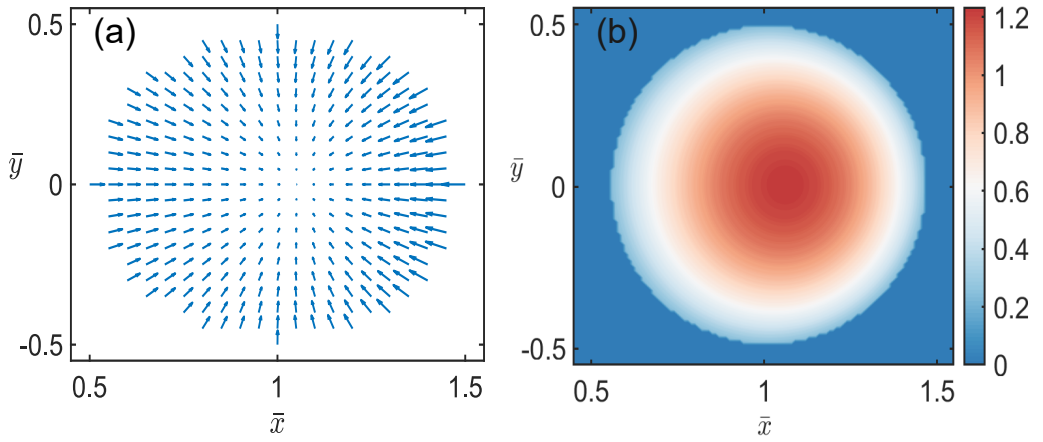

Figure 5.4: **Magnetic force inside of one current wire and the reconstructed pressure profile** (a) magnetic force $\mathbf{J} \times \mathbf{B}$ on $\bar{z} = 0$ plane. (b) the reconstructed pressure profile from $\nabla P = \mathbf{J} \times \mathbf{B}$.

We have thus provided a systematic method for determining the equilibrium of helically braided systems. This method is straightforward to implement, involving several key steps: (i) define a current distribution function to represent the helically braided system; (ii) determine the equilibrium state by setting to zero the net magnetic force over the cross-section of one current carrying wire; (iii) calculate the equilibrium magnetic field using Equations (5.3–5.5) and build the pressure distribution from $\nabla P = \mathbf{J} \times \mathbf{B}$. An important corollary of this method is that it could be used to construct a fractally braided system analogous to a braided rope where each rope braid is composed of strands that, in turn, are composed of smaller braided strands.

We can reproduce observed helically braided structures using the simple double helix equilibrium derived from this helical current two-wire model. A specific example is the braided structure of the double helix nebula [73], shown in Figure 5.5(a). The minor radius is measured as $\bar{b} \approx 0.3$, and the axial angular wavenumber $\bar{k} \approx 0.6$. We assume the two wires have the same direction current and this current is uniformly distributed on a circular cross-section. Using $\bar{b} = 0.3$, the helical wire model yields an equilibrium $\bar{k} = 0.623$, which is in excellent agreement with the observed value. Figure 5.5(b) shows the double helix structure predicted by the helical wire model presented here oriented as in the telescope photo and shows that this closely replicates the intricate structure of the double helix nebula in Figure 5.5(a).

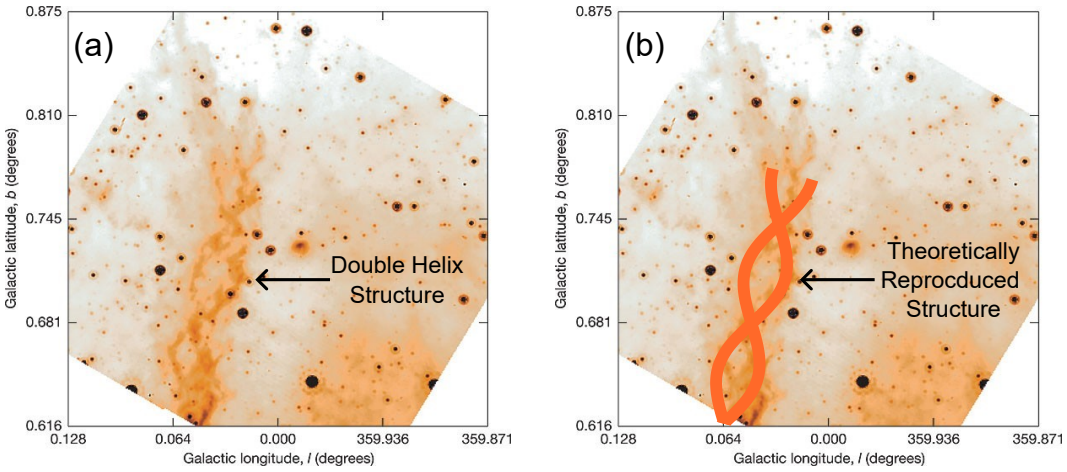

Figure 5.5: **Comparison between the double helix nebula and a double helix equilibrium reconstructed from the model** (a) The double helix nebula, observed at the infrared wavelength of 24 μm with the MIPS camera on the Spitzer Space Telescope. The spatial resolution is 6 arcsec. At the 8 kpc distance of the Galactic Centre, 1 arcmin corresponds to 2.5 pc. The minor radius is measured as $\bar{b} \approx 0.3$, and the axial angular wavenumber $\bar{k} \approx 0.6$. This image is reproduced from [73]. (b) a double helix equilibrium reconstructed from the model with $\bar{b} = 0.3$ and $\bar{k}_{eq} = 0.623$.

In some braided magnetic flux ropes experiments, an external axial magnetic field was applied, and the rotation of two flux ropes was observed [75, 76]. The helical current wires model can incorporate axial magnetic field and rotation. They provide additional radial force to the current wire, so they can be considered as extra forces in the force balance equation. In the astrophysical jets observation, rotating flow was also observed [89]. This model can also be expanded for dynamic equilibrium with helical flow through the structure.

In conclusion, this paper presents a comprehensive helical current wire model that establishes MHD equilibria. The equilibria correlate with phenomena observed in both astrophysical environments and controlled laboratory experiments. The application of this equilibrium model extends broadly to plasma studies, including but not limited to the reconstruction of magnetic flux ropes [90], magnetic flux rope interactions [91] and evolutions [92], the study of magnetic helicity [93], magnetic reconnections [94, 95], and magnetic fusion equilibrium states [96].

Chapter 6

NEUTRAL-CHARGED-PARTICLE COLLISIONS AS THE MECHANISM FOR ACCRETION DISK ANGULAR MOMENTUM TRANSPORT

1. Zhang, Y. & Bellan, P. M. Neutral-charged-particle collisions as the mechanism for accretion disk angular momentum transport. *The Astrophysical Journal* **930,** 167 (2022).

In this chapter, I move into a new area of study: the transport of angular momentum within accretion disks.

I got to the accretion disk study from Paul M. Bellan's presentation on his neutral-ion bonding accretion model [97]. His model investigated the dynamics of a metaparticle comprised of tightly bonded neutrals and ions across various charge-to-mass ratios. His findings revealed that under a critical charge-to-mass ratio, the metaparticle could possess zero canonical angular momentum, causing it to spiral inward and eventually accrete onto the central star. Intrigued by this concept, I sought to explore the dynamics further.

Coincidentally, I was also learning N-body simulation techniques for molecules through Professor José E. Andrade's ME 201 class. Recognizing the potential of applying N-body simulation to study accretion disk dynamics at the particle level, I proposed the idea to Paul M. Bellan, and he enthusiastically supported me in trying it.

Through N-body simulation, we uncovered fascinating dynamics involving ions and electrons interacting with neutrals, leading to canonical angular momentum transport between charged particles and neutrals. When the Kepler motion is of different polarity with the magnetic field, ions drift inward while electrons drift outward during collisions with neutrals. This process transports neutrals' angular momentum into charged particles' canonical angular momentum in a manner such that the net global canonical angular momentum is conserved. Building upon these findings, we devised an angular momentum transport mechanism solely reliant on neutral-charged particle collisions. Remarkably, our model predicted an accretion rate of 3×10^{-8} solar mass per year in good agreement with observed accretion

rates. Given that this angular momentum transport is contingent solely on neutrals colliding with charged particles, this mechanism should be ubiquitous.

The accumulation of ions at a smaller radius and electrons at a larger radius generates a radially outward electric field, whereas the current resulting from the separation of ions and electrons flows radially inward. Consequently, this mechanism also naturally gives rise to a gravitational dynamo, converting gravitational energy into the electric energy that powers an astrophysical jet.

6.1 Introduction

Protoplanetary discs are thin, weakly ionized, cold accretion disks existing during the early life of a star and typically have associated poloidal magnetic fields and bidirectional astrophysical jets. Protoplanetary discs have inner radii of a few a.u., outer radii of 10-100 a.u., accretion rates of 10^{-9} to 10^{-7} $M_{\odot}$ yr^{-1} [6] and poloidal magnetic fields > 1 milligauss [5]. Because accreting particles must shed angular momentum to satisfy energy constraints, accretion must involve outward transport of angular momentum [98] but how this works has been a long-standing mystery. Classical viscosity is insufficient to provide the required angular momentum tranport so efforts have been directed towards finding stronger transport mechanisms. Shakura & Sunyaev [99] proposed turbulence but did not suggest a source for the postulated turbulence. Balbus & Hawley [100] derived the Magnetorotational Instability (MRI) and proposed the MRI as the source of turbulence enhancing angular momentum transport. However, Flaherty *et al.* [101] measured actual turbulent levels in a Protoplanetary disc, and found "*there is little turbulence throughout the vertical extent of the disk, contrary to theoretical predictions based on the magnetorotational instability*." Ji *et al.* [102] constructed a laboratory device designed to demonstrate the MRI, but MRI has not been detected so far; Ji & Balbus [103] state "*To date, however, the MRI has been difficult to identify unambiguously, even though the required threshold conditions have been exceeded*."

As an alternate to turbulence and MRI, Bellan [97] argued that because the accretion disk is an axisymmetric electromagnetic-gravitational system, the fundamental conserved quantity is not the *ordinary* angular momentum (OAM) mrv_θ but rather the *canonical* angular momentum (CAM) $mrv_\theta + q\psi/2\pi$ where q is the charge, and ψ is the poloidal magnetic flux. The canonical angular momentum conservation is derived in Appendix B. We report here particle simulations of a weakly ionized,

collisional accretion disk. The simulated accretion disk is composed of "hard-disk" neutrals, ions, and electrons (because the simulation is in 2D the particles are "hard disks" rather than "hard spheres"; note that the word "disk" is being used in two different contexts – accretion disk and particle disk – which should not be confused). It is found that in the presence of collisions the total accretion disk CAM is conserved but the total OAM is not. The numerical simulation shows that collisions cause the charged particle CAM to increase with a corresponding reduction of the neutral OAM so that total CAM is conserved. In accordance with their decreased OAM, neutrals spiral inwards, i.e., accrete. The microscopic details of the OAM and CAM transfer are explained by direct calculation of the average radial velocity of a charged particle as a result of collisions with Kepler-orbiting neutrals. A radially outward electric field develops as a result of the radial inward/outward motion of the ions/electrons and this electric field is just what is required to drive the bidirectional out-of-plane electric currents flowing along bidirectional astrophysical jets. The simulations and their interpretation provide a ubiquitous, straightforward model of angular momentum shedding and jet drive mechanism [97].

6.2 Simulation Method

The simulation has a central body with mass M_* at the origin of a cylindrical coordinate system $\{r, \theta, z\}$ and a uniform magnetic field $B = B\hat{z}$ so the poloidal flux is $\psi = B\pi r^2$. Surrounding the central body are a large number of particles represented by hard disks restricted to the $z = 0$ plane. When not colliding, the equation of motion for a particle with mass m and charge q is

$$m\frac{d\mathbf{v}}{dt} = q\mathbf{v} \times \mathbf{B} - \frac{GM_*m}{r^2}\hat{r} \; . \tag{6.1}$$

Using reference parameters $r_0 = 1$ a.u., $v_{K0} = \sqrt{GM_*/r_0}$, $\omega_{K0} = \sqrt{GM_*\Big/r_0^3}$, normalized quantities $\bar{r} = r/r_0, \bar{\mathbf{v}} = \mathbf{v}/v_{K0}, \bar{t} = \omega_{K0}t, \omega_c = qB/m$, and $\bar{\omega}_c = \omega_c/\omega_{K0}$ are defined so Equation (6.1) becomes

$$\frac{d\bar{\mathbf{v}}}{dt} = \bar{\omega}_c\bar{\mathbf{v}} \times \hat{z} - \frac{1}{\bar{r}^2}\hat{r} \; . \tag{6.2}$$

The hard-disk particle model means that particles do not interact except when colliding. Particles are assumed to be disks having radius a and center at $\mathbf{r}_i$ where $i = 1$ to N and N is the number of particles. A collision occurs between particle i and particle j when $\left|\mathbf{r}_i - \mathbf{r}_j\right| < 2a$. The velocity change of particle i after a collision is

$$\delta \mathbf{v}_i = -\frac{2m_j}{m_i + m_j} \left(\mathbf{v}_{ij} \cdot \hat{n}_{ij}\right) \hat{n}_{ij} \ , \tag{6.3}$$

where $\mathbf{v}_{ij} = \mathbf{v}_i - \mathbf{v}_j$ and $\hat{n}_{ij} = \frac{\mathbf{r}_i - \mathbf{r}_j}{|\mathbf{r}_i - \mathbf{r}_j|}$.

On defining $\mathbf{u}_i$ as the mean velocity of species i, the frictional drag frequency ν_{ij} of species j on species i is defined by $d\mathbf{u}_i/dt = -\nu_{ij}(\mathbf{u}_i - \mathbf{u}_j)$; integrating this over a short time T gives

$$\Delta \mathbf{u}_i = -\nu_{ij} T (\mathbf{u}_i - \mathbf{u}_j). \tag{6.4}$$

If a particle makes S collisions in a time T then, its change in velocity will be $\Delta \mathbf{v}_i = \sum_{i=1}^{S} \delta \mathbf{v}_i(k)$. The change of the species mean velocity will be

$$\Delta \mathbf{u}_i = \left\langle \sum_{k=1}^{S} \delta \mathbf{v}_i(k) \right\rangle = -\sum_{k=1}^{S} \frac{2m_j}{m_i + m_j} \left\langle \left(\mathbf{v}_{ij} \cdot \hat{n}_{ij}\right) \hat{n}_{ij} \right\rangle \tag{6.5}$$

where the angle brackets denote averaging over particles and over directions $\hat{n}_{ij}$. By defining $\hat{p} = \hat{z} \times \hat{v}_{ij}$ where $\hat{z}$ is out of plane, then $\hat{n}_{ij} = \hat{v}_{ij} \cos\phi + \hat{p} \sin\phi$ where ϕ is a random angle that differs for each of the S collisions. Since $\left(\mathbf{v}_i - \mathbf{v}_j\right) \cdot \hat{n}_{ij} = \left|\mathbf{v}_i - \mathbf{v}_j\right| \cos\phi$, then ϕ averaging of $\left(\mathbf{v}_i - \mathbf{v}_j\right) \cdot \hat{n}_{ij} \hat{n}_{ij}$ gives $\left(\mathbf{v}_i - \mathbf{v}_j\right) \cdot \hat{n}_{ij} \hat{n}_{ij} = \left(\mathbf{v}_i - \mathbf{v}_j\right) \cos^2\phi$. Averaging over many particles gives $\left\langle \left(\mathbf{v}_i - \mathbf{v}_j\right) \cdot \hat{n}_{ij} \hat{n}_{ij} \right\rangle = \left(\mathbf{u}_i - \mathbf{u}_j\right)/2$ so combining Equations 6.4 and 6.5 gives

$$\nu_{ij} = \frac{S}{T} \frac{m_j}{m_i + m_j} \ . \tag{6.6}$$

The collisional drag frequency ν_{ij} is thus determined from the numerical simulation by counting how many collisions S are experienced by a particle in a time T and then using Equation (6.6). The ergodic assumption that the friction of a single particle over many collisions is the same as the average instantaneous friction experienced by many particles allows this determination to be made by following a single numerical particle.

A reflective boundary at an inner radius $\bar{r} = 0.1 - \bar{a}$ is used to avoid the infinite gravitational force when particles move close to the origin. This reflective boundary means that a particle is reflected back with an opposite radial velocity when it tries to penetrate inside a circle having radius $\bar{r} = 0.1$. Because this reflection is radial, it conserves both canonical and ordinary angular momentum. There is no boundary at large radius. Unless specified otherwise, $\bar{a} = 0.01$ and the number of particles is $N = 16128$. The ion mass is set to $\bar{m}_i = m_i/m_n = 1$, and the electron

mass is set to $\bar{m}_e = m_e/m_n = 0.1$. The simulation starts at $\bar{t} = 0$ with particles located in concentric circles ranging from $\bar{r} = 0.3$ to $\bar{r} = 1.9$, with a spacing $\bar{d} = 2.5\bar{a}$ between adjacent concentric circles. The particles are arranged at $\bar{t} = 0$ with uniform azimuthal spacing on each circle with inter-particle angular separation $\Delta\theta = 2\pi/\lceil 2\pi\bar{r}/\bar{d}\rceil$ where $\lceil 2\pi\bar{r}/\bar{d}\rceil$ means the nearest integer greater than or equal to $2\pi\bar{r}/\bar{d}$. Particles are assigned an initial Kepler velocity with $\bar{\mathbf{v}} = \sqrt{1/\bar{r}}\hat{\theta}$. The magnetic field direction is opposite to the Kepler rotation sense, i.e., $B < 0$. A Boris method [104] is used for pushing the particles and the time step is $\Delta\bar{t} = 10^{-4}$. The total system dimensionless CAM is

$$\bar{P}_\theta = \frac{P_\theta}{m_n r_0 v_{K0}} = \frac{\sum_{j=1}^{N}\left(m_j r_j v_{\theta j} + \frac{1}{2}q_j B r_j^2\right)}{m_n r_0 v_{K0}} = \sum_{j=1}^{N}\left(\bar{m}_j\bar{r}_j\bar{v}_{\theta j} + \frac{1}{2}\bar{\omega}_{cj}\bar{r}_j^2\right) \tag{6.7}$$

and the total system dimensionless OAM is

$$\bar{L}_\theta = \frac{L_\theta}{m_n r_0 v_{K0}} = \frac{\sum_{j=1}^{N} m_j r_j v_{\theta j}}{m_n r_0 v_{K0}} = \sum_{j=1}^{N}\bar{m}_j\bar{r}_j\bar{v}_{\theta j}. \tag{6.8}$$

6.3 Main Results

Figure 6.1 displays simulation results when there is an ion (red dot) and an electron (black dot) and a large number of neutrals (blue and grey dots). The neutrals neighboring the ion-electron pair at $\bar{t} = 0$ are shown as dark blue dots. The ion is at initial position $(\bar{r}, \theta) = (1, 0)$ with $\bar{\omega}_{ci} = -50$. The electron is at initial position $(\bar{r}, \theta) = (1.025, 0)$ with $\bar{\omega}_{ce} = +500$. By counting the number of collisions made by the electrons and ions in one Kepler period, it is found that $\bar{\nu}_{in} = 56.6$ and $\bar{\nu}_{en} = 253.1$. Figures 6.1 (a-d) show the system state at $\bar{t} = 0$, 0.34, 0.68 and 1. Figure 6.1 (e) displays the time dependence of the total system CAM $\bar{P}_\theta$ as defined by Equation (6.7) and the total system OAM $\bar{L}_\theta$ as defined by Equation (6.8). Figure 6.1 (e) thus verifies that the basic conserved quantity is not the system OAM but rather the system CAM. Figure 6.1 (f) plots the ion and electron radial positions and shows the ion moves radially inwards while the electron moves radially outwards. Figure 6.1 (g) plots the time dependence of the CAM of the ion and of the electron and shows that the ion and electron CAM are both increasing. Because total system CAM $\bar{P}_\theta$ is conserved and the ion and electron CAM are increasing, the OAM of the neutrals decreases as shown in Figure 6.1 (h). Effectively, the neutral OAM is transferred to the ion and electron CAM as the system evolves. Since OAM scales

as $r^{1/2}$, removing OAM from neutrals corresponds to the neutrals accreting towards the star. Neutral-neutral collisions will conserve neutral OAM so it is possible for some neutrals to move inwards while others move outwards in a way that conserves OAM; unlike collisions with charged particles this process will not cause global loss of neutral OAM.

We now explain why an ion and an electron have opposite average radial displacement as a result of collisions with neutrals and then relate this to angular momentum transport. The equation of motion for charged particles σ moving in a sea of neutral particles is

$$\frac{d\mathbf{u}_\sigma}{dt} \approx \omega_{c\sigma}\mathbf{u}_\sigma \times \hat{z} - \nu_{\sigma n}\left(\mathbf{u}_\sigma - \mathbf{u}_n\right) \tag{6.9}$$

where $\nu_{\sigma n}$ is given by Equation (6.6). The gravitational force on the charged particles is ignored because $|\bar{\omega}_{c\sigma}| \gg 1$. The exact solution for Equation (6.9) is

$$\mathbf{u}_\sigma = \left(\mathbf{u}_L \cos\left(\omega_{c\sigma}t\right) + \mathbf{u}_L \times \hat{z} \sin\left(\omega_{c\sigma}t\right)\right) e^{-\nu_{\sigma n}t} + \frac{1}{1+\frac{\nu_{\sigma n}^2}{\omega_{c\sigma}^2}}\left(\frac{\nu_{\sigma n}}{\omega_{c\sigma}}\mathbf{u}_n \times \hat{z} + \frac{\nu_{\sigma n}^2}{\omega_{c\sigma}^2}\mathbf{u}_n\right) . \tag{6.10}$$

On time-averaging over a cyclotron period the terms containing $\cos\left(\omega_{c\sigma}t\right)$ and $\sin\left(\omega_{c\sigma}t\right)$ vanish. On defining $\xi_\sigma = \frac{\nu_{\sigma n}}{\omega_{c\sigma}}$ the time-averaged charged particle velocity is

$$\mathbf{u}_\sigma = \frac{\xi_\sigma \mathbf{u}_n \times \hat{z} + \xi_\sigma^2 \mathbf{u}_n}{1+\xi_\sigma^2} . \tag{6.11}$$

We presume that the neutrals are in Kepler motion so $\mathbf{u}_n$ is in the θ direction. The radial component of the time-averaged charged particle velocity is thus

$$u_{\sigma r} = \frac{\xi_\sigma}{1+\xi_\sigma^2} u_{n\theta} . \tag{6.12}$$

Because ions and electrons have opposite polarity, their $\omega_{c\sigma}$ and hence their ξ_σ have opposite sign so v_{ir} and v_{er} have opposite signs. The simulation has $B < 0$ and Kepler rotation with $v_{n\theta} > 0$. Equation (6.12) gives negative radial velocity for ions and positive for electrons so ions move radially inwards and electrons move radially outwards as seen in the simulations. Because $B < 0$, the CAM magnetic component $qBr^2/2$ thus increases for both electrons and ions. Furthermore, it is seen that the radial velocity of charged particles of type σ has a maximum of $1/2$ which occurs when $|\xi_\sigma| = 1$. Because the total CAM of the two particles involved in each collision is conserved, the system total CAM is conserved. The OAM of the neutrals must decrease as a result of collisions with both electrons and ions because, on average, collisions cause an increase in the CAM of both electrons and

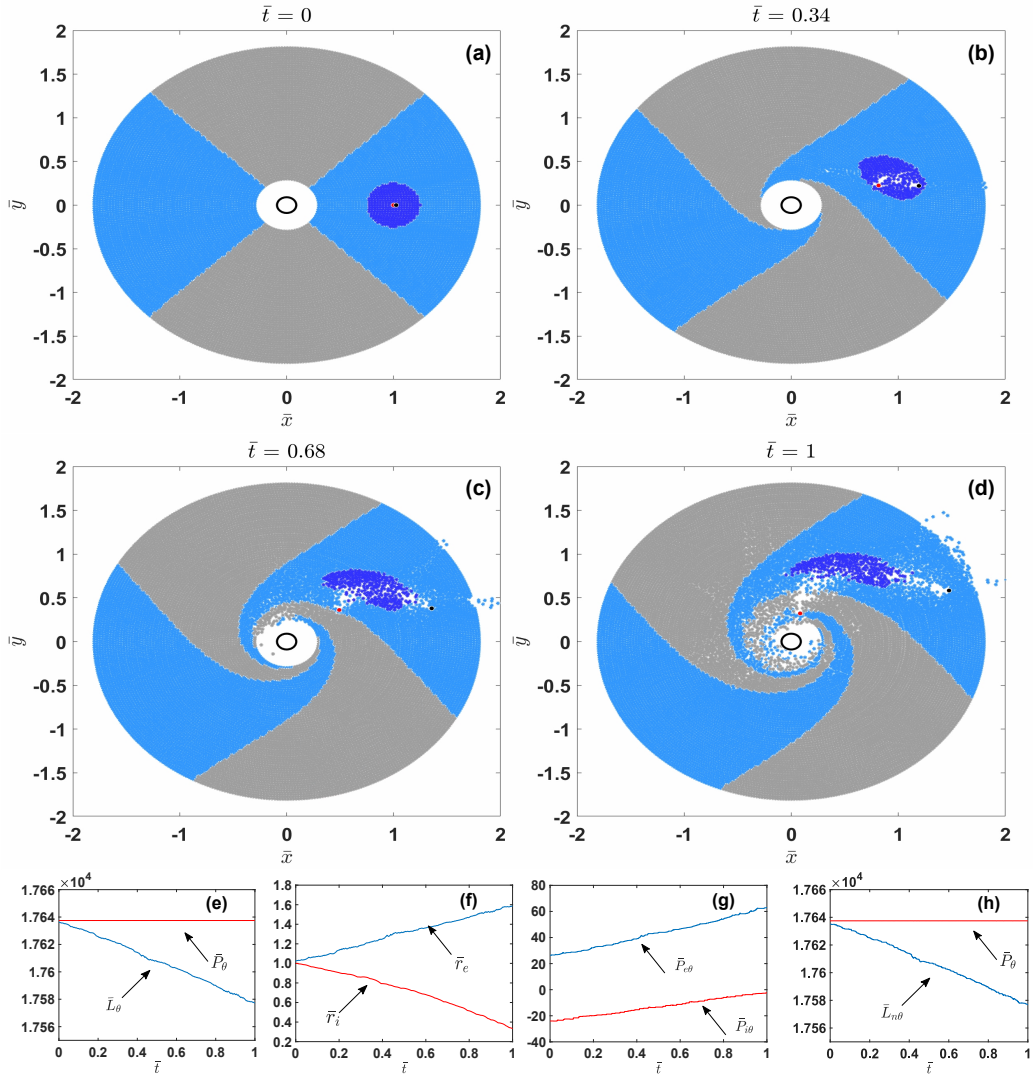

Figure 6.1: **Simulation results when there is an electron-ion pair in the system.** The ion is at initial position $(\bar{r}, \theta) = (1, 0)$ with $\bar{\omega}_{ci} = -50$ and $\bar{\nu}_{in} = 56.6$. The electron is at initial position $(\bar{r}, \theta) = (1.025, 0)$ with $\bar{\omega}_{ce} = +500$ and $\bar{\nu}_{en} = 253.1$. (a-d) The particle trajectory of the whole system at time $\bar{t} = 0$, 0.34, 0.68 and 1. Neutral particles are blue and grey. The ion is red, and the electron is black. The neutrals surrounding the electron-ion pair at $\bar{t} = 0$ are dark blue. (e) The total canonical angular momentum of the system and the total angular momentum of the system. (f) The radial positions of the ion and electron (g) The canonical angular momentum of the ion and electron. (h) The angular momentum of the neutrals and the total canonical angular momentum of the system.

ions. The mechanism is insensitive to the polarity of the magnetic field, because if $B > 0$, Equation (6.12) shows ions move radially outwards and electrons move radially inwards, so the CAM of the charged particles increases, in which case the

neutral OAM will again decrease.

Assuming a constant collision frequency and using $\bar{v}_{n\theta} = 1/\bar{r}^{1/2}$, Equation (6.12) can be integrated to give

$$\bar{r}_\sigma(\bar{t}) = \left(\frac{3}{2}\frac{\xi_\sigma}{1+\xi_\sigma^2}\bar{t} + \bar{r}_\sigma^{\frac{3}{2}}(\bar{t}=0)\right)^{\frac{2}{3}}. \tag{6.13}$$

Figures 6.2 (a-c) compare the time dependence of the radial position of an ion from a simulation with the dependence predicted by Equation (6.13); the ion initial position is $(\bar{r}, \theta) = (1, 0)$. Figure 6.2 (d) presents the ξ_i dependence of the average radial velocity $|\bar{v}_{ir}| = |\bar{r}_i(\bar{t}=1) - \bar{r}_i(\bar{t}=0)|$. The simulation motion and radial velocity agree well with Equation (6.13) and also confirm that the ion radial velocity has maximum value when $|\xi| = 1$. The discrepancy of some simulated points in Figure 6.2 (d) is presumed to be from the friction collision force approximation and radial velocity of colliding neutrals. The friction collision force is derived from averaging over the finite number of collisions so if the number of collisions is not large, there will be significant variation in how the velocity of the charged particle decreases. An additional effect is that at $\bar{t} = 0$ neutrals have no radial velocity component but then some neutrals develop a radial velocity upon colliding with charged particles, and in subsequent collisions this neutral radial velocity can accelerate or decelerate the radial motion of charged particles. Figure 6.2 (c) presents a simulation with a small $|\xi_i|$. The oscillations from cyclotron motion are visible in the radial motion because the collision frequency is much smaller than the cyclotron frequency. Even in this regime, the ion continues to move radially inwards and Equation (6.12) still holds. In this low collisionality limit, the average radial velocity can be evaluated by averaging the jumps in guiding center $\Delta\mathbf{r}_{gc} = -\frac{1}{\omega_c}\hat{z}\times\Delta\mathbf{v}$ as a result of collisions; this corresponds to Equation (6.12) in the small $|\xi_\sigma|$ limit and yields an average guiding center radial velocity $v_{\sigma r} = \xi_\sigma v_{n\theta}$.

The radial velocity of neutrals is now derived from the conservation of total system CAM. Consider a collisional system where at a specific radius neutrals have density n_n and average azmuthal velocity $u_{n\theta}$, ions have density n_i and average azmuthal velocity $u_{i\theta}$ and electrons have density n_e and average azmuthal velocity $u_{e\theta}$. The CAM density at this radius is thus

$$\mathcal{P}_\theta = n_n m_n r_n u_{n\theta} + n_i m_i r_i u_{i\theta} + n_e m_e r_e u_{e\theta} + \frac{1}{2}n_i q_i B r_i^2 + \frac{1}{2}n_e q_e B r_e^2 = \text{const.} \tag{6.14}$$

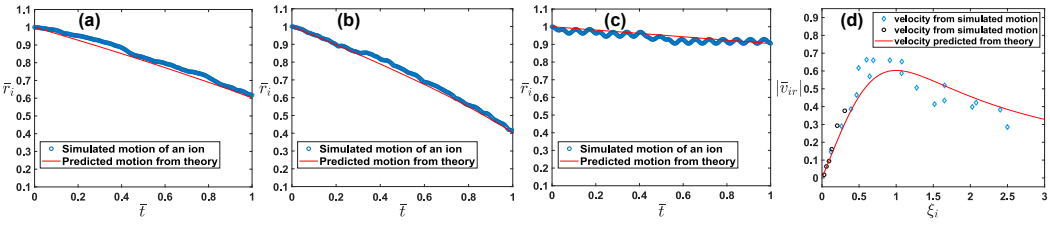

Figure 6.2: **Verification of the derived radial velocity.** (a-c) Comparison between the simulated motion of one ion in the system (blue circles) and the predicted motion from Equation (6.13) (red lines). In (a) to (c), respectively, $\bar{\omega}_{ci} = -12$, -50, -100, $\bar{v}_{in} = 28.8$, 53.6, 9.4 which give $\xi = -2.40$, -1.07, -0.09. (d) Comparison between the simulated velocity of one ion in the system (blue diamonds and black circles) and the predicted velocity from Equation (6.12) (red lines) with $|\bar{v}_{ir}| = |\bar{r}_i\,(\bar{t}=1) - \bar{r}_i\,(\bar{t}=0)|$. For (c) and the black circles in (d) the simulation has $\bar{a} = 0.025$ and $\bar{d} = 4\bar{a}$ with N=1183 particles arranged on concentric circles from $\bar{r} = 0.3$ to $\bar{r} = 1.9$.

During a small time Δt, the change of the CAM density is

$$\Delta\mathcal{P}_\theta = n_n m_n\,(\Delta r_n u_{n\theta} + r_n \Delta u_{n\theta}) + n_i m_i\,(\Delta r_i u_{i\theta} + r_i \Delta u_{i\theta}) + n_e m_e\,(\Delta r_e u_{e\theta} + r_e \Delta u_{e\theta}) + n_i q_i B r_i \Delta r_i + n_e q_e B r_e \Delta r_e = 0. \tag{6.15}$$

The system temporal evolution can be decomposed into two types of interspersed intervals, namely time intervals where there are collisions and time intervals where there are no collisions. Only the time intervals when there are collisions could contribute to angular momentum transport between charged particles and neutrals. Because the two particles involved in a collision have the same r at the time of their collision and because there is no change in the total momentum of these two particles as a result of the collision, $n_n m_n r_n \Delta u_{n\theta} + n_i m_i r_i \Delta u_{i\theta} + n_e m_e r_e \Delta u_{e\theta} = 0$. Ignoring $n_i m_i \Delta r_i u_{i\theta} + n_e m_e \Delta r_e u_{e\theta}$ because it is much smaller than the magnetic parts of the CAM, Equation (6.15) reduces to

$$n_n m_n \Delta r_n u_{n\theta} + n_i q_i B r_i \Delta r_i + n_e q_e B r_e \Delta r_e = 0. \tag{6.16}$$

Assuming $u_{n\theta} = v_K = \sqrt{GM/r_n}$ and dividing by Δt, the radial velocity of neutrals is obtained as

$$u_{nr} = -\frac{\omega_{ci}}{\omega_K}\frac{m_i}{m_n}\,(\chi_i u_{ir} - \chi_e u_{ir}) \tag{6.17}$$

where $\chi_i = \frac{n_i}{n_n}$ and $\chi_e = \frac{n_e}{n_n}$ are the ion and electron density fraction. Assuming $\chi_i = \chi_e = \chi$, then

$$u_{nr} = -\chi\frac{\omega_{ci}}{\omega_K}\frac{m_i}{m_n}\,(u_{ir} - u_{ir}) \tag{6.18}$$

Using Equation (6.12) this becomes

$$u_{nr} = -\chi\omega_{ci}\frac{m_i}{m_n}\left(\frac{\xi_i}{1+\xi_i^2} - \frac{\xi_e}{1+\xi_e^2}\right)r_n. \tag{6.19}$$

Although we assume a uniform magnetic field for the sake of simplicity, the radial velocity expression still holds for a non-uniform magnetic field situation.

Figure 3 (a-b) presents the radial motion of 43462 neutrals, 440 ions and 440 electrons initially uniformly distributed between $\bar{r} = 0.95$ and $\bar{r} = 2$ while Figure 3 (c-d) shows for comparison a reference situation having neutrals only (no charged particles). These simulations have an initial velocity which is Kepler plus a small random velocity (essential for collisions to occur in the neutral-only reference case since without random velocities, neutrals in circular Kepler orbits would never collide with each other). Figure 3 (e-f) compares the u_{nr} dependence on r from the simulation with the prediction calculated from u_{ir} using a modified form of Equation (6.17) with $u_{nr} = -\frac{\omega_{ci}}{\omega_K}\frac{m_i}{m_n}(\chi_i u_{ir} - \chi_e u_{ir})$, where $\chi_i = \frac{n_i}{n_n}$ and $\chi_e = \frac{n_e}{n_n}$ becasue the ions and electrons moves to different radius and the fraction of ions does not equal to the fraction of electrons for some regions. The electric field from this charge separation is ignored in the simulation. The slight jaggedness of the prediction (circles) is because of the limited number of charged particles in each radius bin. The u_{nr} from the simulation has excellent agreement with the Equation (6.17) prediction in Figure 3 (f) between $\bar{r} = 1$ and $\bar{r} = 1.8$ where the ionization fraction is relatively stable. In contrast, Figure 3(h) shows that when there are no ions u_{nr} is zero in the central region and there is only a small diffusive flux at the edges associated with the density gradient. Comparison between Figures 3 (f) and (h) of u_{nr} in the interior region $1 < r < 1.8$, (i.e., no edge diffusion) clearly shows that there is a substantial radial inward neutral flow only when ions are present. For the system with ions, the total system CAM is conserved with $\bar{P}_\theta = 5.4 \times 10^4$ while the total system OAM decreases from $\bar{L}_\theta\,(\bar{t} = 0) = 5.4 \times 10^4$ to $\bar{L}_\theta\,(\bar{t} = 0.8) = 3.7 \times 10^4$. For the neutrals-only system, the total system OAM is conserved with $\bar{L}_\theta\,(\bar{t} = 0) = \bar{L}_\theta\,(\bar{t} = 0.8) = 5.4 \times 10^4$.

The simulation conserves the total energy W = sum of kinetic and potential energies. For a single particle in a pure circular Kepler orbit the total energy in dimensioned parameters is $W = L^2/(2mr^2) - mM_*G/r = -mM_*G/(2r)$ so total energy would not be conserved if a particle moved from a pure circular Kepler orbit at one radius to a pure circular Kepler orbit at a different radius. Thus, particles cannot change radius while simultaneously conserving energy and maintaining a pure circular

Kepler orbit. In a real disk, the energy released from decrease of particle radial position would be extracted as blackbody radiation and electrical power expended in driving the astrophysical jets. This energy release from the disk would enable particles to maintain nearly circular Kepler orbits as their radial position decreased. If it is assumed that particles maintain a pure circular Kepler orbit as their radius decreases, Equation (17) becomes modified to give a u_{nr} that is double that of Equation (17); this comes from assuming that $n_n m_n \Delta\left(r_n u_{n\theta}\right) = \frac{1}{2} n_n m_n u_{n\theta} \Delta r_n$ since for a pure circular Kepler orbit $u_{n\theta} \sim r^{-1/2}$ and $n_n m_n r_n \Delta u_{n\theta} = -\frac{1}{2} n_n m_n u_{n\theta} \Delta r_n$.

The mass accretion rate is $\dot{M} = -2\pi r v_{nr} \Sigma$ where $\Sigma \approx n m_n h$ is the surface density and h is the scale height. Using the radial velocity of neutrals given by Equation (6.18), the accretion rate is thus

$$\dot{M} = 2\pi\chi n r^2 h \left|qB\right| \left(\frac{\left|\xi_i\right|}{1+\xi_i^2} + \frac{\left|\xi_e\right|}{1+\xi_e^2} \right). \tag{6.20}$$

The friction collision frequency between charged particles and neutrals taking into account dipole moment effects of neutrals is $\nu_{\sigma n} = \frac{m_n}{m_n + m_\sigma} n_n \langle \sigma v \rangle_{\sigma n}$ where typical values of the rate coefficients are $\langle \sigma v \rangle_{in} = 1.9 \times 10^{-9}$ cm$^3 \cdot$ s^{-1} and $\langle \sigma v \rangle_{en} = 1.0 \times 10^{-15}$ cm$^2 \left(\frac{128 k T_e}{9\pi m_e} \right)^{\frac{1}{2}}$ [105]. At $r = 1$ a.u., we presume $n_n = 10^{20}$ m^{-3} [106], $B = 5$ mG [5], $\chi = 10^{-12}$ [107, 108], $T_e = 100$ K, $h = 0.1$ a.u., $m_i = m_H = 1.66 \times 10^{-27}$ kg, $m_n = m_{H_2} = 3.32 \times 10^{-27}$ kg. Then $\left|\xi_i\right| = 2627$ and $\left|\xi_e\right| = 9.44$. Since $\left|\xi_i\right| \gg \left|\xi_e\right| \gg 1$ Equation (6.19) gives the mass accretion rate as $\dot{M} = 2\pi\chi n r^2 h \left|qB/\xi_e\right| = 2.9 \times 10^{-8}\ M_\odot \cdot \text{year}^{-1}$. This agrees well with observations that the mass accretion rate is 10^{-9} to $10^{-7}\ M_\odot \cdot \text{year}^{-1}$.

The accumulation of ions at small radius and accumulation of electrons at large radius establishes a radial electric field $E_r > 0$. The radial inward motion of the ions and outward motion of the electrons corresponds to a radial electric current $J_r < 0$. Because $E_r J_r < 0$ the process acts as an electric generator and so is a dynamo that converts gravitational potential energy into electrical energy. The radial electric field provides an electric force that opposes the radial inward motion of the ions and outward motion of the electrons. The maximum radial electric field on the disk plane $E_{r\,\max} = -B v_{n\theta} = -B\sqrt{\frac{GM_*}{r}}$ is achieved when the charge accumulation stops; this maximum will occur if there is no means to drain the charge accumulation and at this maximum radial electric field the time-average radial velocity of charged particles goes to zero so the electric current would cease. However, if a mechanism such as an astrophysical jet circuit exists to drain the charge accumulation, the radial electric

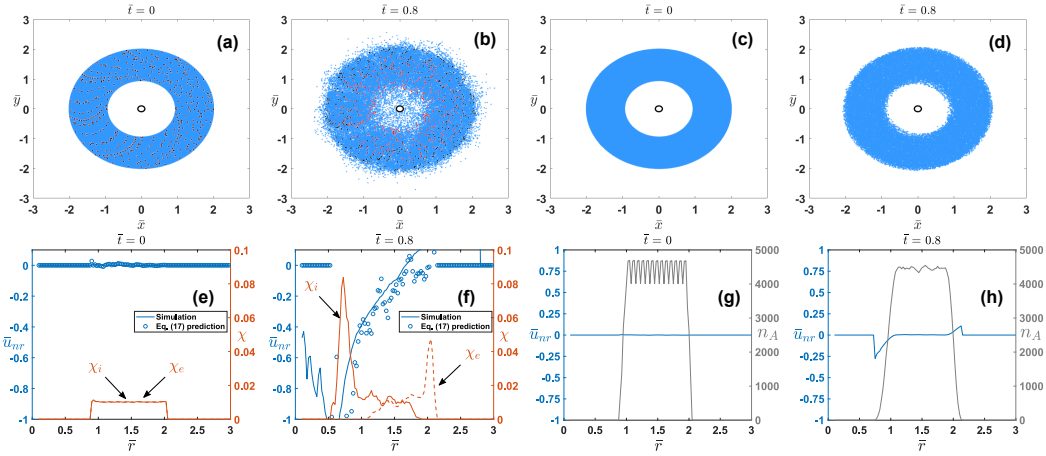

Figure 6.3: **Simulation results when there are a lot of ions and electrons in the system.** (a, b) The particle trajectory of a system with ions at times $\bar{t} = 0$ and 0.8. The simulation has $\bar{a} = 3 \times 10^{-3}$, $\bar{d} = 5a$ and $\bar{\omega}_{ci} = -50$ with $N_n = 43462$ neutrals and $N_i = 440$ ions and $N_e = 440$ electrons located in concentric circles ranging from $\bar{r} = 0.95$ to $\bar{r} = 2$. The initial velocity is a Kepler velocity plus a random thermal velocity having 10% of the Kepler velocity magnitude, that is $\bar{\mathbf{v}}(\bar{t} = 0) = \sqrt{1/\bar{r}}\hat{\theta} + 0.1\sqrt{1/\bar{r}}\hat{v}_{random}$ where $\hat{v}_{random}$ is a random direction vector. (c, d) The particle trajectory of a reference system having neutrals only at times $\bar{t} = 0$ and 0.8 with the same initial condition for neutrals as in (a). (e, f) The neutral radial drift velocity profile and ionization fraction of the system in (a, b). The blue line is the radial drift velocity profile of neutrals obtained from the simulation. The average radial velocity at a certain radius $\bar{r}$ is obtained as the average velocity of particles that are in a bin between radial position $\bar{r} - \Delta\bar{r}$ and $\bar{r} + \Delta\bar{r}$ with $\Delta\bar{r} = 0.05$. The blue circles are the radial velocity of neutrals calculated as a function of the ion radial velocity and electron radial velocity as predicted by a modified expression of Equation (6.17) with $u_{nr} = -\frac{\omega_{ci}}{\omega_K}\frac{m_i}{m_n}(\chi_i u_{ir} - \chi_e u_{ir})$, where $\chi_i = \frac{n_i}{n_n}$ and $\chi_e = \frac{n_e}{n_n}$. The red solid/dashed line shows the ion/electron fraction versus radial position. (g, h) The neutral drift velocity profile and neutral surface density n_A versus radial position of the system of (c, d). The rippling of n_A in (g) is from the aliasing of the radial position bin period and the concentric circle position period and this rippling smooths out as the random velocity and collisions destroy the imposed initial pattern of concentric circles of neutrals.

field in the $z = 0$ plane will drive an out-of-plane electric current and this electric field will be less than $E_{r\,\max}$. The bidirectional jet electric currents are directed away from the accretion disk in the small radius region (ion accumulation region). The slight r component of the out-of-plane electric current and its associated azimuthal magnetic field B_ϕ produce $J_r B_\phi$ forces that drive bidirectional astrophysical jets flowing away from the disk plane; this adds to axial pressure gradients that also drive a flow away from the disk plane [97, 109].

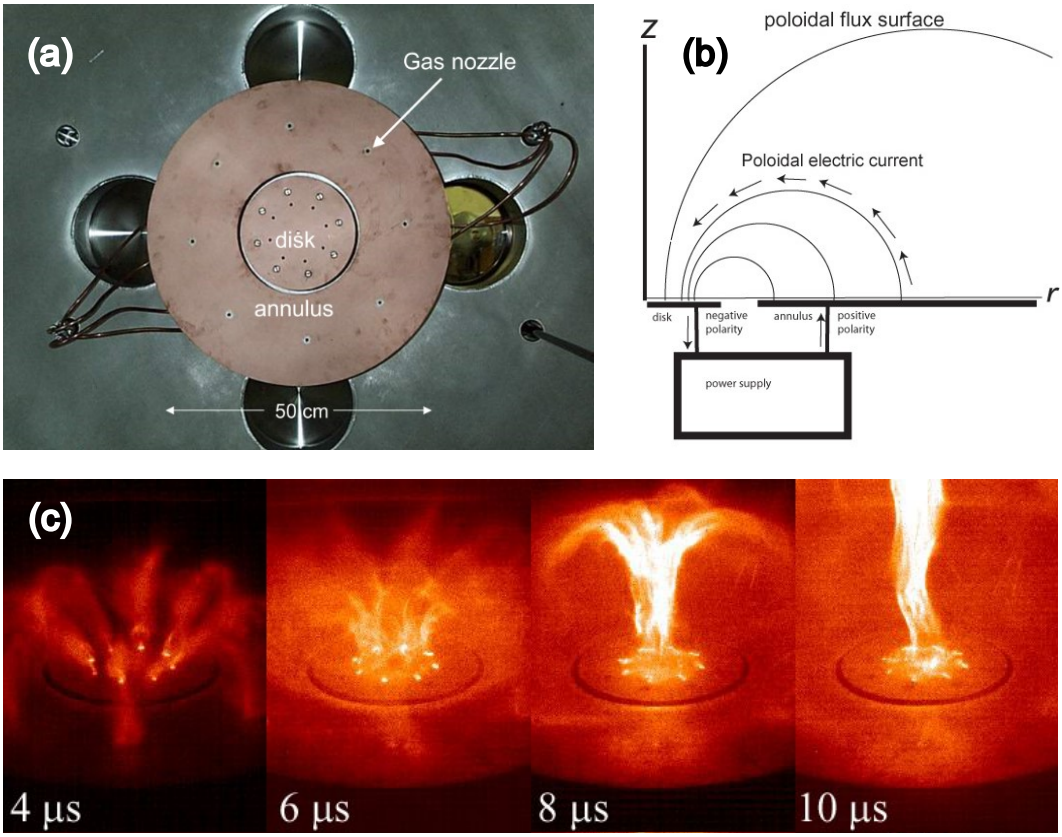

Figure 6.4: **Caltech astrophysical jet experiment**. (a) The experiment electrode structure. there is a conducting disc and a coplanar annulus surrounding the disc and separated by a small gap. (b) The power supply. Poloidal current is produced by a power supply imposing a radial electric field between a conducting disc and a coplanar conducting annulus. (c) Typical jets generated from the experiment. Eight collimated "spider legs" merge on axis to form a central column jet that collimates and propagates into the vacuum vessel.

The configuration for generating jets bears topological resemblance to the Caltech astrophysical jet experiment [110–112] as shown in Figure 6.4. In this setup, a poloidal current is induced by a power supply that applies a radial electric field between a conducting disc positioned in the $z = 0$ plane and a coplanar conducting annulus encircling the disc, with a small gap between them. Figure 6.4 (a) illustrates the electrode structure comprising a conducting disc and an adjacent coplanar annulus, separated by a narrow gap, housed within a vacuum chamber. The circuit diagram in Figure 6.4 (b) presents the connection of the power supply to the disc and the annulus. The power supply ionizes the gas puffed and generates a poloidal electric current. Figure 6.4 (c) shows a typical experimental jet formation sequence, starting from the formation of "spider legs" due to the poloidal current, progressing

to collimation, and forming a jet. Notably, the accumulation of ions at smaller radii and electrons at larger radii mirrors the setup of the astrophysical jet experiment, enabling the generation of a poloidal current and the propulsion of a jet from the disc.

6.4 Conclusions

(i) The fundamental conserved quantity is the canonical angular momentum $mrv_\theta + q\psi/2\pi$, not the ordinary angular momentum mrv_θ. Ordinary angular momentum and canonical angular momentum are identical for a neutral but are very different for charged particles.

(ii) Collisions transfer neutral ordinary angular momentum to charged particle canonical angular momentum so neutrals spiral inward.

(iii) The accumulation of ions at small radius and electrons at large radius creates a radial electric field. Since $E_r J_r < 0$, the disk acts as a gravity-powered dynamo.

(iv) The accumulation of ions at small radius drives an axially outward out-of-plane poloidal electric current along the poloidal magnetic field at small radius. This current and its associated magnetic field produce forces that drive bidirectional astrophysical jets flowing away from the disk. The increasing energy in the jets as they lengthen is powered by the gravitational disk dynamo.

Chapter 7

MECHANISM FOR GENERATION OF ANGULAR MOMENTUM IN AN ASTROPHYSICAL SYSTEM

1. Zhang, Y. & Bellan, P. M. Mechanism for generation of angular momentum in an astrophysical system. (to be submitted) (2024).

Why astrophysical entities rotate and so have angular momentum has long been a mystery. In this chapter, we utilized N-body simulations to investigate a weakly ionized plasma system featuring radially free-fall neutrals, aiming to unravel the mechanisms behind their rotation. Upon colliding with the free-falling neutrals, ions and electrons exhibit disparate mean velocities. This velocity difference causes ions and electrons to decrease their canonical angular momentum $P_\theta = mrv_\theta + q\psi/2\pi$ while at the same time the neutrals gain ordinary angular momentum $L = mrv_\theta$. The net result is that the total system canonical angular momentum is conserved as predicted by Langrangian mechanics for an axisymmetric system. These findings demonstrate that a weakly-ionized, initially non-rotating cloud of neutral particles will spontaneously acquire rotation during infall. Furthermore, quantitative scaling analyses forecast an angular momentum generation rate capable of converting neutral infall motion into neutral Keplerian rotation in the outer regions of a protoplanetary accretion disk.

7.1 Introduction

Rotation is common in astrophysics: protoplanetary disks, molecular clouds, and galaxies rotate about a star or proto-stellar core while planets rotate both about their axis and about a star. This indicates that angular momentum generation is ubiquitous yet why this is so is an unanswered question. A specific example of this question is what causes the transition from free-fall motion to Keplerian rotation in a protoplanetary disk. Measurements of the protoplanetary disk rotation velocity profile show that in the inner region particles are in Kepler rotation, but in the outer region particles are radially infalling [3, 113, 114]. How particle motion changes from infalling radial motion to azimuthal Kepler motion has not been explained.

Magnetic fields are common in astrophysical systems and have milligauss magnitudes in protoplanetary disks [5] and microgauss magnitudes in molecular clouds

[115]. Lagrangian mechanics shows that when charged particles are in azimuthally symmetric fields, the conserved quantity is not the ordinary angular momentum (OAM) $L = mrv_\theta$, but rather the canonical angular momentum (CAM) $P_\theta = mrv_\theta + q\psi/2\pi$ where q is the charge and ψ is the poloidal magnetic flux [116]. The CAM magnetic term $q\psi/2\pi$ is typically orders of magnitude larger than the OAM term mrv_θ for Kepler motion so, even in very weakly ionized systems where the fraction of charged particles is extremely small, the charged particles contain substantial CAM. Because ψ depends on position, the total canonical angular momentum of the charged particles will change if ions and electrons radially separate. However, if the global system is axisymmetric, then the total system CAM is conserved so any change in total charged particle CAM must be compensated by an equal and opposite change in the OAM of the much larger number of neutral particles. Thus, any mechanism that causes a radial separation of ions from electrons provides a means for either generation or shedding of neutral particle OAM.

MHD is often used to model accretion disk dynamics but MHD is a fluid model based on the assumption that ions and electrons have nearly the same velocities perpendicular to the magnetic field. This is a simplifying assumption asserted in the derivation of the MHD Ohm's law which is not necessarily correct. Deviation from this assumption, known as the Hall term, can significantly affect accretion disk formation dynamics [117, 118]; it has been shown that the Hall term can spin up an accretion disk [117].

Bellan [119] proposed a complete electric circuit for an accretion disk acting as an electrical power supply driving an astrophysical jet and showed that the dynamics could be interpreted in terms of CAM conservation. The z direction is defined by the disk rotation sense and a cylindrical coordinate system (r, θ, z) is used. There are poloidal magnetic fields (B_r, B_z) and toroidal magnetic fields (B_θ) as well as poloidal electric currents (J_r, J_z) and toroidal electric currents (J_θ). The accretion disk acts as a gravitationally-powered dynamo (effective battery) driving the jet poloidal current. Symmetry arguments show that in the disk the magnetic field is axial and the current is radial. The inner accretion disk has B_z negative while the outer disk radius has B_z positive. However, J_r is negative throughout the disk givng a resulting torque $-rJ_rB_z$ which creates angular momentum at large radius but removes (sheds) angular momentum at small radius.

In a previous paper [116] we demonstrated an angular momentum shedding mechanism based on Kepler-orbiting neutral particles in the accretion disk inner region

colliding both with each other and with charged particles. This first principles calculation of particle dynamics avoids imposing fluid assumptions inherent in MHD and so captures basic physics phenomena missing from MHD. The collisions were observed to cause a radial separation of the charged particles and this involved a conversion of the neutral particle OAM into charged particle CAM in a manner such that total system CAM was conserved. Quantitative scaling predicted a mass accretion rate consistent with observations.

Here we consider the opposite situation, namely generation of neutral OAM in the outer disk region, i.e., spinning up. We assume that neutrals are initially not spinning but instead are radially falling inwards in the gravity of a star. Using a 2D N-body simulation of a weakly ionized accretion disk, we show that an initially zero angular momentum system develops angular momentum as a result of collisions between neutrals and charged particles. The key principle is that because of the large ion to electron mass ratio and the similarity between neutral and ion mass, neutrals entrain ions but not electrons. The electrons are instead nearly frozen into the magnetic field. Collisions between infalling neutrals and ions cause the ions to have nearly the same inward radial motion as the infalling neutrals whereas electrons are left behind. The radially inward moving ions experience a magnetic force which gives the ions an azimuthal velocity. However, since the ions are collisionally bound to the neutrals, this ion azimuthal velocity causes the neutrals to develop an azimuthal velocity also. At the particle level, collisions convert a change in charged particle CAM into a change in neutral OAM. These changes are manifested by the neutrals spinning up (OAM increase) and the ions and electrons radially separating (CAM decrease). This process can equivalently be explained using fluid theory by stating that a magnetic torque $-rJ_rB_z$ spins up the system. Quantitative scaling shows that this mechanism efficiently converts free fall motion into Kepler rotation in the protoplanetary accretion disk outer region. Similar processes may cause angular momentum generation in molecular clouds and galaxies.

7.2 Simulation Method

The simulation has a central body with mass M_* at the origin of a cylindrical coordinate system $\{r, \theta, z\}$ and a uniform magnetic field $\mathbf{B} = B\hat{z}$ with $B > 0$ so $\psi = B\pi r^2$ is positive. Surrounding the central body are a large number of particles represented by hard disks restricted to the $z = 0$ plane. When not colliding, the equation of motion for a particle with mass m_σ and charge q_σ is

$$m_\sigma \frac{d\mathbf{v}}{dt} = q_\sigma \mathbf{v} \times \mathbf{B} - \frac{GM_* m_\sigma}{r^2}\hat{r} \ . \tag{7.1}$$

In contrast to our previous paper [116] where a reference radius of 1 a.u. was used to denote examination of the inner region of a protoplanetary disk, here we use a reference radius $r_0 = 100$ a.u. to denote examination of the outer region of a protoplanetary disk. As before, the Kepler velocity is $v_{K0} = \sqrt{GM_*/r_0}$ and the Kepler frequency is $\omega_{K0} = \sqrt{GM_*/r_0^3}$. Normalized quantities are defined as $\bar{r} = r/r_0$, $\bar{\mathbf{v}} = \mathbf{v}/v_{K0}$, $\bar{t} = \omega_{K0}t$, and $\bar{\omega}_{c\sigma} = \omega_{c\sigma}/\omega_{K0}$ where $\omega_{c\sigma} = q_\sigma B/m_\sigma$. With these definitions Equation (7.1) becomes

$$\frac{d\bar{\mathbf{v}}}{dt} = \bar{\omega}_{c\sigma}\bar{\mathbf{v}} \times \hat{z} - \frac{1}{\bar{r}^2}\hat{r} \ . \tag{7.2}$$

Assuming the magnetic field is 1 μG at 100 a.u. and using $q_i = 1.6 \times 10^{-19}$C, and $m_i = m_H = 1.66 \times 10^{-27}$kg the ion cyclotron frequency is $\omega_{ci} = 9.6 \times 10^{-3}\text{s}^{-1}$ whereas the Kepler frequency is $2.0 \times 10^{-10}\text{s}^{-1}$ for $M_* = M_\odot$. Thus, $\bar{\omega}_{ci} > 10^7$ while for electrons the magnitude of $\bar{\omega}_{ce}$ will be even larger. The Kepler frequency decays as $\sim r^{-\frac{3}{2}}$ and assuming B decays as $\sim r^{-3}$ it is seen that $\omega_{ci}/\omega_K = 4.8 \times 10^7 (r/100\text{a.u.})^{-\frac{3}{2}}$. The ion cyclotron frequency thus would only equal the Kepler frequency at $r = 1.3 \times 10^7$a.u. which would be much larger than the typical 2.5×10^5a.u. interstellar distance.

The hard-disk particle model means that particles do not interact except when colliding [116]. The particle radius is $\bar{a} = 0.001$. Unless specified otherwise the number of particles is $N = 95,240$. Masses are normalized to the neutral particle mass. The ion mass is set to be the same as the neutral particle mass so $\bar{m}_i = m_i/m_n = 1$. The normalized electron mass is set to $\bar{m}_e = m_e/m_n = 0.01$. The simulation starts at $\bar{t} = 0$ with particles located in concentric circles ranging from $\bar{r} = 1$ to $\bar{r} = 2$ (i.e., 100 to 200 a.u. in un-normalized distance). Particles are assumed to be initially in free fall and so have an initial velocity $\bar{\mathbf{v}} = -\sqrt{2/\bar{r}}\hat{r}$. A Boris method [104] with a time step $\Delta\bar{t} = 10^{-4}$ is used for pushing the particles.

In this simulation, our emphasis lies in demonstrating fundamental concepts and particle-level physics. Therefore, we simplify the magnetic field by setting it as a constant. This approach aids in easier analysis and interpretation of results. In real situations, the magnetic field should evolve with plasma motion.

The total system dimensionless CAM is

$$\bar{P}_\theta = \frac{P_\theta}{m_n r_0 v_{K0}} = \frac{\sum_{j=1}^{N}\left(m_j r_j v_{\theta j} + \frac{1}{2} q_j B r_j^2\right)}{m_n r_0 v_{K0}} = \sum_{j=1}^{N}\left(\bar{m}_j \bar{r}_j \bar{v}_{\theta j} + \frac{1}{2}\bar{\omega}_{cj}\bar{r}_j^2\right) \tag{7.3}$$

and the total system dimensionless OAM is

$$\bar{L}_\theta = \frac{L_\theta}{m_n r_0 v_{K0}} = \frac{\sum_{j=1}^{N} m_j r_j v_{\theta j}}{m_n r_0 v_{K0}} = \sum_{j=1}^{N} \bar{m}_j \bar{r}_j \bar{v}_{\theta j}. \tag{7.4}$$

7.3 Main Results

Figure 7.1 displays simulation results when there is one ion (red dot), one electron (black dot) and 95,238 neutrals (blue dots). The ion is initially at $(\bar{r}, \theta) = (1.2, 0)$, $\bar{\omega}_{ci} = +30$, and $\bar{\nu}_{in} = 45$ where $\bar{\nu}_{in}$ is the effective collision frequency between the ion and neutrals. The electron is at initial position $(\bar{r}, \theta) = (1.2, 0.01)$ with $\bar{\omega}_{ce} = -3000$ and $\bar{\nu}_{en} = 238$. The effective collision frequency $\nu_{\sigma n}$ is determined [116] from the numerical simulation by counting how many collisions S are experienced by an ion or an electron in a time T and then using $\nu_{\sigma n} = \frac{S}{T}\frac{m_n}{m_n + m_\sigma}$. Figures 7.1 (a-c) show the system at $\bar{t} = 0$, 0.2, and 0.4 and indicate that neutrals move radially inward as manifested by the shrinking inner and outer radii of the blue annulus. Figure 7.1 (d) displays the time dependence of the respective radial positions of the ion and of the electron. The ion, entrained by the infalling neutrals, moves radially inwards while the electron, approximately frozen to the magnetic field, is left behind at nearly its initial radial position. Figure 7.1 (e) displays the time dependence of the total system CAM $\bar{P}_\theta$ as defined by Equation (7.3), the CAM of the ion and electron $\bar{P}_{i\theta} + \bar{P}_{e\theta}$, and the OAM of the neutrals $\bar{P}_{n\theta}$. The total system CAM remains constant, verifying that the entire system conserved quantity is the system total CAM. The CAM of the ion and electron decreases, and thus the OAM of the neutrals increases, as shown in Figure 7.1 (e). Charged particle CAM is effectively transferred to neutral particle OAM as the system evolves.

We now explain why an ion and an electron develop different radial drift velocities upon colliding with neutrals and then relate this to angular momentum transport. Dimensioned variables will be used for this explanation.

The equation of motion for an ensemble of charged particles σ moving in a sea of neutral particles is

$$\frac{d\mathbf{u}_\sigma}{dt} \approx \omega_{c\sigma}\mathbf{u}_\sigma \times \hat{z} - \nu_{\sigma n}\left(\mathbf{u}_\sigma - \mathbf{u}_n\right) \tag{7.5}$$

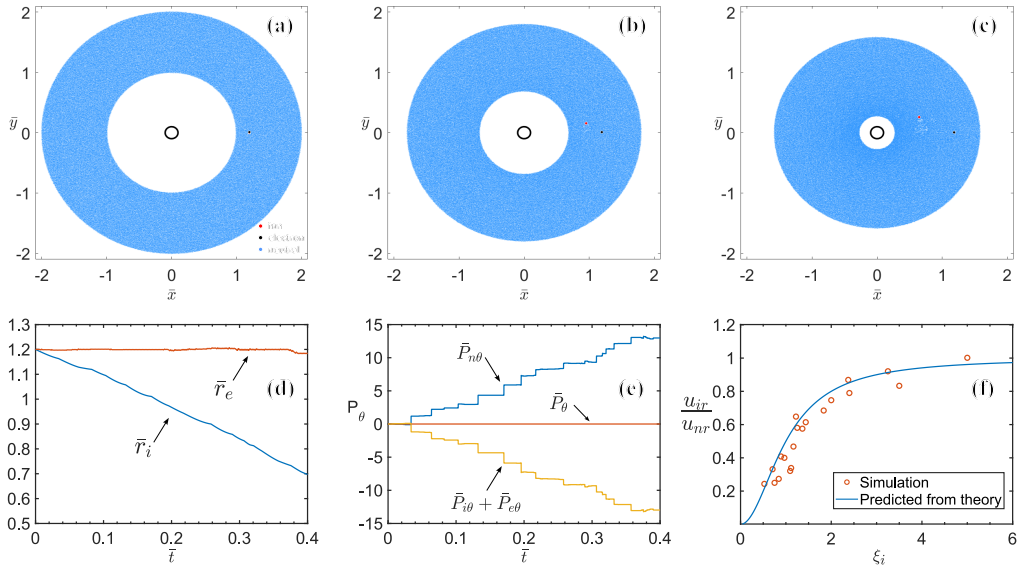

Figure 7.1: **Simulation results when there is an electron-ion pair in the system.** The ion and electron are initially at $\bar{r} = 1.2$ and are separated by a small azimuthal angle; $\bar{\omega}_{ci} = +30$, $\bar{\nu}_{in} = 45$, $\bar{\omega}_{ce} = -3000$ and $\bar{\nu}_{en} = 238$. (a-c) The system at $\bar{t} = 0$, 0.2, and 0.4. Neutral particles are blue, the ion is red, and the electron is black. (d) The radial positions of the ion and electron. (e) The total system CAM $\bar{P}_\theta$, and the total neutral OAM $\bar{P}_{n\theta}$, and the total CAM of the electron-ion pair $\bar{P}_{i\theta} + \bar{P}_{e\theta}$. (f) Comparison between the simulated velocity ratio u_{ir}/u_{nr} of the ion and the predicted velocity from Equation (7.8) (blue lines). This is obtained from different simulations by varying ω_{ci} and ν_{in}.

where $\nu_{\sigma n}$ is the effective frictional drag collision frequency between the charged particle ensemble and the neutrals and $\mathbf{u}_n$ is the mean velocity of the neutrals. This effective frictional drag has meaning for an ensemble of charged particles, but not for an individual particle as an individual particle has discrete hard body collisions whereas the ensemble experiences an average over these collisions. This average can be considered as the continuous drag frictional collision frequency. The gravitational force on the charged particle is ignored because the gravitational force is seven orders of magnitude smaller than the magnetic force. The exact solution for Equation (7.5) is

$$\mathbf{u}_\sigma = \left(\mathbf{u}_L \cos\left(\omega_{c\sigma} t\right) - \hat{z} \times \mathbf{u}_L \sin\left(\omega_{c\sigma} t\right)\right) e^{-\nu_{\sigma n} t} + \frac{\xi_\sigma^2 \mathbf{u}_n + \xi_\sigma \mathbf{u}_n \times \hat{z}}{1 + \xi_\sigma^2} \tag{7.6}$$

where $\xi = \nu_{\sigma n}/\omega_{c\sigma}$. On time-averaging, the terms containing $\cos\left(\omega_{c\sigma} t\right)$ and $\sin\left(\omega_{c\sigma} t\right)$ vanish so the time-averaged velocity of the ensemble of charged particles σ is

$$\mathbf{u}_\sigma = \frac{\xi_\sigma^2 \mathbf{u}_n + \xi_\sigma \mathbf{u}_n \times \hat{z}}{1 + \xi_\sigma^2}. \tag{7.7}$$

We presume that the neutrals are in free-fall motion so $\mathbf{u}_n$ is in the negative $\hat{r}$ direction. The radial component of the time-averaged charged particle velocity is thus

$$u_{\sigma r} = \frac{\xi_\sigma^2}{1 + \xi_\sigma^2} u_{nr} \tag{7.8}$$

which is negative.

Equation (7.8) shows that a charged particle is entrained with the neutrals if $\xi_\sigma \gg 1$ but is radially at rest if $\xi_\sigma \ll 1$. Using $\bar{\omega}_{ci} = +30$ and $\bar{\nu}_{in} = 45$ gives $\xi_i = 1.5$ so $u_{ir} = 0.7 u_{nr}$ while using $\bar{\omega}_{ce} = -3000$ and $\bar{\nu}_{en} = 238$ gives $\xi_e = 0.08$ so $u_{er} = 0.006 u_{nr}$. The ions are thus nearly entrained with the infalling neutrals whereas the electrons are nearly stationary. This causes ions to drift radially inwards whereas electrons are left behind. The radial motion difference between ions and electrons reduces total charged particle CAM and so neutrals gain OAM due to the conservation of overall system CAM.

Figure 7.1 (f) compares the ξ_i dependence of u_{ir}/u_{nr} observed in different simulations with the Equation (7.8) prediction. The velocity is obtained at $\bar{t} = 0.2$ from the simulations which are arranged to be different by varying the cyclotron frequency ω_{ci} and the collision frequency ν_{in}. The radial velocity from the simulations agrees well with Equation (7.8).

The predicted neutral particle OAM generation rate is derived by considering the total system CAM in a thin annulus having nominal radius r and containing colliding neutrals, electrons, and ions. The CAM in this annulus is

$$P_\theta = m_n \sum_{j=1}^{N_n} r_{nj} v_{n\theta j} + \frac{q_i}{2\pi} \sum_{j=1}^{N_i} \psi(r_{ij}) + \frac{q_e}{2\pi} \sum_{j=1}^{N_e} \psi(r_{ej}) \tag{7.9}$$

where N_n, N_i, and N_e are the respective numbers of neutrals, ions, and electrons and r_{nj} is the position of the j^{th} neutral, $v_{n\theta j}$ is the θ component of the velocity of the j^{th} neutral, etc. The OAM of the charged particles has been dropped because it is negligible compared to the magnetic part of their CAM. Because a colliding pair of particles are at the same position at the instants before and after they collide, ψ does not change during a collision because it is a function of position. Thus, because ψ and OAM are conserved in a collision, a collision does not change the CAM of a

pair of colliding particles. Finally, the CAM of individual particles is individually conserved for time intervals between collisions. Thus, the total system CAM is conserved in the collisional axisymmetric system.

This conservation can be expressed as

$$\Delta P_\theta = \sum_{j=1}^{N_n} \Delta\left(m_n r_{nj} v_{n\theta j}\right) + \frac{q_i}{2\pi}\sum_{j=1}^{N_i} \Delta\psi(r_{ij}) + \frac{q_e}{2\pi}\sum_{j=1}^{N_e} \Delta\psi(r_{ej}) = 0 \tag{7.10}$$

and remains true after a short time Δt during which the j^{th} particle of species σ makes the incremental displacement $\Delta r_j = v_{\sigma rj}\Delta t$ in which case $\Delta\psi(r_{\sigma j}) = \frac{\partial\psi}{\partial r} v_{\sigma rj}\Delta t = 2\pi B r_{\sigma j} v_{\sigma rj}\Delta t$.

Since Δt is small, $r_{nj} \simeq r_{ij} \simeq r_{ej} \simeq r$ so Equation (7.10) can be re-arranged as

$$\sum_{j=1}^{N_n} \frac{\Delta\left(m_n r v_{n\theta j}\right)}{\Delta t} = -rB\left(q_i \sum_{j=1}^{N_i} v_{irj} + q_e \sum_{j=1}^{N_e} v_{erj}\right). \tag{7.11}$$

On defining the volume of the annulus to be V, the respective neutral, ion, and electron densities are $n_n = N_n/V$, $n_i = N_i/V$ and $n_e = N_e/V$ so Equation (7.11) can be written as

$$\frac{\Delta\left(n_n m_n r u_{n\theta}\right)}{\Delta t} = -rB\left(q_i n_i u_{ir} + q_e n_e u_{er}\right) \tag{7.12}$$

where $u_{n\theta} = N_n^{-1}\sum_{j=1}^{N_n} v_{n\theta j}$ is the mean neutral θ velocity and u_{ir}, u_{er} are the mean radial velocities of ions and electrons. The radial current density is $J_r = q_i n_i u_{ir} + q_e n_e u_{er}$ so

$$\frac{\Delta\left(n_n m_n r u_{n\theta}\right)}{\Delta t} = -rJ_r B. \tag{7.13}$$

From the particle point of view, Equation (7.12) shows that ions and electrons drift at different radial velocities and convert their CAM into neutral particle OAM. From the macroscopic (fluid) point of view, Equation (7.13) shows that magnetic torque caused by the radial current density interacting with the magnetic field generates the fluid OAM.

Figure 7.2 displays simulation results with a large number of ions and electrons. Figure 7.2 (a-c) show the system at $\bar{t} = 0$, 0.2, and 0.4. Figure 7.2 (d) presents the average radial position of ions and electrons with $\langle\bar{r}_i\rangle = \sum_{j=1}^{N_i} \bar{r}_{ij}\big/N_i$ and $\langle\bar{r}_e\rangle = \sum_{j=1}^{N_e} \bar{r}_{ej}\big/N_e$. Ions drift inward, but electrons are left behind. The total CAM is conserved during this process, as presented in Figure 7.2 (e). With the decrease of

charged particle CAM, neutral OAM increases by an equal amount. Figure 7.2 (f) shows the neutral particle OAM generation rate at time $\bar{t} = 0.2$; this rate is in good agreement with Equation (7.12).

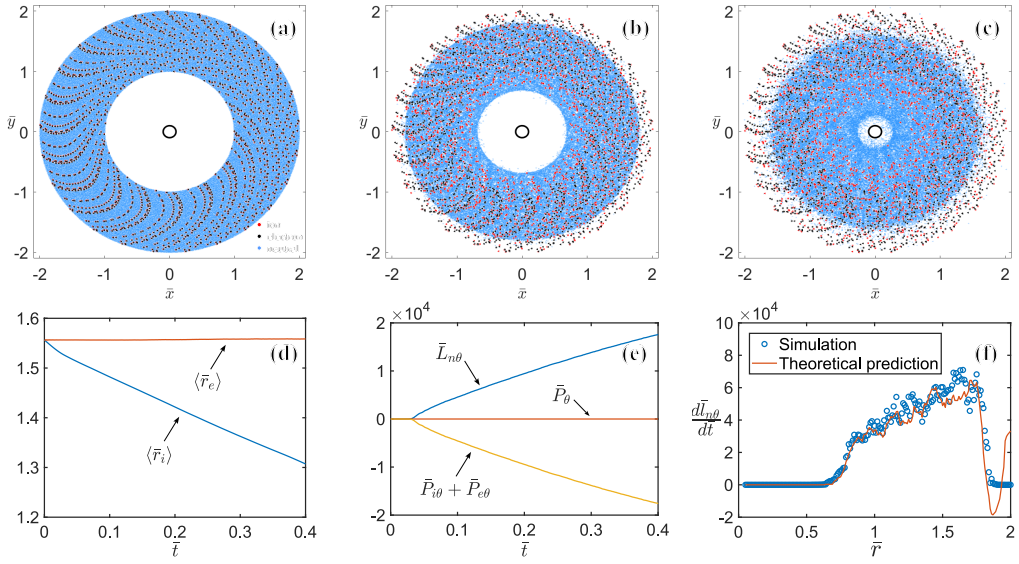

Figure 7.2: **Simulation results when there are a lot of ions and electrons in the system.** (a, b, c) Particle trajectories at $\bar{t} = 0$, 0.2 and 0.4 for $N_n = 91430$ neutrals, $N_i = 1905$ ions and $N_e = 1905$ electrons initially located in concentric circles ranging from $\bar{r} = 1$ to $\bar{r} = 2$. The ions and electrons are initially in adjacent pairs separated by a small azimuthal angle. The initial velocity is a free-fall velocity. (d) The average radial position of ions and electrons. (e) The total system CAM, total neutral OAM, and total charged particle CAM. (f) Comparison of simulated radial angular momentum density change rate with theoretical prediction by Equation (7.12) at $\bar{t} = 0.2$.

From Equations (7.12) and (7.13), the sign of the angular momentum generation rate depends on the magnetic field direction. As a result, the rotation direction should be the same as the magnetic field direction for angular momentum generation by ions entrained by infalling neutrals. This magnetic field dependence has been observed previously from a Hall-MHD simulation of the disk formation showing that the disk rotation direction is the same as the initial magnetic field direction [117].

We now estimate the characteristic time needed to generate a Keplerian angular momentum density. Substituting $\Delta\left(n_n m_n r_n u_{n\theta}\right) = n_n m_n r_n v_K$ in Equation (7.12) and using Equation (7.8), the characteristic time is

$$\tau \sim \frac{1}{-\frac{m_i}{m_n}\chi\omega_{ci}\frac{u_{nr}}{v_K}\left(\frac{\xi_i^2}{1+\xi_i^2}-\frac{\xi_e^2}{1+\xi_e^2}\right)} \tag{7.14}$$

where $\chi = n_i/n_n$ is the ionization fraction.

For free fall neutrals, $u_{nr} = -\sqrt{2GM_*/r_n} = -\sqrt{2}v_K$ giving

$$\tau \sim \frac{1}{\sqrt{2}\frac{m_i}{m_n}\chi\omega_{ci}\left(\frac{\xi_i^2}{1+\xi_i^2}-\frac{\xi_e^2}{1+\xi_e^2}\right)}. \tag{7.15}$$

To check the efficiency of this angular momentum generation mechanism, we compare the characteristic time with the free fall time $\tau_{freefall} \sim r_n/u_{nr} = \sqrt{2}\Big/\omega_K$

$$\frac{\tau}{\tau_{freefall}} \sim \frac{1}{\frac{m_i}{m_n}\chi\frac{\omega_{ci}}{\omega_K}\left(\frac{\xi_i^2}{1+\xi_i^2}-\frac{\xi_e^2}{1+\xi_e^2}\right)}. \tag{7.16}$$

Let us consider the transition from free-fall to Kepler motion at $r = 100$ a.u. in a protoplanetary accretion disk using physically realistic approximations for collision frequencies and ionization fraction. The collision frequency between charged particles and neutrals, taking into account dipole moment effects of neutrals, is $\nu_{\sigma n} = \frac{m_n}{m_n+m_\sigma}n_n\langle\sigma v\rangle_{\sigma n}$ where typical values of the rate coefficients [105] are $\langle\sigma v\rangle_{in} = 1.9\times10^{-9}$ cm$^3\cdot$s^{-1} and $\langle\sigma v\rangle_{en} = 1.0\times10^{-15}$ cm$^2\left(\frac{128kT_e}{9\pi m_e}\right)^{\frac{1}{2}}$. At $r = 100$ a.u., we presume $n_n = 10^{14}$ m^{-3} [106] and $B = 1$ μG [5]. No direct measurement of the ionization fraction exists but numerical models [107, 108, 120] predict χ is 10^{-9} to 10^{-6}. We assume $\chi = 10^{-7}$, $T_e = 10$ K, $m_i = m_H = 1.66\times10^{-27}$ kg, $m_n = m_{H_2} = 3.32\times10^{-27}$ kg. Then $|\xi_i| = 14$ and $|\xi_e| = 0.014$. Thus, $\tau\big/\tau_{freefall} \sim 0.42$. This result is fairly insensitive to the precise values of ξ_i and of ξ_e so long as the former is much larger than unity and the latter is much smaller than unity. As the characteristic time is around the order of the free fall time, this angular momentum mechanism can efficiently cause initially free-falling neutrals to develop Kepler rotation. This creation of angular momentum is energetically favorable since the kinetic energy of an infalling neutral at a radius r is twice that of the same neutral undergoing Kepler rotation at this radius. Angular momentum is not conserved, but this is not a problem because what counts, namely canonical angular momentum, is conserved.

We now consider how these results relate to an actual measured accretion disk system. From Equation (7.12), $\frac{\Delta}{\Delta t}n_nm_nru_{n\theta} = \frac{d}{dt}n_nm_nru_{n\theta} = \frac{\partial}{\partial t}n_nm_nru_{n\theta} + \nabla\cdot$

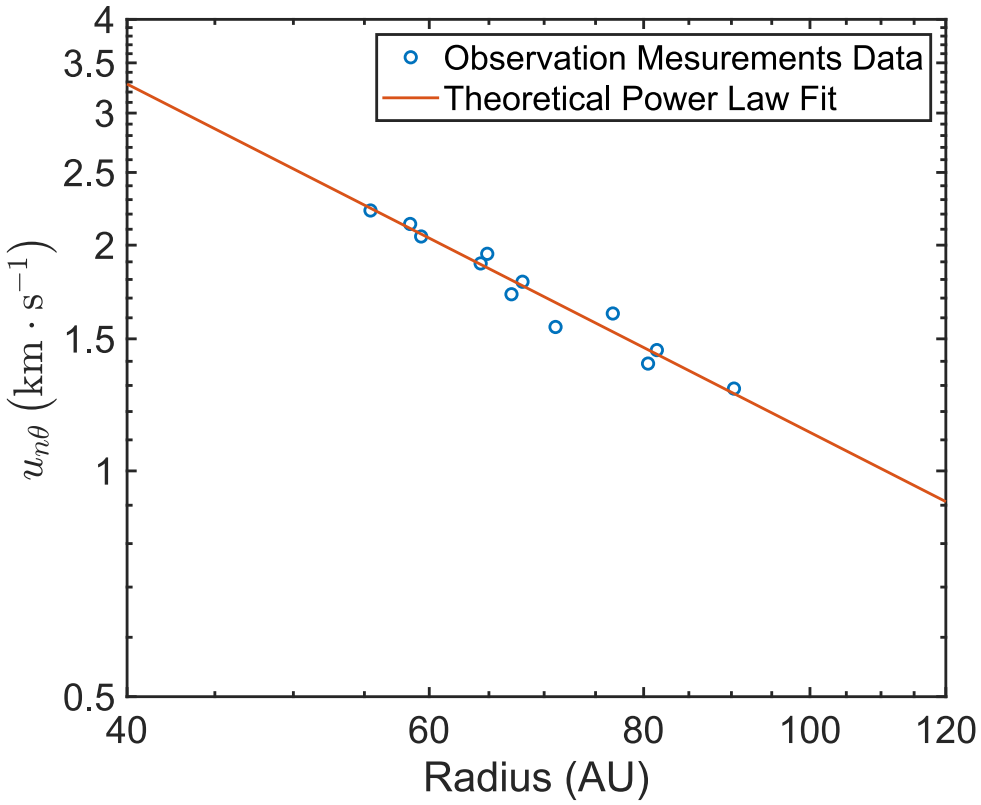

Figure 7.3: **Rotation velocity radial distribution profile of L1527 IRS from 50 a.u. to 100 a.u.** The scattered points are observation measurements extracted from reference [114]. The red line is a power law fit with $r^{-1.17}$. Reasonable assumptions on the magnetic field and ionization fraction can generate this power law fit.

$n_n m_n r u_{n\theta}\mathbf{u}$. For steady state and only considering the radial derivative, $\frac{\partial}{\partial t} n_n m_n r u_{n\theta} = 0$ and $\nabla \cdot n_n m_n r u_{n\theta}\mathbf{u} \approx \frac{1}{r}\frac{\partial}{\partial r} r n_n m_n u_{nr} r u_{n\theta}$. Assuming that ions are tightly coupled with the neutrals while electrons are not, $u_{ir} \approx u_{nr}$ and $u_{er} \approx 0$. Then,

$$\frac{1}{r}\frac{\partial}{\partial r}\left(r^2 n_n u_{nr} m_n u_{n\theta}\right) = -r n_n u_{nr} q_i B_i \chi. \tag{7.17}$$

ALMA measurements [114] of the rotation velocity of accretion disk L1527 IRS are plotted in Figure 7.3 and show that the rotation velocity from 50 a.u. to 100 a.u. is fit by the power law dependence $u_{n\theta} \propto r^k$ where $k = -1.17$. Assuming that the other factors in Equation7.17 follow the power laws $r^2 n_n u_{nr} \propto r^\alpha$, $\chi \propto r^\beta$, and $B \propto r^\eta$ it is seen that Equation7.17 implies $\eta + \beta = k - 1 = -2.17$. Models by Woitke *et al.* [120] and by Walsh *et al.* [108] predict that the ionization fraction increases with radius with $\beta \approx 1$ which consequently implies the quite plausible magnetic decay factor $\eta \simeq -3$. A detailed test of this model could be made by simultaneous

measurements of k, η and β.

This mechanism also sheds light on the origin of the angular momentum of other astrophysical systems, such as galaxies [121] and molecular clouds [122], where the rotation may be a clue to the physical conditions under which these systems formed. Certainly, the angular momentum related rotation is an important test of any theory for the origin of rotating astrophysical systems [122].

In summary, we have presented a robust angular momentum generation mechanism that operates in a weakly ionized plasma having a magnetic field. Ions and electrons colliding with neutrals drift inwards at different velocities because of a magnetic field and so convert their CAM into neutral OAM by magnetic torque. The process is shown in the diagram of Figure 7.4.

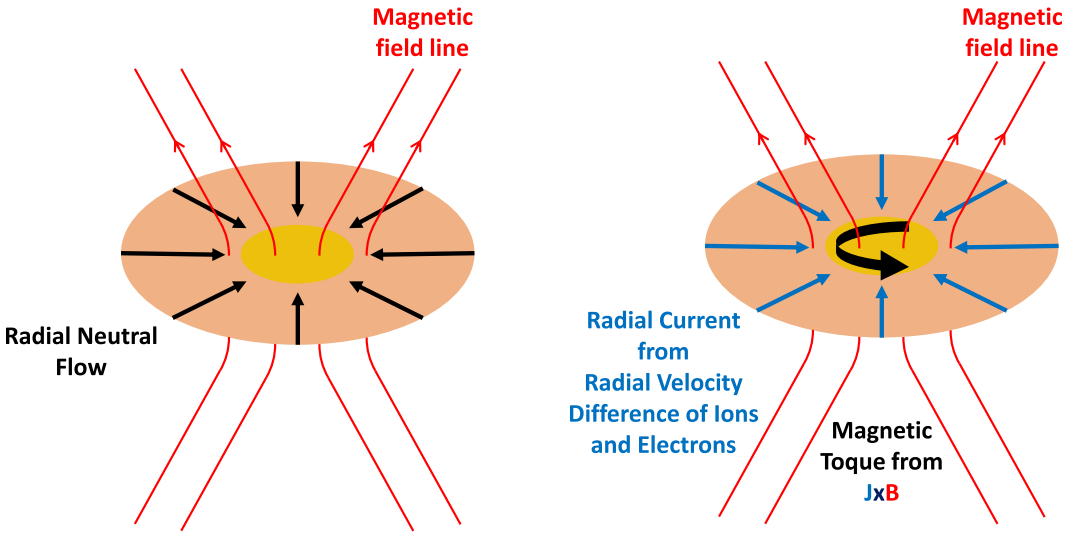

Figure 7.4: **Diagram of the spinning up mechanism in a disk system.** Radial neutral flow entrains ions but not electrons so generate a radial current. The magnetic toque from the $\mathbf{J} \times \mathbf{B}$ force spins up the system. This diagram also applies to a 3D collapsing cloud system where inhomogeneous angular momentum may be generated along different axes while the total angular momentum will be a net in a certain orientation due to inhomogeneity and magnetic field direction.

Chapter 8

SUMMARY AND FUTURE WORKS

8.1 Summary

This dissertation describes investigations of two big questions: how solar flare is generated and how accretion disk transports angular momentum and generates astrophysical jets. Through experiments and associated models, significant insights have been attained. The key findings include:

The dependence of the magnetic Rayleigh-Taylor instability on magnetic fields
We observed that magnetic Rayleigh-Taylor instability developed on a laboratory plasma loop and showed that magnetic Rayleigh-Taylor instability wavelength increases with the increase of background magnetic field strength. This provides a possible explanation of the different observed plume dynamics in the solar prominences and also points out a possible magnetic field measurement method from the magnetic Rayleigh-Taylor instability wavelength.

Laboratory nanoflares generated from braided magnetic flux ropes
We replicated the braided feature of solar coronal loops. Transient, localized 7.6-keV X-ray bursts and a several-kilovolt voltage spike are observed in braided magnetic flux ropes of a 2-eV plasma when the braid strand radius is choked down to be at the kinetic scale by either MHD kink or magnetic Rayleigh–Taylor instabilities. The energy burst is of nanoflare feature with multiple separated observed X-ray bursts observed from multiple strands breaking at different time. This sequence of observations reveals a cross-scale coupling from MHD to non-MHD physics that is likely responsible for generating solar energetic particles and X-ray bursts.

Equilibrium of braided magnetic flux ropes with the same direction current
We provided a systematic method for constructing braided magnetic flux rope equilibria. This method generates a double helix equilibrium with net axial current which is characteristic of observed solar loops and of laboratory-produced braided magnetic flux ropes. To the best of our knowledge, no previous model has been able to describe braided structures with net axial current and instead has only described braided structures with no net axial current; these no-net current structures

had equal-magnitude positive and negative axial currents. The net-axial-current equilibrium presented here reproduces the observed braided structure of the double helix nebula and is expected to be a powerful tool in other contexts.

Accretion disk angular momentum shedding mechanism

We proposed an angular momentum transport mechanism based only on the collisions between neutrals and charged particles and the basic conserved quantity canonical angular momentum. Collisions between neutrals and charged particles cause: (i) ions to move radially inwards, (ii) electrons to move radially outwards, (iii) neutrals to lose ordinary angular momentum, and (iv) charged particles to gain canonical angular momentum. Neutrals thus spiral inward due to their decrease of ordinary angular momentum. Quantitative scaling of the model using plausible disk density, temperature, and magnetic field strength gives an accretion rate of 3×10^{-8} solar mass per year, which is in good agreement with observed accretion rates. This mechanism also naturally provides a gravitational dynamo process converting gravitational energy into electric field energy that powers astrophysical jets.

Mechanism for generation of angular momentum in an astrophysical system

We presented a mechanism for the spontaneous generation of angular momentum in astrophysical contexts. This mechanism depends on the combined presence of gravitational and magnetic fields and generates angular momentum via collisions between small numbers of charged particles and numerous, free-falling neutral particles. The mechanism is demonstrated by a 2D simulation of an N-body weakly-ionized system where ions and electrons develop different mean velocities upon colliding with free-falling neutrals. This velocity difference causes ions and electrons to decrease their canonical angular momentum while at the same time the neutrals gain ordinary angular momentum. The net result is that the total system canonical angular momentum is conserved as predicted by Langrangian mechanics for an axisymmetric system. This shows that a weakly-ionized initially non-rotating cloud of neutral particles will spontaneously start rotating when infalling. Quantitative scaling predicts an angular momentum generation rate sufficient to convert neutral infall motion into neutral Keplerian rotation in the outer region of a protoplanetary accretion disk.

8.2 Future Work

Following the thesis work, numerous intriguing avenues for further investigation have emerged. This thesis has laid the groundwork for exploring particle acceleration

resulting from the coupling between MHD instabilities and kinetic instabilities, the dynamics of braided magnetic flux ropes, and the particle-level dynamics of accretion disk. Here are several potential projects that could be pursued in the future:

Kinetic simulation of the particle acceleration process

Experimental measurements in Chapter 4 have provided insights into electron acceleration, although ion acceleration remains unmeasured due to limitations in detector size. However, understanding ion acceleration in detail is crucial. Particularly, the energy distribution of accelerated ions is of significant interest. Expanding on this experimental setup, a kinetic simulation can be developed to closely replicate the experimental conditions. This simulation enables a more detailed investigation of the particle acceleration process for both electrons and ions. Specifically, we can extract the energy spectrum of charged particles and compare it with the power law distribution of solar energetic particles.

Experiment verification of braided magnetic flux ropes equilibrium

In Chapter 6, we developed a helical current wire model capable of attaining a double helix equilibrium with currents flowing in the same direction. This equilibrium configuration has the potential to be reproduced in laboratory settings using two braided current wires. Initial experiments, conducted by Adele Payman, Joshua Morgan, and myself, utilized direct current, but we encountered challenges due to limitations in the exerted force. Typically, the magnetic force involved is relatively weak, requiring the generation of high currents to overcome the bending force exerted by the materials. Currently, we are in the process of designing a pulsed power setup aimed at generating a significantly stronger current and magnetic force.

Self-similar braided magnetic flux ropes

In magnetohydrodynamics, there is not an inherent scale, meaning the braiding behavior persists until reaching the kinetic scale, specifically the ion skin depth. A self-similar object exhibits exact or approximate similarity to a portion of itself. Figure 8.1 illustrates the self-similar structure of braided magnetic flux ropes, where this structure implies that one flux rope within a system of two braided magnetic flux ropes can be composed of a second level of two braided magnetic flux ropes. The magnetic field energy of such a system is described by the equation:

$$\int \frac{B^2}{2\mu_0} d^3r = \frac{LI^2}{2} = \frac{L^2I^2}{2L} = \frac{\Phi^2}{2L} \tag{8.1}$$

where L represents the system inductance and $\Phi = LI$ denotes the magnetic flux. In a system conserving magnetic flux, higher inductance corresponds to lower magnetic field energy. Hence, a flux-conserving system tends to exhibit higher inductance. The self-similar braided magnetic flux rope structure possesses higher inductance compared to an unbraided flux rope structure. Consequently, the braided structure represents a lower-energy configuration than an unbraided structure containing the same magnetic flux, indicating that it is energetically favorable for systems to exhibit braided configurations in order to conserve flux.

To my knowledge, no study of self-similar braided magnetic flux ropes has been done. However, using the current wire model discussed in Chapter 5, an equilibrium for the self-similar structure can be constructed.

It is also possible to explore the self-similar structure in laboratory experiments. Braided structures have been successfully generated in the solar loop experiment. The strand radius is very close to ion skin depths, so we do not have the observation of a self-similar structure. However, the strand radius closely approximates ion skin depths, precluding the observation of a self-similar structure. Achieving self-similarity requires the strand to have a larger radius compared to the ion skin depth. Although the current setup does not facilitate this observation, it is conceivable to design an experiment specifically tailored to study the self-similar structure.

Accretion disk magnetic field

Measurements indicate that the magnetic field within an accretion disk is around the miligauss level at a distance of a few a.u. If we presume that this field originates solely from the central star, which has a sun radius equivalent to 0.00465 a.u., and follows a decay proportional to r^{-3}, then a magnetic field of 1 tesla would be required at the star surface. This is significantly greater than the average surface magnetic field of a star, which typically measures around 1 gauss. Consequently, it suggests that the magnetic field within the accretion disk must stem from an alternative source.

To date, there is no comprehensive model detailing the generation of magnetic fields within accretion disks. In Chapters 6 and 7, our focus primarily centers on the radial motion of charged particles. However, by considering the azimuthal motion of these particles, it becomes feasible to generate an azimuthal current capable of driving a poloidal magnetic field. By deriving the distribution of azimuthal current density, denoted as $J_\theta(r, z)$, it becomes possible to calculate the magnetic

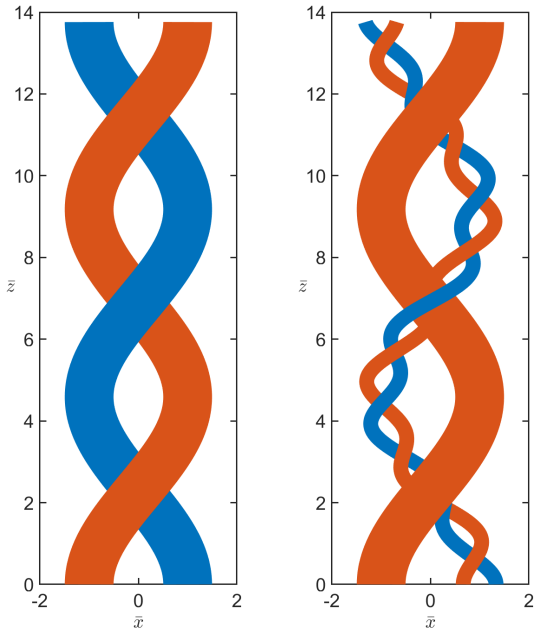

Figure 8.1: **Self-similar braided magnetic flux ropes.** (a) double helix braided magnetic flux ropes (b) self-similar braided magnetic flux ropes of (a). The blue flux rope is composed a new double helix braided magnetic flux ropes.

field under a specific current distribution. This process can be executed utilizing a Green's function method akin to the one employed in Chapter 5.

A comprehensive model for the dynamics in the accretion disk

In our previous studies, we have examined various physical processes within the accretion disk independently, including angular momentum transport in the Keplerian motion region, angular momentum generation in the free-fall region, and the generation of astrophysical jets. My aim is to integrate the physics of different regions to elucidate the complete dynamics of particle motion and establish a closed current circuit for the astrophysical jets within the accretion disk, as depicted in Figure 8.2. To accomplish this objective, it is imperative to develop a coherent 3D three-fluid simulation of the disk. Such a simulation will allow us to unveil the dynamics of different species and the associated physics across various regions of the accretion disk.

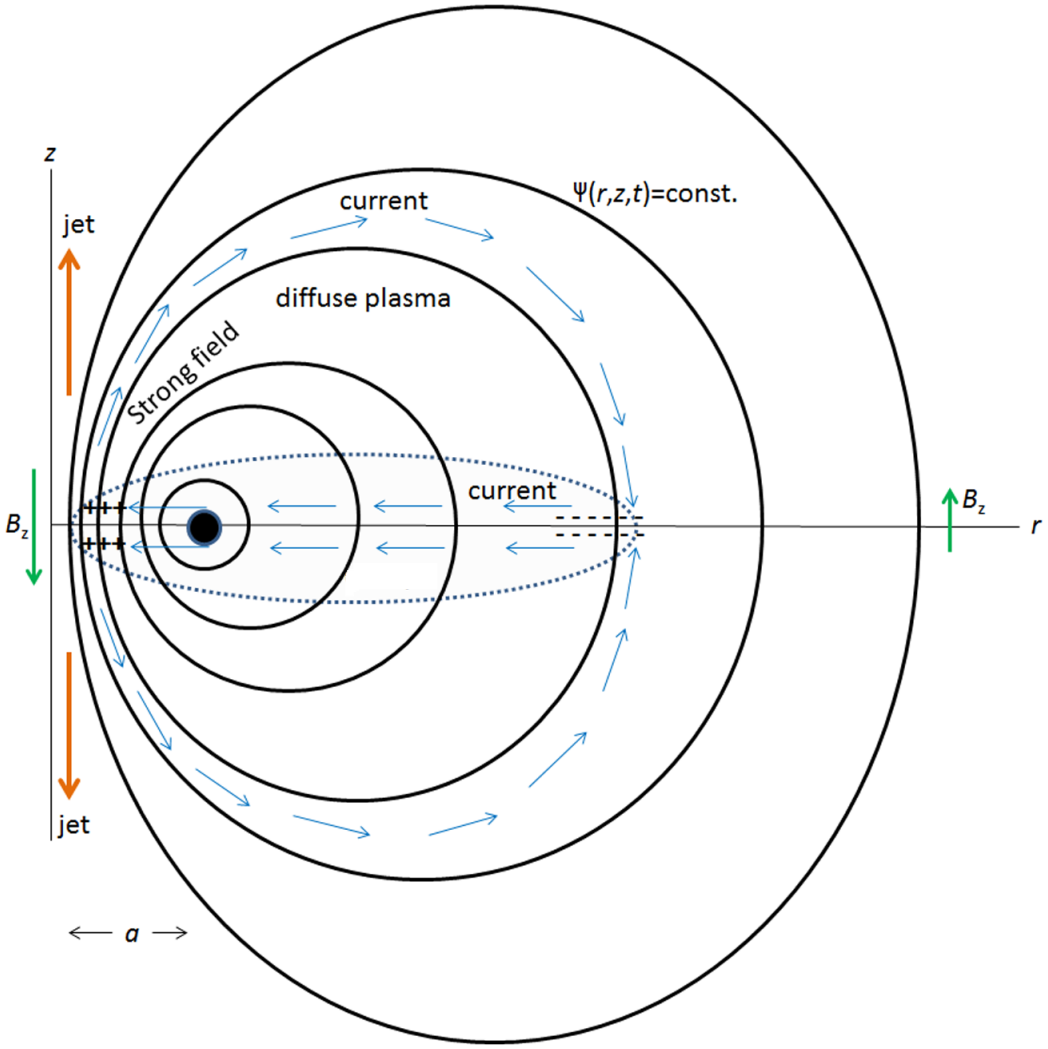

Figure 8.2: **A comprehensive diagram for the dynamics in the accretion disk.** Dense weakly ionized gas inside dotted line ellipse. The accumulation of ions at smaller radius and accumulation of electrons at bigger radius drives currents away from the z-axis. These currents drive astrophysical jets away from the z-axis and flow back to large radius along poloidal flux surfaces. This Figure is adapted from [97].

BIBLIOGRAPHY

1. Bellan, P. M. *Fundamentals of plasma physics* (Cambridge University Press, 2008).

2. Ryutov, D., Drake, R. & Remington, B. Criteria for scaled laboratory simulations of astrophysical MHD phenomena. *The Astrophysical Journal Supplement Series* **127,** 465 (2000).

3. Aso, Y. *et al.* ALMA observations of the protostar L1527 IRS: Probing details of the disk and the envelope structures. *The Astrophysical Journal* **849,** 56 (2017).

4. Andrews, S. M. *et al.* The disk substructures at high angular resolution project (DSHARP). I. Motivation, sample, calibration, and overview. *The Astrophysical Journal Letters* **869,** L41 (2018).

5. Harrison, R. E. *et al.* ALMA CN Zeeman observations of AS 209: Limits on magnetic field strength and magnetically driven accretion rate. *The Astrophysical Journal* **908,** 141 (2021).

6. Gullbring, E., Hartmann, L., Briceno, C. & Calvet, N. Disk accretion rates for T Tauri stars. *The Astrophysical Journal* **492,** 323 (1998).

7. McCaughrean, M., Zinnecker, H., Andersen, M., Meeus, G. & Lodieu, N. Standing on the shoulder of a giant: ISAAC, Antu, and star formation. *The Messenger (ISSN 0722-6691), No. 109, p. 28-36 (September 2002)* **109,** 28–36 (2002).

8. Lee, C.-F. *et al.* First detection of equatorial dark dust lane in a protostellar disk at submillimeter wavelength. *Science Advances* **3,** e1602935 (2017).

9. Lee, C.-F. *et al.* A rotating protostellar jet launched from the innermost disk of HH 212. *Nature Astronomy* **1,** 0152 (2017).

10. Lee, C.-F. *et al.* Formation and atmosphere of complex organic molecules of the HH 212 protostellar disk. *The Astrophysical Journal* **843,** 27 (2017).

11. Haw, M. A. *Experimental and Numerical Studies of Cavities, Flows, and Waves in Arched Flux Ropes.* PhD thesis (California Institute of Technology, 2018).

12. Zhou, Y., Pree, S. & Bellan, P. M. Imaging suprathermal x-rays from a laboratory plasma jet using PIN-diode-based and scintillator-based 1D pinhole/coded aperture cameras. *Review of Scientific Instruments* **94** (2023).

13. Ha, Q. B. N. *Plasma Loop and Strapping Field Dynamics: Reproducing Solar Eruptions in the Laboratory.* PhD thesis (California Institute of Technology, 2016).

14. Aschwanden, M. *Physics of the solar corona: An introduction with problems and solutions* (Springer Science & Business Media, 2006).

15. Hansen, J. F., Tripathi, S. & Bellan, P. M. Co-and counter-helicity interaction between two adjacent laboratory prominences. *Physics of Plasmas* **11,** 3177–3185 (2004).

16. Tripathi, S., Bellan, P. & Yun, G. Observation of kinetic plasma jets in a coronal-loop simulation experiment. *Physical Review Letters* **98,** 135002 (2007).

17. Stenson, E. V. & Bellan, P. Magnetically driven flows in arched plasma structures. *Physical Review Letters* **109,** 075001 (2012).

18. Ha, B. N. & Bellan, P. M. Laboratory demonstration of slow rise to fast acceleration of arched magnetic flux ropes. *Geophysical Research Letters* **43,** 9390–9396 (2016).

19. Haw, M. A. & Bellan, P. M. MHD collimation mechanism in arched flux ropes characterized using volumetric, time-dependent B-vector measurements. *Geophysical Research Letters* **44,** 9525–9531 (2017).

20. Haw, M. A., Wongwaitayakornkul, P., Li, H. & Bellan, P. M. Reverse current model for coronal mass ejection cavity formation. *The Astrophysical Journal Letters* **862,** L15 (2018).

21. Wongwaitayakornkul, P., Haw, M. A., Li, H., Li, S. & Bellan, P. M. Apex dips of experimental flux ropes: Helix or cusp? *The Astrophysical Journal* **848,** 89 (2017).

22. Wongwaitayakornkul, P., Haw, M. A., Li, H. & Bellan, P. M. Magnetically induced current piston for generating extreme-ultraviolet fronts in the solar corona. *The Astrophysical Journal* **874,** 137 (2019).

23. Moser, A. L. & Bellan, P. M. Magnetic reconnection from a multiscale instability cascade. *Nature* **482,** 379–381 (2012).

24. Hachisu, I., Matsuda, T., Nomoto, K. & Shigeyama, T. Mixing in ejecta of supernovae. I-General properties of two-dimensional Rayleigh-Taylor instabilities and mixing width in ejecta of supernovae. *The Astrophysical Journal* **390,** 230–252 (1992).

25. Hester, J. J. *et al.* WFPC2 studies of the Crab Nebula. III. magnetic Rayleigh-Taylor instabilities and the origin of the filaments. *Astrophysical Journal* **456,** 225–233 (1996).

26. Porth, O., Komissarov, S. S. & Keppens, R. Rayleigh–Taylor instability in magnetohydrodynamic simulations of the Crab nebula. *Monthly Notices of the Royal Astronomical Society* **443,** 547–558 (2014).

27. Berger, T. E. *et al.* Quiescent prominence dynamics observed with the Hinode solar optical telescope. I. Turbulent upflow plumes. *The Astrophysical Journal* **716,** 1288 (2010).

28. Ryutova, M., Berger, T., Frank, Z., Tarbell, T., *et al.* Observation of plasma instabilities in quiescent prominences. *Solar Physics* **267,** 75–94 (2010).

29. Terradas, J., Soler, R., Luna, M., Oliver, R. & Ballester, J. Morphology and dynamics of solar prominences from 3D MHD simulations. *The Astrophysical Journal* **799,** 94 (2015).

30. Hillier, A. The magnetic Rayleigh–Taylor instability in solar prominences. *Reviews of Modern Plasma Physics* **2,** 1 (2018).

31. Takabe, H., Mima, K., Montierth, L. & Morse, R. Self-consistent growth rate of the Rayleigh–Taylor instability in an ablatively accelerating plasma. *The Physics of fluids* **28,** 3676–3682 (1985).

32. Betti, R., Goncharov, V., McCrory, R. & Verdon, C. Growth rates of the ablative Rayleigh–Taylor instability in inertial confinement fusion. *Physics of Plasmas* **5,** 1446–1454 (1998).

33. Zhou, Y. Rayleigh–Taylor and Richtmyer–Meshkov instability induced flow, turbulence, and mixing. II. *Physics Reports* **723,** 1–160 (2017).

34. Goedbloed, H., Keppens, R. & Poedts, S. *Magnetohydrodynamics: Of Laboratory and Astrophysical Plasmas* (Cambridge University Press, 2019).

35. Kruskal, M. D. & Schwarzschild, M. Some instabilities of a completely ionized plasma. *Proceedings of the Royal Society of London. Series A. Mathematical and Physical Sciences* **223,** 348–360 (1954).

36. Zhai, X. & Bellan, P. M. A hybrid Rayleigh-Taylor-current-driven coupled instability in a magnetohydrodynamically collimated cylindrical plasma with lateral gravity. *Physics of Plasmas* **23,** 032121 (2016).

37. Hillier, A., Berger, T., Isobe, H. & Shibata, K. Numerical simulations of the magnetic Rayleigh-Taylor instability in the Kippenhahn-Schlüter prominence model. I. Formation of upflows. *The Astrophysical Journal* **746,** 120 (2012).

38. Keppens, R., Xia, C. & Porth, O. Solar prominences: "Double, Double... Boil and Bubble,". *The Astrophysical Journal Letters* **806,** L13 (2015).

39. Lebedev, S. *et al.* Azimuthal structure and global instability in the implosion phase of wire array Z-pinch experiments. *Physical Review Letters* **81,** 4152 (1998).

40. Sinars, D. *et al.* Measurements of magneto-Rayleigh-Taylor instability growth during the implosion of initially solid Al tubes driven by the 20-MA, 100-ns Z facility. *Physical Review Letters* **105,** 185001 (2010).

41. De Grouchy, P. *et al.* Observations of the magneto-Rayleigh-Taylor instability and shock dynamics in gas-puff Z-pinch experiments. *Physics of Plasmas* **25,** 072701 (2018).

42. Shafranov, V. Plasma equilibrium in a magnetic field. *Reviews of Plasma Physics* **2,** 103 (1966).

43. Stenson, E. V. *Fields, Forces, and Flows: What Laboratory Experiments Reveal About the Dynamics of Arched Plasma Structures.* PhD thesis (California Institute of Technology, 2012).

44. Kosugi, T. *et al.* The Hinode (Solar-B) mission: An Overview. *Solar Physics,* 3–17 (2007).

45. Hirayama, T. *The density and thickness of quiescent prominences.* in *NASA Conference Publication* **2442** (Dec. 1986), 149–153.

46. Hanssen, E. T. *The nature of solar prominences* (Springer, Dordrecht, 1995).

47. Leroy, J. L. *Observation of prominence magnetic fields* in *Dynamics and Structure of Quiescent Solar Prominences.* (ed Priest, E. R.) (Springer Netherla nds, 1989), 77–113.

48. Marshall, R. S. *Developing Plasma Spectroscopy and Imaging Diagnostics to Understand Astrophysically-Relevant Plasma Experiments: Megameters, Femtometers, and Everything in Between.* PhD thesis (California Institute of Technology, 2020).

49. Cirtain, J. W. *et al.* Energy release in the solar corona from spatially resolved magnetic braids. *Nature* **493,** 501–503 (2013).

50. Testa, P. *et al.* Evidence of nonthermal particles in coronal loops heated impulsively by nanoflares. *Science* **346,** 1255724 (2014).

51. Fleishman, G. D. *et al.* Decay of the coronal magnetic field can release sufficient energy to power a solar flare. *Science* **367,** 278–280 (2020).

52. Bahauddin, S. M., Bradshaw, S. J. & Winebarger, A. R. The origin of reconnection-mediated transient brightenings in the solar transition region. *Nature Astronomy* **5,** 237–245 (2021).

53. Fleishman, G. D., Nita, G. M., Chen, B., Yu, S. & Gary, D. E. Solar flare accelerates nearly all electrons in a large coronal volume. *Nature* **6,** 674–677 (2022).

54. Lemen, J. R. *et al. The atmospheric imaging assembly (AIA) on the solar dynamics observatory (SDO)* in *The Solar Dynamics Observatory.* (Springer, 2011), 17–40.

55. Kobayashi, K. *et al.* The high-resolution coronal imager (Hi-C). *Solar Physics* **289,** 4393–4412 (2014).

56. Parker, E. Magnetic neutral sheets in evolving fields. I - General theory. *The Astrophysical Journal* **264,** 635–647 (1983).

57. Parker, E. Nanoflares and the solar X-ray corona. *The Astrophysical Journal* **330,** 474–479 (1988).

58. Alfvén, H. & Carlqvist, P. Currents in the solar atmosphere and a theory of solar flares. *Solar Physics* **1,** 220–228 (1967).

59. Carlqvist, P. Current limitation and solar flares. *Solar Physics* **7,** 377–392 (1969).

60. Zhang, Y., Wongwaitayakornkul, P. & Bellan, P. M. Magnetic Rayleigh–Taylor instability in an experiment simulating a solar loop. *The Astrophysical Journal Letters* **889,** L32 (2020).

61. Newcomb, W. A. Hydromagnetic stability of a diffuse linear pinch. *Annals of Physics* **10,** 232–267 (1960).

62. Henke, B. L., Gullikson, E. M. & Davis, J. C. X-ray interactions: photoabsorption, scattering, transmission, and reflection at E= 50-30,000 eV, Z= 1-92. *Atomic Data and Nuclear Data Tables* **54,** 181–342 (1993).

63. Buneman, O. Dissipation of currents in ionized media. *Physical Review* **115,** 503–517 (1959).

64. Engelhardt, M. LTspice owned by Analog Devices Inc.; Software available at https://www.analog.com/en/design-center/design-tools-and-calculators/ltspice-simulator.html.

65. Sullivan, C. R. & Zhang, R. Y. *Simplified design method for litz wire* in *IEEE Applied Power Electronics Conference and Exposition-APEC* (2014), 2667–2674.

66. Stix, T. H. Magnetic braiding in a toroidal plasma. *Physical Review Letters* **30,** 833 (1973).

67. Srivastava, A., Zaqarashvili, T., Kumar, P. & Khodachenko, M. Observation of kink instability during small B5. 0 solar flare on 2007 June 4. *The Astrophysical Journal* **715,** 292 (2010).

68. Kumar, P., Cho, K.-S., Bong, S.-C., Park, S.-H. & Kim, Y. Initiation of coronal mass ejection and associated flare caused by helical kink instability observed by SDO/AIA. *The Astrophysical Journal* **746,** 67 (2012).

69. Lin, R. P. *et al.* in *The Reuven Ramaty High-Energy Solar Spectroscopic Imager (RHESSI)* 3–32 (Springer, 2003).

70. Ergun, R. *et al.* Observations of double layers in Earth's plasma sheet. *Physical Review Letters* **102,** 155002 (2009).

71. Osherovich, V., Fainberg, J. & Webb, A. Observational evidence for a double-helix structure in CMEs and magnetic clouds. *Solar Physics* **284,** 261–274 (2013).

72. Hu, Q., Smith, C. W., Ness, N. F. & Skoug, R. M. Double flux-rope magnetic cloud in the solar wind at 1 AU. *Geophysical Research Letters* **30** (2003).

73. Morris, M., Uchida, K. & Do, T. A magnetic torsional wave near the Galactic Centre traced by a 'double helix'nebula. *Nature* **440,** 308–310 (2006).

74. Pasetto, A. *et al.* Reading M87's DNA: A double helix revealing a large-scale helical magnetic field. *The Astrophysical Journal Letters* **923,** L5 (2021).

75. Sun, X. *et al.* Flux rope dynamics: Experimental study of bouncing and merging. *Physical Review Letters* **105,** 255001 (2010).

76. Gekelman, W. *et al.* Spiky electric and magnetic field structures in flux rope experiments. *Proceedings of the National Academy of Sciences* **116,** 18239–18244 (2019).

77. Zhang, Y., Pree, S. & Bellan, P. M. Generation of laboratory nanoflares from multiple braided plasma loops. *Nature Astronomy* **7,** 655–661 (2023).

78. Delgado-Aparicio, L. *et al.* On the formation and stability of long-lived impurity-ion snakes in Alcator C-Mod. *Nuclear Fusion* **53,** 043019 (2013).

79. Lorenzini, R. *et al.* Self-organized helical equilibria as a new paradigm for ohmically heated fusion plasmas. *Nature Physics* **5,** 570–574 (2009).

80. Awe, T. *et al.* Observations of modified three-dimensional instability structure for imploding z-pinch liners that are premagnetized with an axial field. *Physical Review Letters* **111,** 235005 (2013).

81. Cothran, C., Gray, T., Schaffer, M. & Marklin, G. Observation of a helical self-organized state in a compact toroidal plasma. *Physical Review Letters* **103,** 215002 (2009).

82. Zhai, X. *Experimental, Numerical and Analytical Studies of the MHD-driven Plasma jet, Instabilities and Waves.* PhD thesis (California Institute of Technology, 2015).

83. Lavine, E. S. & You, S. Observations of a plectonemic configuration in a stable magnetized plasma jet. *Physics of Plasmas* **28** (2021).

84. Parker, E. Topological dissipation and the small-scale fields in turbulent gases. *The Astrophysical Journal, vol. 174, p. 499* **174,** 499 (1972).

85. Marshall, R. S. & Bellan, P. M. Acceleration of charged particles to extremely large energies by a sub-Dreicer electric field. *Physics of Plasmas* **26,** 042102. ISSN: 1070-664X, 1089-7674. (2022) (Apr. 2019).

86. Johnson, J. L., Oberman, C., Kulsrud, R. & Frieman, E. Some stable hydromagnetic equilibria. *The Physics of Fluids* **1,** 281–296 (1958).

87. Bogoyavlenskij, O. I. Exact helically symmetric plasma equilibria. *Letters in Mathematical Physics* **51,** 235–247 (2000).

88. Tominaka, T., Okamura, M. & Katayama, T. Analytical field calculation of helical coils. *Nuclear Instruments and Methods in Physics Research Section A: Accelerators, Spectrometers, Detectors and Associated Equipment* **459,** 398–411 (2001).

89. Booth, A. S. *et al.* Molecules with ALMA at Planet-forming Scales (MAPS). XVI. Characterizing the impact of the molecular wind on the evolution of the HD 163296 system. *The Astrophysical Journal Supplement Series* **257,** 16 (2021).

90. Hu, Q., He, W., Qiu, J., Vourlidas, A. & Zhu, C. On the quasi-three dimensional configuration of magnetic clouds. *Geophysical Research Letters* **48,** e2020GL090630 (2021).

91. Lau, Y.-T. & Finn, J. Magnetic reconnection and the topology of interacting twisted flux tubes. *Physics of Plasmas* **3,** 3983–3997 (1996).

92. Liu, R. *et al.* Structure, stability, and evolution of magnetic flux ropes from the perspective of magnetic twist. *The Astrophysical Journal* **818,** 148 (2016).

93. Berger, M. A. *Topological Magnetohydrodynamics and Astrophysics* in *Encyclopedia of Complexity and Systems Science* (ed Meyers, R. A.) (Springer New York, New York, NY, 2009), 9268–9282.

94. Gekelman, W. *et al.* Pulsating magnetic reconnection driven by three-dimensional flux-rope interactions. *Physical Review Letters* **116,** 235101 (2016).

95. Daughton, W. *et al.* Role of electron physics in the development of turbulent magnetic reconnection in collisionless plasmas. *Nature Physics* **7,** 539–542 (2011).

96. Cooper, W., Graves, J., Pochelon, A., Sauter, O. & Villard, L. Tokamak magnetohydrodynamic equilibrium states with axisymmetric boundary and a 3D helical core. *Physical Review Letters* **105,** 035003 (2010).

97. Bellan, P. M. Integrated accretion disc angular momentum removal and astrophysical jet acceleration mechanism. *Monthly Notices of the Royal Astronomical Society* **458,** 4400–4421 (2016).

98. Balbus, S. A. Enhanced angular momentum transport in accretion disks. *Annual Review of Astronomy and Astrophysics* **41,** 555–597 (2003).

99. Shakura, N. I. & Sunyaev, R. A. Black holes in binary systems. Observational appearance. *Astronomy and Astrophysics* **24,** 337–355 (1973).

100. Balbus, S. A. & Hawley, J. F. A powerful local shear instability in weakly magnetized disks. I. Linear analysis. II. Nonlinear evolution. *The Astrophysical Journal* **376,** 214–233 (1991).

101. Flaherty, K. M. *et al.* A Three-dimensional view of turbulence: Constraints on turbulent motions in the HD 163296 protoplanetary disk using DCO+. *The Astrophysical Journal* **843,** 150 (2017).

102. Ji, H., Burin, M., Schartman, E. & Goodman, J. Hydrodynamic turbulence cannot transport angular momentum effectively in astrophysical disks. *Nature* **444,** 343–346 (2006).

103. Ji, H. & Balbus, S. Angular momentum transport in astrophysics and in the lab. *Physics Today* **66,** 27 (2013).

104. Boris, J. *Relativistic plasma simulation-optimization of a hybrid code* in *Proceedings of the Fourth Conference on Numerical Simulation of Plasmas* (Naval Research Laboratory, Washington DC, 1970), 3.

105. Draine, B. T., Roberge, W. G. & Dalgarno, A. Magnetohydrodynamic shock waves in molecular clouds. *The Astrophysical Journal* **264,** 485–507 (1983).

106. Hayashi, C. Structure of the solar nebula, growth and decay of magnetic fields and effects of magnetic and turbulent viscosities on the nebula. *Progress of Theoretical Physics Supplement* **70,** 35–53 (1981).

107. Ilgner, M. & Nelson, R. P. On the ionisation fraction in protoplanetary disks I. Comparing different reaction networks. *Astronomy & Astrophysics* **445,** 205–222 (2006).

108. Walsh, C., Nomura, H., Millar, T. & Aikawa, Y. Chemical processes in protoplanetary disks. II. On the importance of photochemistry and X-ray ionization. *The Astrophysical Journal* **747,** 114 (2012).

109. Bellan, P. M. Analytic model for the time-dependent electromagnetic field of an astrophysical jet. *The Astrophysical Journal* **888,** 69 (2020).

110. Hsu, S. C. & Bellan, P. M. A laboratory plasma experiment for studying magnetic dynamics of accretion discs and jets. *Monthly Notices of the Royal Astronomical Society* **334,** 257–261 (2002).

111. You, S., Yun, G. & Bellan, P. M. Dynamic and stagnating plasma flow leading to magnetic-flux-tube collimation. *Physical Review Letters* **95,** 045002 (2005).

112. Kumar, D. & Bellan, P. M. Nonequilibrium Alfvénic plasma jets associated with spheromak formation. *Physical Review Letters* **103,** 105003 (2009).

113. Sakai, N. *et al.* Change in the chemical composition of infalling gas forming a disk around a protostar. *Nature* **507,** 78–80 (2014).

114. Ohashi, N. *et al.* Formation of a Keplerian disk in the infalling envelope around L1527 IRS: Transformation from infalling motions to Kepler motions. *The Astrophysical Journal* **796,** 131 (2014).

115. Crutcher, R. M. Magnetic fields in molecular clouds. *Annual Review of Astronomy and Astrophysics* **50,** 29–63 (2012).

116. Zhang, Y. & Bellan, P. M. Neutral-charged-particle collisions as the mechanism for accretion disk angular momentum transport. *The Astrophysical Journal* **930,** 167 (2022).

117. Krasnopolsky, R., Li, Z.-Y. & Shang, H. Disk formation in magnetized clouds enabled by the hall effect. *The Astrophysical Journal* **733,** 54 (2011).

118. Wurster, J., Bate, M. R. & Bonnell, I. A. The impact of non-ideal magnetohydrodynamic processes on discs, outflows, counter-rotation, and magnetic walls during the early stages of star formation. *Monthly Notices of the Royal Astronomical Society* **507,** 2354–2372 (2021).

119. Bellan, P. M. Integrated accretion disk angular momentum removal and astrophysical jet acceleration mechanism. *Monthly Notices of the Royal Astronomical Society* **458.** 4400-4421 (2016).

120. Woitke, P., Kamp, I. & Thi, W.-F. Radiation thermo-chemical models of protoplanetary disks-I. Hydrostatic disk structure and inner rim. *Astronomy & Astrophysics* **501,** 383–406 (2009).

121. Peebles, P. J. Origin of the angular momentum of galaxies. *The Astrophysical Journal* **155,** 393 (1969).

122. Bodenheimer, P. Angular momentum evolution of young stars and disks. *Annual Review of Astronomy and Astrophysics* **33,** 199–238 (1995).

123. Armitage, P. J., Kley, W. & Armitage, P. J. Physical processes in protoplanetary disks. *From Protoplanetary Disks to Planet Formation: Saas-Fee Advanced Course 45. Swiss Society for Astrophysics and Astronomy,* 1–150 (2019).

Appendix A

GREEN'S FUNCTION METHOD

A.1 Double Helix Current Wire Magnetic Field Calculation

We consider two helically braided current wires each with uniform current density on a circular cross-section having radius b in the $z = 0$ plane; these cross-sections are the red circles in Figure 6.3(b). These wires will be referred to as wire #1 and wire #2. The respective centers of the two circular cross sections of wires #1 and #2 are, respectively, at $(r, \theta) = (a, 0)$ and $(r, \theta) = (a, \pi)$. Through each circular cross-section there is a uniform axial current density $J_z(r', \phi') = J_{z0}$ for $(x \pm a)^2 + y^2 \leq b^2$ and $J_z(r', \phi') = 0$ elsewhere. Using Equations (5.3-5.5), the magnetic field at $a - b \leq r \leq a + b$ can be derived; this magnetic field is needed to calculate the force on the wires as prescribed by Equation 5.6.

Consider the radial magnetic field $B_{r,\#1}$ at $a - b < r < a + b$ generated from wire #1 which has its circular cross-section in the $z = 0$ plane centered at $r = a$ and $\theta = 0$. The integration surface S' with finite J_{z0} is the interior of the circle cross-section defined by $(r' \cos(\varphi') - a)^2 + (r' \sin(\varphi'))^2 \leq b^2$. For a given r' with $a-b < r' < a+b$, the integration interval for φ' is from $[-c(r'), c(r')]$, where these limits define the edge of the circle cross-section. The limits $\pm c(r')$ are determined by defining three vectors: $\mathbf{a}$ which goes from $x = 0, y = 0$ to the center of the circle $x = a, y = 0$, $\mathbf{r}'$ which has magnitude r' and goes from $x = 0, y = 0$ to the upper edge of the circle, and $\mathbf{b}$ which has magnitude b and goes from the center of the circle $x = a, y = 0$ to the tip of $\mathbf{r}'$. Thus $\mathbf{r}' - \mathbf{a} = \mathbf{b}$ so $r'^2 - 2\mathbf{r}' \cdot \mathbf{a} + a^2 = b^2$. Using $\mathbf{r}' \cdot \mathbf{a} = r' a \cos(c(r'))$ gives $c(r') = \arccos\left(\frac{r'^2 + a^2 - b^2}{2ar'}\right)$.

To simplify the notation, we define $R = nkr$, $\xi = nkr'$,

$$Q_n(R) = I'_n(R) \int_R^{nk(a+b)} d\xi \xi^2 K'_n(\xi) \sin[nc(\xi/nk)] + K'_n(R) \int_{nk(a-b)}^{R} d\xi \xi^2 I'_n(\xi) \sin[nc(\xi/nk)] \tag{A.1}$$

and

$$W_n(R) = I_n(R) \int_R^{nk(a+b)} d\xi \xi^2 K'_n(\xi) \sin[nc(\xi/nk)] + K_n(R) \int_{nk(a-b)}^{R} d\xi \xi^2 I'_n(\xi) \sin[nc(\xi/nk)]. \tag{A.2}$$

Using Equation (5.3), we can then express the radial magnetic field from wire #1 in a more compact form as

$$\begin{aligned} B_{r,\#1}(r,\theta,z) &= \int_{r}^{a+b} r'dr' \int_{-c(r')}^{c(r')} d\varphi' \frac{\mu_0 J_{z0}}{\pi} k^2 r' \sum_{n=1}^{\infty} nK'_n(nkr')\, I'_n(nkr) \sin\left[n(\theta - kz - \varphi')\right] \\ &+ \int_{a-b}^{r} r'dr' \int_{-c(r')}^{c(r')} d\varphi' \frac{\mu_0 J_{z0}}{\pi} k^2 r' \sum_{n=1}^{\infty} nI'_n(nkr')\, K'_n(nkr) \sin\left[n(\theta - kz - \varphi')\right] \\ &= \frac{2\mu_0 J_{z0}}{\pi k} \sum_{n=1}^{\infty} \frac{1}{n^3} \sin\left[n(\theta - kz)\right] Q_n(R). \end{aligned} \tag{A.3}$$

Wire #2 is centered at $(r,\theta) = (a,\pi)$. By replacing $\sin[n(\theta - kz)]$ with $\sin[n(\theta - kz - \pi)] = (-1)^n \sin[n(\theta - kz)]$ in Equation (A.3), we can derive the radial magnetic field $B_{r,\#2}$ generated from wire #2 as

$$B_{r,\#2} = \frac{2\mu_0 J_{z0}}{\pi k} \sum_{n=1}^{\infty} \frac{(-1)^n}{n^3} \sin\left[n(\theta - kz)\right] Q_n(R)\,. \tag{A.4}$$

Adding the radial magnetic fields of wires #1 and #2, the radial magnetic field generated from the two wires is

$$B_r(r,\theta,z) = \frac{4\mu_0 J_z}{\pi k} \sum_{\substack{n=2i \\ i=1}}^{\infty} \frac{1}{n^3} \sin\left[n(\theta - kz)\right] Q_n(R). \tag{A.5}$$

Similarly, B_θ and B_z are calculated as below

$$B_\theta(r,\theta,z) = \frac{2\mu_0 J_z}{\pi r} \int_{a-b}^{r} dr' r' c(r') + \frac{4\mu_0 J_z}{\pi k^2 r} \sum_{\substack{n=2i \\ i=1}}^{\infty} \frac{1}{n^3} \cos\left[n(\theta - kz)\right] W_n(R) \tag{A.6}$$

$$B_z(r,\theta,z) = \frac{2\mu_0 J_z k}{\pi} \int_{r}^{a+b} dr' r' c(r') - \frac{4\mu_0 J_z}{\pi k} \sum_{\substack{n=2i \\ i=1}}^{\infty} \frac{1}{n^3} \cos\left[n(\theta - kz)\right] W_n(R)\,. \tag{A.7}$$

The magnetic field at $r < a - b$ can be obtained by referring back to Equation (5.2) and realizing that all the current is such that $r < r'$ and this current is located in the range $a - b < r' < a + b$. This implies that the integration uses the $r < r'$ prescription for the magnetic field and is over the range $a - b < r' < a + b$. This

can be accomplished by replacing the r limits in the two integrals on the right hand side of Equation (A.3) by $a-b$, i.e., $\int_{r}^{a+b} + \int_{a-b}^{r} \rightarrow \int_{a-b}^{a+b} + \int_{a-b}^{a-b} \rightarrow \int_{a-b}^{a+b}$. Similarly the magnetic field at $r > a+b$ is obtained by replacing the r limits in the two integrals on the right hand side of Equation (A.3) by $a+b$. These replacements should be used for evaluating $Q_n(R)$ and $W_n(R)$ when calculating the magnetic field in the region $r < a-b$ or in the region $r > a-b$.

A.2 Magnetic Force Calculation

For the magnetic force in Equation (5.7-5.9), the integration region S is $(x-a)^2 + y^2 \leq b^2$, so $\int dS = \int_{a-b}^{a+b} r dr \int_{-c(r)}^{c(r)} d\theta$. From Equation (A.5-A.7), B_r and $(krB_z - B_\theta)\sin\theta + B_r\cos\theta$ are an odd function of θ, so $f_y = 0$ and $f_z = 0$. Using Equation (5.7), f_x can be calculated as

$$f_x = \int_{a-b}^{a+b} r dr \int_{-c(r)}^{c(r)} d\theta J_{z0} \left[(krB_z - B_\theta)\cos\theta - B_r \sin\theta \right]. \tag{A.8}$$

We define the dimensionless force $\bar{f}_x = f_x \Big/ \left(\frac{\mu_0 J_{z0}^2 \pi^2 b^4}{4\pi a} \right)$ and then use Equations (A.5)-(A.7) in Equation (A.8) to obtain

$$\bar{f}_x = \frac{32a}{\pi^2 k^3 b^4} \left\{ \begin{array}{l} \frac{k^3}{2} \int_{a-b}^{a+b} dr \left(- \int_{a-b}^{r} dr' r' c\left(r'\right) + k^2 r^2 \int_{r}^{a+b} dr' r' c\left(r'\right) \right) \sin c\left(r\right) \\ - \sum_{\substack{n=2i \\ i=1}}^{\infty} \int_{nk(a-b)}^{nk(a+b)} dR \left\{ \begin{array}{l} \frac{n\cos c\left(\frac{R}{nk}\right)\sin nc\left(\frac{R}{nk}\right) - \sin c\left(\frac{R}{nk}\right)\cos nc\left(\frac{R}{nk}\right)}{n^4\left(n^2-1\right)} \left(1 + \left(\frac{R}{n}\right)^2\right) W_n\left(R\right) \\ + \frac{\cos c\left(\frac{R}{nk}\right)\sin nc\left(\frac{R}{nk}\right) - n\sin c\left(\frac{R}{nk}\right)\cos nc\left(\frac{R}{nk}\right)}{n^4\left(n^2-1\right)} \frac{R}{n} Q_n\left(R\right) \end{array} \right\} \end{array} \right\}. \tag{A.9}$$

The dimensionless force f_x is calculated numerically, and the summation on n stops when the relative error $|\Delta f_x / f_x| < 10^{-5}$.

A.3 Curl of Magnetic Force

Static equilibrium $\nabla P = \mathbf{J} \times \mathbf{B}$ requires the magnetic force to be curl-free, that is $\nabla \times (\mathbf{J} \times \mathbf{B}) = 0$.

Let us consider a general case for a helical current density $\mathbf{J}(r,\theta,z) = J_z(r,u)\left[kr\hat{\theta} + \hat{z}\right]$, where $u = \theta - kz$ is the helical parameter. The magnetic field can be calculated from Equations (5.3-5.5) as $\mathbf{B}(r,\theta,z) = \mathbf{B}(r,u) = B_r\hat{r} + B_\theta\hat{\theta} + B_z\hat{z}$. As the system is helically symmetric with physical quantities depending only on r and $u = \theta - kz$, it is seen that $\frac{\partial}{\partial\theta} = \frac{\partial}{\partial u}$ and $\frac{\partial}{\partial z} = -k\frac{\partial}{\partial u} = -k\frac{\partial}{\partial\theta}$. The curl can be calculated as

$$\nabla \times (\mathbf{J} \times \mathbf{B}) = \left(\frac{\partial}{\partial r} \left(J_z r B_r \right) - \frac{\partial}{\partial \theta} J_z \left(k r B_z - B_\theta \right) \right) \frac{1}{r} \left[k r \hat{\theta} + \hat{z} \right]. \tag{A.10}$$

From $\nabla \cdot \mathbf{B} = 0$, it is seen that $\frac{\partial}{\partial r} \left(r B_r \right) - \frac{\partial}{\partial \theta} \left(k r B_z - B_\theta \right) = 0$, so Equation (A.10) can be expressed as

$$\nabla \times (\mathbf{J} \times \mathbf{B}) = \left[r B_r \frac{\partial}{\partial r} J_z - \left(k r B_z - B_\theta \right) \frac{\partial}{\partial \theta} J_z \right] \frac{1}{r} \left[k r \hat{\theta} + \hat{z} \right] \tag{A.11}$$

and the curl-free condition becomes

$$r B_r \frac{\partial}{\partial r} J_z - \left(k r B_z - B_\theta \right) \frac{\partial}{\partial \theta} J_z = 0. \tag{A.12}$$

The uniform-current density distribution assumed here automatically satisfies Equation (A.12). In order to have a static equilibrium $\nabla P = \mathbf{J} \times \mathbf{B}$ for a non-uniform current density, the current distribution and associated magnetic field would have to satisfy Equation (A.12). If $\nabla \times (\mathbf{J} \times \mathbf{B}) \neq 0$, a torque will be exerted on the plasma which would drive vortex flows. These flows could develop a steady-state if this torque is balanced by a viscous drag.

Appendix B

CANONICAL ANGULAR MOMENTUM CONSERVATION

In an electromagnetic system exhibiting azimuthal symmetry, the electric field **E** and the magnetic field **B** does not depend on the azimuthal angle θ. The same is true for the magnetic potential **A** and the electric potential ϕ. The poloidal magnetic flux $\psi\,(r,z) = \int \mathbf{B}\cdot d\mathbf{S}$ is defined as the magnetic flux across a circular crosssection centered at $(r,\theta,z) = (0,0,z)$. As $\int \mathbf{B}\cdot d\mathbf{S} = \int (\nabla\times\mathbf{A})\cdot d\mathbf{S} = \oint \mathbf{A}\cdot d\mathbf{l} = 2\pi r A_\theta$,

$$\psi\,(r,z) = 2\pi r A_\theta. \tag{B.1}$$

B.1 One Particle System

Considering a charged particle with mass m and charge q in this system with a massive central body M_* at the center, the lagrangian is

$$L = \frac{1}{2}m\left(\dot{r}^2 + r^2\dot{\theta}^2 + \dot{z}^2\right) + \frac{GM_*m}{\sqrt{r^2+z^2}} + q\left(\dot{r}A_r + r\dot{\theta}A_\theta + \dot{z}A_z\right) - q\phi. \tag{B.2}$$

The canonical angular momentum is defined as $P_\theta = \frac{\partial L}{\partial\dot{\theta}}$. Defining the azimuthal velocity $v_\theta = r\dot{\theta}$ and using Equation B.1,

$$P_\theta = mrv_\theta + \frac{q}{2\pi}\psi. \tag{B.3}$$

From Lagrange's equation,

$$\frac{d}{dt}P_\theta = \frac{d}{dt}\frac{\partial L}{\partial\dot{\theta}} = \frac{\partial L}{\partial\theta} = 0. \tag{B.4}$$

Then,

$$P_\theta = mrv_\theta + \frac{q}{2\pi}\psi = \text{Const.} \tag{B.5}$$

B.2 Two Particles System

Considering a system with two particles, particle i and particle j, the lagrangian is

$$\begin{aligned} L = & \frac{1}{2}m\left(\dot{r}_i^2 + r_i^2\dot{\theta}_i^2 + \dot{z}_i^2\right) + \frac{GM_*m_i}{\sqrt{r_i^2+z_i^2}} + q_i\left(\dot{r}_iA_{ri} + r_i\dot{\theta}_iA_{\theta i} + \dot{z}_iA_{zi}\right) - q_i\phi_i \\ & + \frac{1}{2}m\left(\dot{r}_j^2 + r_j^2\dot{\theta}_j^2 + \dot{z}_j^2\right) + \frac{GM_*m_j}{\sqrt{r_j^2+z_j^2}} + q_j\left(\dot{r}_jA_{rj} + r_j\dot{\theta}_jA_{\theta j} + \dot{z}_jA_{zj}\right) - q_j\phi_j \\ & + f_{ij}\left(\left|\mathbf{r}_i - \mathbf{r}_j\right|^2\right) \end{aligned} \tag{B.6}$$

where $f_{ij}\left(\left|\mathbf{r}_i - \mathbf{r}_j\right|^2\right)$ is the interaction potential between particle i and j.

As

$$\frac{\partial f_{ij}}{\partial\theta_i} = \frac{\partial f_{ij}}{\partial\left|\mathbf{r}_i - \mathbf{r}_j\right|^2}\frac{\partial\left|\mathbf{r}_i - \mathbf{r}_j\right|^2}{\partial\left(\theta_i - \theta_j\right)}\frac{\partial\left(\theta_i - \theta_j\right)}{\partial\theta_i} \tag{B.7}$$

and

$$\frac{\partial f_{ij}}{\partial\theta_j} = \frac{\partial f_{ij}}{\partial\left|\mathbf{r}_i - \mathbf{r}_j\right|^2}\frac{\partial\left|\mathbf{r}_i - \mathbf{r}_j\right|^2}{\partial\left(\theta_i - \theta_j\right)}\frac{\partial\left(\theta_i - \theta_j\right)}{\partial\theta_j} = -\frac{\partial f_{ij}}{\partial\theta_i} \tag{B.8}$$

$$\frac{\partial L}{\partial\theta_i} + \frac{\partial L}{\partial\theta_j} = \frac{\partial f_{ij}}{\partial\theta_i} + \frac{\partial f_{ij}}{\partial\theta_j} = 0. \tag{B.9}$$

Using Lagrange's equation,

$$\frac{d}{dt}\left(\frac{\partial L}{\partial\dot{\theta}_i} + \frac{\partial L}{\partial\dot{\theta}_j}\right) = \frac{\partial L}{\partial\theta_i} + \frac{\partial L}{\partial\theta_j} = 0, \tag{B.10}$$

so the total canonical angular momentum

$$\begin{aligned} P_{\theta i} + P_{\theta j} &= \frac{\partial L}{\partial\dot{\theta}_i} + \frac{\partial L}{\partial\dot{\theta}_j} \\ &= m_ir_iv_{\theta i} + \frac{q}{2\pi}\psi_i + m_jr_jv_{\theta j} + \frac{q}{2\pi}\psi_j \\ &= \text{Const} \end{aligned} \tag{B.11}$$

B.3 N Particles System

For a system with N particles, the lagrangian is

$$L = \sum_i^N\left[\ \tfrac{1}{2}m\left(\dot{r}_i^2 + r_i^2\dot{\theta}_i^2 + \dot{z}_i^2\right) + \tfrac{GM_*m_i}{\sqrt{r_i^2+z_i^2}} + q_i\left(\dot{r}_iA_{ri} + r_i\dot{\theta}_iA_{\theta i} + \dot{z}_iA_{zi}\right) - q_i\phi_i + \sum_{j>i}^N f_{ij}\left(\left|\mathbf{r}_i - \mathbf{r}_j\right|^2\right)\ \right] \tag{B.12}$$

where $f_{ij}\left(\left|\mathbf{r}_i - \mathbf{r}_j\right|^2\right)$ is the interaction potential between particle i and j. From Newton's third law, every force in nature there is an equal and opposite reaction, so $\frac{\partial f_{ij}}{\partial \theta_i} + \frac{\partial f_{ij}}{\partial \theta_j} = 0$. Using Lagrange's equation,

$$\frac{d}{dt}\sum_i^N \frac{\partial L}{\partial \dot{\theta}_i} = \sum_i^N \frac{\partial L}{\partial \theta_i} = \sum_i^N \sum_{j>i}^N \frac{\partial f_{ij}\left(\left|\mathbf{r}_i - \mathbf{r}_j\right|^2\right)}{\partial \theta_i} = 0, \tag{B.13}$$

so the total canonical angular momentum

$$P_\theta = \sum_i^N \frac{\partial L}{\partial \dot{\theta}_i} = \sum_i^N m_i r_i v_{i\theta} + \frac{q_i}{2\pi}\psi_i = \text{Const.} \tag{B.14}$$

Appendix C

CONNECTING THE PARTICLE-LEVEL PHYSICS TO FLUID-LEVEL PHYSICS

In Chapter 6, we study accretion disk dynamics by analyzing the motion of single particles and deriving the neutral radial velocity and mass accretion rates based on the conservation of canonical angular momentum. Most researchers study the accretion disk from single MHD equations and Non-ideal MHD effects [123]. This appendix bridges the gap between particle-level motion and fluid-level motion. We derive the radial velocity and mass accretion rate from fluid equations, providing a comprehensive understanding of the underlying dynamics from different aspects.

C.1 The Radial Velocity of Charged Particles and Neutrals Derived from Fluid Equations.

The equation of motion for neutrals is

$$\rho_n \frac{d\mathbf{u}_n}{dt} = -\nabla P_n - \rho_n \nabla\Phi - \mathbf{p}_{ni} - \mathbf{p}_{ne} \tag{C.1}$$

where Φ is the gravitational potential, and $\mathbf{p}_{ni}$ and $\mathbf{p}_{ne}$ are the rate of momentum exchange due to collisions between the neutrals and the ions/electrons, respectively. In the astrophysics community, the notation $\mathbf{p}_{n\sigma}$ is commonly used to represent momentum exchange, while in the plasma physics community, the notation $\mathbf{R}_{n\sigma}$ is typically employed for the same purpose.

Similar equations apply to the charged species, but have the addition of Lorentz forces,

$$\rho_i \frac{d\mathbf{u}_i}{dt} = -\nabla P_i - \rho_i \nabla\Phi + Zen_i \left(\mathbf{E} + \mathbf{u}_i \times \mathbf{B}\right) - \mathbf{p}_{in} \tag{C.2}$$

$$\rho_e \frac{d\mathbf{u}_e}{dt} = -\nabla P_e - \rho_e \nabla\Phi - en_e \left(\mathbf{E} + \mathbf{u}_e \times \mathbf{B}\right) - \mathbf{p}_{en}. \tag{C.3}$$

where $\mathbf{E}$ and $\mathbf{B}$ are the electric and magnetic fields. Z is the ion charge number.

The rate of the momentum exchange/drag forces are given by

$$\mathbf{p}_{in} = -\mathbf{p}_{ni} = n_i m_i \nu_{in} \left(\mathbf{u}_i - \mathbf{u}_n\right) = n_i \frac{m_i m_n}{m_i + m_n} n_n \langle \sigma v \rangle_{in} \left(\mathbf{u}_i - \mathbf{u}_n\right) \tag{C.4}$$

and

$$\mathbf{p}_{en} = -\mathbf{p}_{ne} = n_e m_e \nu_{en} \left(\mathbf{u}_e - \mathbf{u}_n\right) = n_e \frac{m_e m_n}{m_e + m_n} n_n \langle \sigma v \rangle_{en} \left(\mathbf{u}_e - \mathbf{u}_n\right) \tag{C.5}$$

where typical values [105] are

$$\langle \sigma v \rangle_{in} = 1.9 \times 10^{-9} \mathrm{cm}^3 \cdot \mathrm{s}^{-1} \tag{C.6}$$

and

$$\langle \sigma v \rangle_{en} = 10^{-15} \mathrm{cm}^2 \left(\frac{128 k_B T}{9\pi m_e}\right)^{\frac{1}{2}} = 8.3 \times 10^{-10} \left(\frac{T}{K}\right)^{\frac{1}{2}} \mathrm{cm}^3 \cdot \mathrm{s}^{-1}. \tag{C.7}$$

The timescale for the macroscopic evolution of the fluid is generally much longer than the timescale for collisional or magnetic forces to alter a charged particle's momentum. Therefore, we can ignore all terms in the momentum equations for the charged species except for the Lorentz and collisional terms. This means that for ions and elections, we have

$$Z e n_i \left(\mathbf{E} + \mathbf{u}_i \times \mathbf{B}\right) - \mathbf{p}_{in} = 0 \tag{C.8}$$

$$-e n_e \left(\mathbf{E} + \mathbf{u}_e \times \mathbf{B}\right) - \mathbf{p}_{en} = 0. \tag{C.9}$$

The charged particle fluid velocities can be solved for from Equations C.8 and C.9 as

$$\mathbf{u}_\sigma = \frac{1}{1 + \xi_\sigma^2} \left[\xi_\sigma \left(\frac{\mathbf{E}}{B} + \mathbf{u}_n \times \frac{\mathbf{B}}{B} \right) + \frac{\mathbf{E} \times \mathbf{B}}{B^2} + \xi_\sigma^2 \mathbf{u}_n + \frac{\left(\mathbf{u}_\sigma \cdot \mathbf{B}\right) \mathbf{B}}{B^2} \right] \tag{C.10}$$

For the motion in the midplane with $\mathbf{u}_\sigma \cdot \mathbf{B} = 0$, this solution reduces to

$$\mathbf{u}_\sigma = \frac{\xi_\sigma \left(\frac{\mathbf{E}}{B} + \mathbf{u}_n \times \frac{\mathbf{B}}{B} \right) + \frac{\mathbf{E} \times \mathbf{B}}{B^2} + \xi_\sigma^2 \mathbf{u}_n}{1 + \xi_\sigma^2}. \tag{C.11}$$

If the electric field is zero, this velocity reduces to

$$\mathbf{u}_\sigma = \frac{\xi_\sigma \mathbf{u}_n \times \frac{\mathbf{B}}{B} + \xi_\sigma^2 \mathbf{u}_n}{1 + \xi_\sigma^2} \tag{C.12}$$

This is the same as Equation 6.11 in this thesis.

Using charge neutrality $n_e = Z n_i$ and current density $\mathbf{J} = e n_e \left(\mathbf{u}_i - \mathbf{u}_e\right)$, and summing C.8 and C.9, we have

$$\mathbf{J} \times \mathbf{B} = \mathbf{p}_{in} + \mathbf{p}_{en}. \tag{C.13}$$

The equation of motion for neutrals becomes

$$\rho_n \frac{d\mathbf{u}_n}{dt} = -\nabla P_n - \rho_n \nabla\Phi + \mathbf{J} \times \mathbf{B}. \tag{C.14}$$

The azimuthal component of Equation C.14 is

$$\rho_n \left(\frac{\partial u_{n\theta}}{\partial t} + u_{nr}\frac{\partial u_{n\theta}}{\partial r} + u_{nz}\frac{\partial u_{n\theta}}{\partial z} + \frac{u_{n\theta}u_{nr}}{r} \right) = -J_r B_z. \tag{C.15}$$

As particles in accretion disk evolve as Kepler velocity with $u_{n\theta} = \sqrt{\frac{GM_*}{r}}$, then, $\frac{\partial u_{n\theta}}{\partial t} = 0$, $\frac{\partial u_{n\theta}}{\partial z} = 0$, $\frac{\partial u_{n\theta}}{\partial r} = -\frac{u_{n\theta}}{2r}$. This becomes

$$\rho_n \frac{u_{nr}\omega_K}{2} = -J_r B_z \tag{C.16}$$

so using $J_r = n_e e\,(u_{ir} - u_{er})$ and $\rho_n = n_n m_n$ this becomes

$$u_{nr} = \frac{-2n_e e\,(u_{ir} - u_{er})\,B_z}{\rho_n \omega_K} = -2\frac{n_e}{n_n}\frac{m_i}{m_n}\frac{(u_{ir} - u_{er})}{\omega_K}\frac{eB_z}{m_i} \tag{C.17}$$

Defining the ion cyclotron frequency $\omega_{ci} = eB_z/m_i$ and the ionization fraction $\chi = n_e/n_n$ this becomes

$$u_{nr} = -2\chi\frac{\omega_{ci}}{\omega_K}\frac{m_i}{m_n}\,(u_{ir} - u_{er}) \tag{C.18}$$

This is similar to Equation 6.18 with a factor 2 difference. Factor 2 is from keeping particles as Kepler velocity. Detailed discussion for factor 2 can be found in the paragraph before Equation 6.20. Similarly, the mass accretion rate can be derived from the neutrals' radial velocity with a factor 2 difference.

Equation C.18 has not been previously discussed in the other literature. Most researchers follow a traditional approach, deriving the neutral velocity and accretion rate from a neutral fluid momentum equation that does not include the drag force from charged particles. For example, see Equation (53) in Reference [123].

From Equation C.11, the electric field would reduce the radial velocity of ions and elections, so would oppose the accretion. In the real system, there can be a certain level of electric field, but it can not equal to $-\mathbf{u}_n \times \mathbf{B}$, as this would result in a zero radial velocity for the neutrals. Removing the build-up of the charged particles requires a 3D picture with a closed electric circuit, including the astrophysical jets.

C.2 Non-ideal MHD Effects

Other researchers often reframe Equation B.9 to include non-ideal MHD effects and may be curious about which non-ideal effects prevail in the parameter we utilized to compute the mass accretion rate. Now, I will proceed to derive the equation for non-ideal MHD effects.

Dividing by en_e, the electrons' momentum equation C.9 can be expanded to

$$\mathbf{E} + [\mathbf{u}_n + (\mathbf{u}_e - \mathbf{u}_i) + (\mathbf{u}_i - \mathbf{u}_n)] \times \mathbf{B} + \frac{m_e \nu_{en}}{e} [(\mathbf{u}_e - \mathbf{u}_i) + (\mathbf{u}_i - \mathbf{u}_n)] = 0. \quad \text{(C.19)}$$

As the temperature of a protoplanetary disk is much smaller than 10^6 K,

$$\left| \frac{\mathbf{p}_{in}}{\mathbf{p}_{en}} \right| = \frac{m_i}{m_e} \frac{m_e + m_n}{m_i + m_n} \frac{n_i}{n_e} \frac{\langle \sigma v \rangle_{in}}{\langle \sigma v \rangle_{en}} \left| \frac{(\mathbf{u}_i - \mathbf{u}_n)}{(\mathbf{u}_e - \mathbf{u}_n)} \right| \approx \frac{1}{Z} \frac{m_i}{m_e} \frac{1}{\left(\frac{T}{K}\right)^{\frac{1}{2}}} \gg 1. \quad \text{(C.20)}$$

Then from Equation C.13

$$\mathbf{J} \times \mathbf{B} \approx \mathbf{p}_{in} = \rho_i \nu_{in} (\mathbf{u}_i - \mathbf{u}_n) . \quad \text{(C.21)}$$

Then,

$$\frac{m_e \nu_{en}}{e} (\mathbf{u}_i - \mathbf{u}_n) \approx \frac{m_e \nu_{en}}{e} \frac{\mathbf{J} \times \mathbf{B}}{\rho_i \nu_{in}} = Z \frac{m_e \nu_{en}}{m_i \nu_{in}} \frac{\mathbf{J} \times \mathbf{B}}{n_e e} \approx \frac{m_e}{m_i} \sqrt{\frac{T}{K}} (\mathbf{u}_e - \mathbf{u}_i) \times \mathbf{B} \ll (\mathbf{u}_e - \mathbf{u}_i) \times \mathbf{B}. \quad \text{(C.22)}$$

The last term in Equation C.19 can thus be ignored. Equation C.19 becomes

$$\mathbf{E} + [\mathbf{u}_n + (\mathbf{u}_e - \mathbf{u}_i) + (\mathbf{u}_i - \mathbf{u}_n)] \times \mathbf{B} + \frac{m_e \nu_{en}}{e} (\mathbf{u}_e - \mathbf{u}_i) = 0. \quad \text{(C.23)}$$

Using $\mathbf{u}_e - \mathbf{u}_i = -\frac{\mathbf{J}}{n_e e}$ and $\mathbf{u}_i - \mathbf{u}_n = \frac{\mathbf{J} \times \mathbf{B}}{\rho_i \nu_{in}}$, Equation C.19 becomes

$$\mathbf{E} + \mathbf{u}_n \times \mathbf{B} - \frac{\mathbf{J} \times \mathbf{B}}{n_e e} + \frac{(\mathbf{J} \times \mathbf{B}) \times \mathbf{B}}{\rho_i \nu_{in}} - \frac{m_e \nu_{en}}{n_e e^2} \mathbf{J} = 0. \quad \text{(C.24)}$$

Taking the curl of the equation, we obtain

$$\frac{\partial \mathbf{B}}{\partial t} = \nabla \times \left[\mathbf{u}_n \times \mathbf{B} - \frac{\mathbf{J} \times \mathbf{B}}{n_e e} + \frac{(\mathbf{J} \times \mathbf{B}) \times \mathbf{B}}{\rho_i \nu_{in}} - \frac{m_e \nu_{en}}{n_e e^2} \mathbf{J} \right]. \quad \text{(C.25)}$$

On the right side of the equation, the first term is defined as the induction term

$$I = \mathbf{u}_n \times \mathbf{B}, \quad \text{(C.26)}$$

and the second term is defined as the Hall term

$$H = \frac{\mathbf{J} \times \mathbf{B}}{n_e e}, \tag{C.27}$$

and the third term is defined as the ambipolar term

$$A = \frac{(\mathbf{J} \times \mathbf{B}) \times \mathbf{B}}{\rho_i \nu_{in}}, \tag{C.28}$$

and the last one is defined as the ohmic term

$$O = \frac{m_e \nu_{en}}{n_e e^2} \mathbf{J}. \tag{C.29}$$

Then, the scaling of each of these terms relative to the Hall term H is

$$\frac{I}{H} \sim \frac{u_n}{u_i - u_e} \tag{C.30}$$

$$\frac{A}{H} \sim \frac{\omega_{ci}}{\nu_{in}} = \frac{1}{|\xi_i|} \tag{C.31}$$

$$\frac{O}{H} \sim \frac{\nu_{en}}{\omega_{ce}} = |\xi_e| \tag{C.32}$$

The parameters we used in Chapter 6 are $r = 1$ a.u., $n_n = 10^{20}$ m^{-3}, $B = 5$ mG, $\chi = 10^{-12}$, $T_e = 100$ K, $h = 0.1$ a.u., $m_i = m_H = 1.66 \times 10^{-27}$ kg, $m_n = m_{H_2} = 3.32 \times 10^{-27}$ kg. Then $\omega_{ci} = 48$ s^{-1}, $\omega_{ce} = 8.8 \times 10^4$ s^{-1}, $\nu_{in} = 1.3 \times 10^5$ s^{-1}, $\nu_{en} = 8.3 \times 10^5$ s^{-1}, $|\xi_i| = 2627$ and $|\xi_e| = 9.44$. The mass accretion rate is $\dot{M} = 2.9 \times 10^{-8}\ M_\odot \cdot \text{year}^{-1}$. The ohmic effect dominates under this case with $O > H > A$.

It is just one possible set of parameters we choose. The mass accretion rate is also reasonable under parameters with other nonideal MHD effects dominating. For example, if we adjust $n_n = 10^{19}$ m^{-3} and $B = 50$ mG while keeping other parameters unchanged, then $|\xi_i| = 26.27$ and $|\xi_e| = 0.0944$. The mass accretion rate becomes $\dot{M} = 3.5 \times 10^{-8}\ M_\odot \cdot \text{year}^{-1}$. The Hall effect dominates under this case with $H > O > A$.

Equation C.25 can also be written as a diffusivities equation, with

$$\frac{\partial \mathbf{B}}{\partial t} = \nabla \times \left[\mathbf{u}_n \times \mathbf{B} - \eta_H \frac{(\nabla \times \mathbf{B}) \times \mathbf{B}}{B} + \eta_A \frac{((\nabla \times \mathbf{B}) \times \mathbf{B}) \times \mathbf{B}}{B^2} - \eta_O (\nabla \times \mathbf{B}) \right] \tag{C.33}$$

where

$$\eta_H = \frac{B}{\mu_0 n_e e} \tag{C.34}$$

$$\eta_A = \frac{B^2}{\mu_0 \rho_i \nu_{in}} \tag{C.35}$$

$$\eta_O = \frac{m_e \nu_{en}}{\mu_0 n_e e^2}. \tag{C.36}$$

It is a common practice to define dimensionless numbers in association with non-ideal effects in order to quantify their relative importance in the induction equation. Elsasser numbers can be defined as

$$\Lambda_{H,A,O} = \frac{V_A^2}{\omega_K \eta_{H,A,O}} = \frac{B^2}{\mu_0 n_n m_n \omega_K \eta} \tag{C.37}$$

Then,

$$\Lambda_O = \chi_i \frac{\omega_{ci}}{\xi_e \omega_K} \frac{m_i}{m_n} \tag{C.38}$$

$$\Lambda_H = \chi_i \frac{\omega_{ci}}{\omega_K} \frac{m_i}{m_n} \tag{C.39}$$

$$\Lambda_A = \chi_i \frac{\nu_{in}}{\omega_K} \frac{m_i}{m_n}. \tag{C.40}$$

Using the parameters outlined after Equation C.32, $\Lambda_O = 1.3 \times 10^{-5}$, $\Lambda_H = 1.2 \times 10^{-4}$, $\Lambda_A = 0.31$.

C.3 Summary

To sum up, the radial velocities of ions, electrons, and neutrals, derived from a single particle's motion and canonical angular momentum conservation in Chapter 6, can also be obtained from fluid equations. Unlike the conventional approach of converting the electron fluid momentum equation to an equation of non-ideal MHD effects, we directly derive the velocities of ions, electrons, and neutrals. The angular momentum transport and accretion can be understood from two different languages. At the particle level, neutrals accrete due to the transport of angular momentum into canonical angular momentum of charged particles. At the fluid level, magnetic torque from $\mathbf{J} \times \mathbf{B}$ removes the angular momentum of neutrals, leading to their accretion.